ULTRAFAST LASER INDUCED THERMO-ELASTO-PLASTODYNAMICS IN POLYCRYSTALLINE METALS

A Dissertation

by

XU MAO

Submitted to the Office of Graduate and Professional Studies of
Texas A&M University
in partial fulfillment of the requirements for the degree of

DOCTOR OF PHILOSOPHY

Chair of Committee, Chii-Der S. Suh
Committee Members, Jyhwen Wang
Alex (Gwo-Ping) Fang
Sy-Bor Wen
Head of Department, Andreas A. Polycarpou

December 2018

Major Subject: Mechanical Engineering

ABSTRACT

A comprehensive thermo-elasto-plastodynamic model of the laser-material interaction in polycrystalline metals in response to ultrafast laser heating is formulated. Lacking a fundamental understanding for the non-ablation and non-melting ablation processes and the underlying mechanism that governs coupled thermal-mechanical generation impedes the broader application of ultrashort lasers. The transport dynamics established in the dissertation describes the initial plasma plumes as the result of the photoelectric and thermionic emissions of electrons. The formulation admits finite electron and lattice energy transport speeds and incorporates energy losses to electrons emission and thermoelastic and thermoplastic generations. Elastic-plastic constitutive laws are incorporated to describe the complex elasto-plastodynamic cyclic behaviors attributed to the rapid thermal processing and metallic characteristics of the Bauschinger' effect. A staggered-grid finite difference scheme is time-integrated to resolve the coupled field responses using a one-dimensional formulation and an axisymmetric model.

The balance equations considered in the research obey the principle of energy conservation and follow the characteristic time scales associated with optical energy absorption, particle emission, and electron and lattice relaxations. Electron energy transport in polycrystalline metals is comprehensively investigated by considering temperature-dependent thermophysical properties and the grain size effects due to surface and grain boundary scatterings. Numerical results obtained for the non-ablation of a gold film under ultrafast optical heating is favorably examined against published experimental data for model validation. Parametric studies considering target thickness, grain size, and optical parameters indicate the impact of these parameters on energy transport, electrons emission, and coupled thermal-mechanical response. Crack initiation is investigated by

considering the propagation of stress waves generated by non-ablation heating. The novel concept of power density is adopted as the energy rate-based criterion to evaluate ablation mass removal and ablation depth as functions of laser fluence. The thermo-elasto-plastodynamic formulation is feasible for describing non-ablation thermoelastic generation and for exploring the correlation between the incident laser pulse and ablation and damage in polycrystalline metals.

ACKNOWLEDGEMENTS

I would like to express my sincere gratitude to my advisor Dr. Chii-Der S. Suh, who offered me such a great chance to join his lab and trusted and believed in me throughout my entire doctoral research at Texas A&M University. I am inspired by his spirit and attitude of seriousness toward physics, science and truth, which would encourage me thoughout my following research. And he always taught me to be confident and keep a positive attitude throughout my life. I would like to thank to my advisor again and I would not complete my doctoral research and dissertation without his help and significant contribution. I also would like to thank my dissertation committee members, Drs. Jyhwen Wang, Alex (Gwo-Ping) Fang and Sy-Bor Wen, for the great support and invaluable advice.

Thanks are also due to the Department of Mechanical Engineering, Texas A&M University and China Scholarship Council (CSC) for the essential financial support.

Last but not the least, I would like to express my deepest to my beloved wife, Xue and my baby, Crystal. You are the most precious gifts of my life. I am grateful to my parents for their love, patience, support and encouragement for all the years and I am pround to be your son. Again, lots of thanks to my family.

CONTRIBUTORS AND FUNDING SOURCES

Contributors

This worok was supported by a dissertation committee consisting of Professors Chii-Der S. Suh [advisor] and Sy-Bor Wen of the Department of Mechanical Engineering and Professors Jyhwen Wang and Alex (Gwo-Ping) Fang of the Department of Engineering Technology & Industrial Distribution.

All work for the dissertation was completed independently by the student.

Funding Sources

There are no outside funding contributions to acknowledge related to the research and compilation of this document.

TABLE OF CONTENTS

Page

ABSTRACT ii

ACKNOWLEDGEMENTS iv

CONTRIBUTORS AND FUNDING SOURCES v

TABLE OF CONTENTS vi

LIST OF FIGURES ix

LIST OF TABLES xi

1. LITERATURE REVIEW AND INTRODUCTION 1

1.1. Overview 1
1.2. Research Objective 13
1.3. Dissertation Outline 15
1.4. References 16

2. THERMO-ELASTO-DYNAMICS OF POLYCRYSTALLINE GOLD FILMS – GRAIN SIZE EFFECTS 23

2.1. Introduction 23
2.2. Thermophysical Properties of Polycrystalline Metals 27
2.2.1. Electron Heat Capacity 27
2.2.2. Grain Size Effect on Film and Grain Boundary Scattering 28
2.2.3. Electron Thermal Conductivity 29
2.2.4. Impact of Size Effects on Electron Thermal Conductivity 34
2.2.5. Electron-Phonon Coupling Factor 35
2.2.6. Impact of Size Effects on Electron-Phonon Coupling Factor 37
2.3. Energy Balance Equations and Constitutive Equations 38
2.3.1. Laser Intensity Source Term 39
2.3.2. Electron Energy Balance Equation 40
2.3.3. Lattice Energy Balance Equation 41
2.3.4. Constitutive Equations for One-Dimensional Thermo-elasticity 42
2.3.5. Initial and Boundary Conditions 43
2.4. Modelling Results 45
2.4.1. Model Verification: Normalized Change of Electron Temperature 46
2.4.2. Size Effects on Thermal-Mechanical Fields 49

2.5. Summary ····· 59
2.6. References ····· 60

3. THERMO-ELASTO-DYNAMICS OF POLYCRYSTALLINE GOLD FILMS – THERMAL-MECHANICAL MODELLING ····· 67

3.1. Introduction ····· 67
3.2. Energy Balance Equations and Constitutive Equations ····· 70
3.2.1. Axisymmetric Model ····· 70
3.2.2. Laser Intensity Source Term ····· 71
3.2.3. Electron Energy Balance Equation ····· 72
3.2.4. Lattice Energy Balance Equation ····· 73
3.2.5. Constitutive Equations for Three-Dimensional Thermo-Elasticity · 77
3.3. Computational Scheme ····· 78
3.3.1. Initial and Boundary Conditions ····· 78
3.3.2. Finite Difference Scheme of Three-Dimensional Model ····· 80
3.3.3. Numerical Discretization ····· 81
3.4. Model Validation ····· 85
3.5. Summary ····· 89
3.6. References ····· 90

4. THERMO-ELASTO-DYNAMICS OF POLYCRYSTALLINE GOLD FILMS – THERMAL-MECHANICAL DAMAGE MODE ····· 93

4.1. Introduction ····· 93
4.2. Three-Dimensional Thermal-Mechanical Fields ····· 96
4.2.1. Electron Temperature ····· 96
4.2.2. Lattice Temperature ····· 98
4.2.3. Grain Size Effects on Thermal Field ····· 100
4.2.4. Grain Size Effects on Stress Fields ····· 105
4.3. Characteristics and Power Density of Thermo-Elastic Stress Waves ····· 106
4.3.1. Thermal Stress Waves ····· 106
4.3.2. Power Density ····· 112
4.4. Summary ····· 115
4.5. References ····· 116

5. THERMO-ELASTO-PLASTO-DYNAMICS OF ULTRAFAST LASER ABLATION IN POLYCRYSTALLINE METALS ····· 119

5.1. Introduction ····· 119
5.2. Hot Carrier Emission ····· 124
5.2.1. Electron Emission ····· 125
5.2.2. Ion Emission Mechanism ····· 126
5.3. Thermo-Elasto-Plasto-Dynamics ····· 127
5.4. Electronic Transport Dynamics ····· 128
5.4.1. Surface Emission Rate ····· 130

5.4.2. Fowler Function ····· 132
5.4.3. Electrical Current inside Target ····· 134
5.5. Energy Balance Equations ····· 136
5.5.1. Electron Energy Balance Equations ····· 136
5.5.2. Lattice Energy Balance Equations ····· 137
5.5.3. Laser Intensity Source ····· 139
5.6. Thermo-Elasto-Plasto-Dynamic Equations of Motion ····· 139
5.6.1. Elasto-Plastic Model ····· 139
5.6.2. Time-Integration of the Elasto-Plastic Model ····· 143
5.7. Discretization on Finite Difference Scheme ····· 149
5.7.1. Initial and Boundary Conditions ····· 149
5.7.2. Summary of Field Equations ····· 150
5.7.3. Discretization Model ····· 151
5.8. Summary ····· 155
5.9. References ····· 155

6. THERMO-ELASTO-PLASTODYNAMIC RESPONSE AND DAMAGE EVALUATION ····· 166

6.1. Introduction ····· 166
6.2. Dynamics of Electron Subsystem ····· 167
6.2.1. Surface Emission Rate ····· 167
6.2.2. Electric Field ····· 170
6.2.3. Emitted Electron Number Density ····· 173
6.2.4. Maximum Thermal Field with and without Electron Emissions · 174
6.2.5. Effect of Laser Fluence and Pulse Duration ····· 177
6.3. Dynamics of Lattice Subsystem ····· 182
6.3.1. Stress-Strain Curve ····· 182
6.3.2. Thermal Field ····· 183
6.3.3. Thermal Stress Field ····· 188
6.3.4. Accumulated Plastic Strain ····· 192
6.4. Damage Evaluation and Ablation Depth Prediction ····· 193
6.4.1. Power Density and Ablation Depth Prediction ····· 193
6.5. Summary ····· 199
6.6. References ····· 201

7. CONCLUSIONS ····· 203

LIST OF FIGURES

Page

Figure 1 $C_e(T_e)/C_e(T_l)$ as a function of electron temperature 31

Figure 2 $\kappa_f/\kappa_{eq,b}$ vs. β for polycrystalline films 34

Figure 3 G_f/G_b as a function of film thickness parameter β for polycrystalline film..... 37

Figure 4 Temperature time profiles 46

Figure 5 Size effect on electron temperature (T_e) evolution..... 49

Figure 6 Size effect on lattice temperature (T_l) evolution 53

Figure 7 σ_{zz} in single crystalline film..... 54

Figure 8 σ_{zz} in single- and poly-crystalline films 56

Figure 9 Staggered-grid finite different scheme 80

Figure 10 Temperture time profiles 86

Figure 11 Size effects on maximum lattice temperature 88

Figure 12 Evolution of electron temperature in polycyrstalline film with D=20nm 96

Figure 13 Evolution of lattice temperature in polycyrstalline film with D=20nm 98

Figure 14 Temporal profiles of T_e for D=20nm and D=100nm at 4 different locations 100

Figure 15 Temporal profiles of T_l for D=20nm and D=100nm at 4 different locations..... 103

Figure 16 Temporal profiles of σ_{zz} corresponding to D=20nm and D=100nm at 4 different locations 105

Figure 17 GWT of σ_{zz} waves acquired at 3 consecutive locations 108

Figure 18 Spatial evolutions of stress components at 2 time instances for averaged grain size D= 20nm..... 111

Figure 19 Spatial evolutions of power density (dS/dt) components at 2 time instances with averaged grain size D= 20nm 113

Figure 20 Temporal evolutions of power density dS/dt at six different locations..... 114

Figure 21 GWT of power density at location (z=50nm, r=0) 115
Figure 22 Fowler function $F(x_N)$ 133
Figure 23 Flow chart of integration algorithm for elastic-plastic behavior 145
Figure 24 Total and thermionic emission rates at 4 different laser fluences 168
Figure 25 Evolution of emission rate at F=1.2 J/cm^2 170
Figure 26 Electrical field generated beneath the surface 171
Figure 27 Evolution of emitted electron number density at 4 different laser fluences 173
Figure 28 Time profiles of electron temperature at 4 different fluences 175
Figure 29 Comparison of electron profiles at 2 different laser fluences 176
Figure 30 Effect of pulse duration on the electronic and thermal fields at F=0.5 J/cm^2 178
Figure 31 Effect of laser fluence on the electronic and thermal fields at F=0.5 J/cm^2 180
Figure 32 Hysteresis loop under cyclic loadings using nonlinear kinematic hardening model 182
Figure 33 Temperature profiles at laser fluence F=0.8 J/cm^2 184
Figure 34 Evolution of electron and lattice temperatures at different laser fluences 186
Figure 35 Evolution of normal stress profiles at different laser fluences 188
Figure 36 Stress-strain relation at different applied laser fluences 190
Figure 37 Evolution of plastic strains at different laser fluences 192
Figure 38 Evolution of strain energy rate and normal stress at F=0.8J/cm^2 196
Figure 39 Ablation depth as a function of laser fluences 198

LIST OF TABLES

Page

Table 1 Optical, thermal, and mechanical properties of gold material 45

Table 2 Calculation of group velocity C_g for $\omega_1 = 1.0 \times 10^{11}$ Hz 109

Table 3 Calculation of group velocity C_g for $\omega_2 = 2.5 \times 10^{11}$ Hz 109

1. LITERATURE REVIEW AND INTRODUCTION

1.1. Overview

Study of transport dynamics in materials in response to ultrafast laser heating is essential for fabricating microstructures [1] – [3]. The threshold ablation fluence is typically lower for ultrafast lasers than for nanosecond lasers [4]. Ultrafast laser processing also produces significantly reduced or negligible heat-affected-zones (HAZs) in the surrounding region of the ablated area. The feature is well explored for the high-quality fabrication of soft and hard materials demanding nanoscale spatial resolution [4]. This is because the pulse duration of an ultrafast laser is much shorter than the thermal relaxation time of the electron-phonons and the characteristic time (~10^{-9} s) for normal evaporation [5] and [6]. And lattice temperatures stay lower than the melting point of the material during the ultrafast laser ablating process at relatively low input intensity [7]. Ultrafast lasers are being applied to explore innovative micro-fabrication and new materials alike. However, the physics behind femtosecond laser-matter interaction at nanoscale (with the cross-section smaller than 100 nm) is yet to be established [8].

Ultrashort lasers are considered beneficial to micromachining. Physical damage and change of surface morphology resulted from thermal melting and re-solidification using conventional lasers can be circumvented by applying ultrafast laser pulses below the ablation threshold [7]. Using light laser intensity can effectively avoid fraction vaporization, excessive mass removal, and physical damage, thus having important

implications for 3D mapping, high quality micromachining of brittle materials, substrate scribing, and surface patterning [4], to name only a few.

When a below melting threshold ultrafast pulse is applied, the irradiated target would undergo to a rapid phase transition that involves the nucleation of a liquid layer at the solid-vapor interface and the receding of melted layer into the bulk with a receding velocity as indicated by Refs. [4], [6] and [7]. The phase transition is characterized by rapid melting, vaporization and resolidification, all attributed to lattice temperatures exceeding the melting point and the saturation temperature [2]. At a sufficiently high excitation, the target experiences superheating at a time scale that is shorter than the one that dictates normal melting. Superheating and lattice instability lead to the formation of liquid-gas mixture of the target material due to the phase explosion.

Nevertheless, surface morphology by ultrafast laser processing does not always deal with material removal through phase transition or explosion and denotes a different mechanism without fully understood. As one experiment investigates the laser fluence effect on ultrafast laser ablation and reveals the fact that laser-induced material removal can be completed by low laser intensity and indicates the sub-melting with the absence of phase transition or explosion since the lattice temperature does not exceed the equilibrium melting or critical temperature, and no molten has been traced [1]. Therefore, the ablation mechanism of phase transition or explosion are not qualified to explain the material removal process caused by the ultrafast laser with light intensities. The observed formation of optical interference patterns at low laser intensity and the disappearance of Newton rings which are observed at high laser intensities indicate the major role of

thermally induced mechanical deformation during the ablation process in low fluence regime [12]. The similar investigations has also been conducted for enhancing machining quality and accuracy by femtosecond laser processing and obtain the similar observation: no obvious molten debris exists at the ablated area morphology with the low-fluence regime [6]. And the resultant material ejection after the laser shot with low fluence is mainly caused by the spallation of fractured layers or fragmentation when tensile stress goes beyond the strength limit [14] rather than the normal vaporization. Consequently, the ablation mechanism in the regime around the ablated threshold is primarily contributed by the thermomechanical coupling and the following surface change due to material ejection (photomechanical spallation) rather than the phase transition or explosion. The fundamental knowledge is consisted by thermodynamics regarding laser-material interaction, thermal-induced mechanical response and the ejection due to fragmentation and mechanical spallation, and is the key to the explanation of the femtosecond ablation at light-intensity and the subsequent surface morphology. The extension of this study of thermal-induced stress wave propagation can also be applied on those open problems, i.e. incubation effect [15] – [19] with single- or multi- laser shots at low fluences on various kinds of solid materials.

Laser-induced removal technology on polycrystalline materials have gain much attention in recent industrial fabrication since the main advantage of relatively low price and high efficiencies of such materials. For example, laser processing has become a key technology for the industrial production of polycrystalline silicon solar cells to reach higher conversion efficiencies where the material costs are significantly reduced [21]. In

the past decades, the research on metal ablation with ultrafast lasers have also received a great number of worldwide interests [21] – [24], for example, metallic thin film is widely used as interconnects in semiconductors and micro-electromechanical systems, the increasing interest in operating ultrashort laser heating also motivates the micro-fabricating of polycrystalline metallic targets [25], [26]. Moreover, most metals are commonly found in polycrystalline form. That is, the material is composed of many grains and grain boundaries. It is proved that both the electrical and thermal properties of metal vary by the change of averaged grain size and the additional grain boundary scattering when the thickness is comparable to the electronic mean-free-path [26]. These features inherently provide the additional complexity for the analysis on the ablation mechanism of laser-material interaction of polycrystalline metallic target. Therefore, the essential knowledge based for characterizing microstructures of polycrystalline metallic target is also required and the macroscopic quantification of carrier behavior is necessary to be taken into account in the energy transport of electrons. Lacking fundamental understandings or comprehensive theory of a non-melting ablation mechanism impacts the broader investigation and application of ultrafast laser to be reliable and effective.

This research aims to establish the fundamental understanding and formulate a comprehensive description for the mechanism of the coupled thermal and mechanical dynamics as the material interaction between the ultrafast laser pulse and polycrystalline metallic target. Apart from experimental researches, nevertheless, publications on electron-lattice energy transport descriptions and fundamental studies of ablation mechanism are rare. Ultrafast laser irradiating on materials evokes a large variety of

complex dynamics that involves laser absorption, particle emission, carrier current flow, thermal diffusion, electron-phonon interaction, coupled thermal-mechanical generation, mechanical layer ejection and induced stress wave propagation. Thus, the preliminary investigations are essential to be completed and understood before finalizing the simulation of coupled thermo-mechanical dynamics on polycrystalline metals by the ultrafast laser ablation.

Although experimental investigations on the property and microstructure of polycrystalline metallic films are plenty [26], [28] and [29], nevertheless, publications on electron-lattice energy transport model and the induced thermo-mechanical response to ultrashort pulse laser heating are few and far between. When the dimensions of focal volume become comparable to the electron mean-free-path, the material properties are found to be greatly reduced from the corresponding bulk value [26]. In addition to providing the essential knowledge base for characterizing microstructures when film thickness is comparable to electronic mean-free-path, many experimental and theoretical studies indicate that scattering of carrier current from grain boundaries is prominent. Commonly viewed as the macroscopic quantifications of carriers in the transport of electron energy in polycrystalline thin films, electron thermal conductivity and electron-phonon coupling are rarely examined for the impact that size effect and surface and grain boundary scatterings have on them. Some studies are therefore required to be reviewed and examined in this study to identify the proper polycrystalline electrical and thermal conductivities in ultrashort laser heating.

The modeling of ablation dynamics by ultrafast laser irradiating is recently popular by introducing the molecular dynamics (MD) for the particle ejection, such as molecules and clusters [4]. Although MD provides the detailed information on the microscopic description of laser-material interaction and the ejection of molecules or liquid droplets in the localized surface region, it is not appropriate and inefficient for investigating the macroscopic thermo-mechanical coupling and obtaining the corresponding response in a long time-scale due to the intensive computation. On the contrary, for macroscopically describing the energy transport dynamics for both electron and lattice subsystems, the two-temperature model is proved to be efficient and valid in simulating for a long time scale. The derived two-step parabolic model [30] admits the energy inequality between electron and lattice subsystem during laser absorption and non-equilibrium process. However, it neglects the physical timescale and the corresponding thermal relaxation time, thus renders an infinite thermal diffusion speed. The model was adopted and improved to take into account the electron current behavior induced by the carrier emission during the ultrafast laser ablation process [3] and [8]. The two-temperature model further proposed by Qiu and Tien introduces the electron heat flux equation that reveals the hyperbolic nature for energy transport in electron subsystem [33]. And the model is then extended from Chen by introducing the lattice relaxation time constant in the heat flux equation [34], which significantly refines the lattice heat conduction into a hyperbolic manner. However, the more comprehensive model for the entire ablation process associated with a relative long time span is still few with the following considerations,

Firstly, none of the mentioned theories consider thermomechanical coupling or the induced mechanical disturbance at sub-ps scales. The lack of insight into the effects of thermomechanical coupling on electron-lattice energy transport will overestimate the thermal diffusion or induce the inadequacy for modelling the dynamics involved in the ultrafast laser irradiation.

Secondly, the involving thermophysical properties are not proper for characterizing the microstructures and reflecting the grain size effect or film thickness on the electronic carrier behavior and the following energy transport in the electron subsystem.

Thirdly, the current theoretic are still inadequate in incorporating the involved dynamics, such as the carrier (electron and ion) emission in the ultrafast laser ablation when the ablated threshold is reached. The ejection of hot electrons from target surface and the corresponding electronic current transport inside the target dissipate a large amount of energy during the intensively competing process of energy diffusion by electron-electron collisions. Therefore, the investigation of the electron emission and incorporation of the associated energy change is necessary for ensuring the energy conservation.

Fourthly, the coupled thermoelasticity was investigated and adopted as the consideration of thermo-mechanical coupling and was introduced as the energy dissipation term into the lattice energy transport equation by Qi and Suh [45] and [46]. However, when employed laser intensity is sufficient large, material behaves no longer elastic, instead, it behaves plastic. Therefore, additional energy term induced by the plastic work

done needs to be incorporated in the lattice energy transport dynamics as the contribution on the irreversibly dissipated energy loss when material becomes inelastic.

The present study aims to address the above deficiencies mentioned from the current classical two-temperature models with the formulation of more comprehensive models for depicting the thermo-elasto-dynamics, and thermo-elasto-plasto-dynamics in polycrystalline metals induced by ultrafast laser pulses, respectively.

At the experiment of ultrafast laser irradiation with extremely low laser fluence, it demonstrated that the lattice temperature changes generate the thermal stress waves which are characteristic as dispersive, broad in frequency bandwidth and of extremely high power density [37]. Such generated short-time scale shock waves due to rapid temperature change, however, cannot be estimated by the ablation threshold since no melting occurs, and always ignored by the classical heat conduction model with no consideration of thermo-elasticity as mentioned above. Therefore, the mechanism of thermo-elasto-dynamics in polycrystalline metals induced by ultrafast laser with extremely low fluence is necessary to be investigated at first for the following reasons:

(1) There are significantly less efforts and few publications, experimental as well as theoretical, reported on coupled thermal-mechanical field responses to ultrafast laser heating, since the damage cannot be evaluated or estimated by non-thermal melting threshold without generating high lattice temperature or high magnitude of stress with the irreversible deformation;

(2) The electron temperature rise is responsibly related to the reflectivity, thus it is appropriate to verify the theoretical model by comparing the simulated

normalized electron temperature change to the measured reflectivity change obtained through thermoreflectance technology (TTR) [38];

(3) The experiment of micro-damage or crack formation in single crystalline material by the thermo-elastic stress generated by the ultrafast laser heating with light or extremely low intensities has already reported and analyzed [39]. But the underlying physical mechanism on micro-cracking in polycrystalline metallic targets irradiated by the ultrafast light laser is quite different due to the isotropic behavior and lacks a proper understanding;

(4) The comprehensive investigation of ultrafast laser-induced thermo-elasto-dynamics allows the in-depth study on the significant characteristics of the thermal-induced elastic stress wave propagation and the mechanism for the initiation of micro-cracking due to the negative impact of the generation wave propagation;

(5) The study on thermo-elasto-dynamics provides an essential correlation between the ultrafast laser input parameters, specific properties with the macroscopic quantification of microstructures of polycrystalline metallic target, the eventually generated thermo-elastic waves and the criterion for inducing the initiation of micro-cracking, but also the preliminary base for the thermo-elasto-plastic dynamics involved in the ultrafast laser non-thermal ablation. Since more complex dynamics are involved when ablation occurs, the model for thermo-elasto-plasto-dynamics can be further developed based on the established model by considering additional dynamics in both electron and lattice subsystem.

The present research addresses the above comments to develop the generalized model for the description of ultrashort laser pulse induced thermo-elasto-dynamics response in polycrystalline metallic target. To resolve the insufficiency of low dimensionality for properly describing both longitudinal and lateral stress wave propagation due to neglecting the lateral distributions of laser energy absorption and heat diffusion, a three-dimensional model that governs the transport dynamics is demanded and thus developed for exploring the initiation mechanism of micro-cracking induced by the generated thermal stress waves. Considering the isotropic behavior of the polycrystalline material and assuming an asymmetry of the irradiated laser beam, the model can reasonably represented by an axisymmetric geometry in the cylindrical coordinates. The inherent complexity of the numerous coupled governing equations of motion renders the use of conventional finite difference method inefficient for numerically resolving the thermal-mechanical field responses. In addition to the primary variables such as electron and lattice temperature, the first order spatial derivative terms as electron and lattice heat flux term, shear stress, and velocity variables also need be time-integrated. A finite different method with staggered grids in [45] and [46] is employed in the study to address the noted complexity. All primary variables are resolved at grid points. The velocity fields and the first-order spatial derivative terms are determined halfway between two consecutive grid points. Shear stresses are calculated at the center location surrounded by velocity components. By using the staggered-grid finite difference scheme along with a sufficiently small time step, numerical oscillations are properly controlled and avoided.

As mentioned, the ablation mechanism and the underlying physical dynamics in submelting conditions of polycrystalline metals induced by the ultrafast laser heating lacks of a comprehensive and thorough elucidation. And few studies provide the thorough sketch starting from laser input irradiation to final surface deformation and the crater formation over a long time-scale. It is commonly admitted that the hot electrons behaves as a 'free-electron gas' due to photoexcitation at a femtosecond scale, which its velocity can approach the Fermi velocity [9]. Due to laser irradiation, the electron-electron collisions instantaneously occur in the energetic electron subsystem when these highly excited electrons approach the Fermi energy. During and after the electron thermalization, energetic electrons emit from the target surface, and its time-scale can last to a few tens of picosecond [21]. The electrons emit from target into air by overcoming the potential barriers and induce the ion ejection due to double layer effect and then cause the plasma formation. Simultaneously, ions in the lattice subsystem remain cold and then the lattice temperature gradually increases due to electron-lattice interaction over a few picoseconds. As stated, heat-affect-zone or melting is impossible to occur with light-intensity laser radiation and submelting condition, indicating that the lattice temperature in the ablated region cannot exceed the melting temperature. Due to thermomechanical coupling, the heat propagation and thermal expansion paves the way for tensile stress at the location used to be compressive a few moment ago. Moreover, such a tension-compression alternation of stress becomes more prominent with high thermal strain rate. When the laser fluence increases closely to the ablation threshold, the solid material no longer behaves reversibly. Although lattice temperature is still far below the melting

temperature, the high gradient of temperature, in turn, results in the induced mechanical stress exceeds the elastic limit as the onset of plasticity, causing the dislocation motion [19], [24] and [26]. The material behaves elasto-plastically with the accumulation of plastic strain when it yields. When the tensile stress reaches the fracture strength or the criterion for the strain energy, mechanical spallation occurs with larger amount of fragmentation or fracture layers ejecting by the repulsive force over tens of picoseconds [9].

This dissertation aims to provide a comprehensive knowledge base needed for establishing the mechanism that governs ultrafast laser-material interaction involving light fluence that is close to the ablation threshold. To figure out the necessary involved thermo-elasto-plasto-dynamics and ablation mechanism induced by ultrafast laser irradiation, the electron emission mechanism, including both photoelectric- and thermionic emission, are investigated and evaluated based on the selected laser parameters. And effect of emission and the corresponding electronic transport dynamics is considered into the electron energy balance process. The non-linear kinematic hardening model for describing the thermal-induced elastic-plastic dynamics is incorporated in constitutive model by taking into account the tension-compression alternative behavior and is further coupled into the lattice energy transport through energy dissipated term due to either thermo-elastic coupling or plastic work done. The integration for the nonlinear kinematic model is inherent complicated since it involves in different conditions like initial loading, unloading and reloading. Moreover, both the yield back-stress and yield stress need to be updated for each computing step associating with the

increase of accumulated plastic strain. And the compression-tension alternation is also related to the Bauschinger effect as one primary effect and thus introduces the complexity in the actual implement of the time-integration. Therefore, a more specific illustration of procedure and the discretization of all the field equations are required to illustrate the entire numerical iteration. Consequently, the model of thermo-elasto-plasto-dynamics can be further applied as the anticipation of ablation threshold and crater depth with certain input parameters of ultrafast lasers heating onto different kinds of polycrystalline metals.

1.2. Research Objective

The dissertation seeks to understand the mechanism that underlies ultrafast ablation and the behaviors of polycrystalline materials in response to optical energy over a long time-scale. The objective of this research is to address all the mentioned issues to better describe the thermo-elasto-dynamic and thermo-elasto-plasto-dynamic responses polycrystalline metals. Thermally induced elastic stress wave propagation will be investigated to provide a comprehensive understanding for the initiation of micro-cracking commonly experienced during non-thermal heating. Ablation mechanism behind non-thermal ablation involving no melting will be established to quantify two severe types of thermo-elasto-plasto-dynamic responses; namely, material fracture and eventual material ejection. To meet the research object the following tasks are identified:

(1) Investigate the grain size effect on metallic thermomechanical response due to scattering of the surface and grain boundaries;

(2) Provide the proper mathematic algorithms of thermophysical properties taking into account the grain size effect and temperature-dependence;

(3) Preliminarily establish a one-dimensional model to consider the grain size effect and temperature-dependent of material properties, the hyperbolic nature of heat transport, and thermomechanical coupling for describing the thermo-elasto-dynamics in polycrystalline metals induced by a single pulse of ultrafast laser heating;

(4) Examine the preliminary results of thermo-elasto-dynamic model through the physical data and reveal the size effect on thermal and mechanical fields;

(5) Refine the energy transport equations and constitutive equations taking into account the lateral effects on both thermal and mechanical field, and establish a three-dimensional model for thermo-elasto-dynamics;

(6) Establish the staggered-grid finite difference scheme and numerically solve the coupled PDEs up to tens of picoseconds;

(7) Investigate the size effects and propagation of the mechanical waves, for example, stresses and displacements, obtained by the three-dimensional model;

(8) Explore the characteristics of the propagated thermal-induced elastic stress waves with the use of time-frequency analysis;

(9) Based on the frequency spectrum of the propagated stress waves, calculate the power density as an important gauge in fatigue damage and determine the potential damage;

(10) Investigate the electron/ion emission mechanism induced by ultrafast laser heating with sufficiently high intensity and the corresponding electronic transport dynamics inside the irradiated target;

(11) Investigate the constitutive model for describing elasti-plastic behavior with the consideration of feature of compression-tension alternation induced by rapid thermal heating;

(12) Finalize the model in (3) by refining the energy transport with emission dynamics and mechanical response by elasto-plasticity for the thermo-elasto-plasto-dynamics in ultrafast laser ablation;

(13) Build the numerically discretized scheme for the coupled PDEs involved in the thermo-elasto-plastic model;

(14) Investigate the generated electrical fields and determine the onset of Coulomb explosion with the selected ultrafast laser pulse heating on the polycrystalline metals;

(15) Identify the occurrence of fracture in tensile stress and determine the crater depth due to the mechanical material ejection.

1.3. Dissertation Outline

Ultrafast laser induced thermal-mechanical responses in polycrystalline metals, including both thermo-elasto-dynamics and thermo-elasto-plasto-dynamics, and the ablation mechanism behind it were mentioned above as the research objective. The dissertation is organized as follows. Chapter 2 presents a one-dimensional, thermo-elasto-dynamic model derived to consider the impact of quantization of macrostructure and grain size on the thermophysical properties in polycrystalline metallic films. The thermo-elasto-dynamic model is further developed into a three-dimensional formulation in Chapter 3. The physical bases for initiating micro-cracking by ultrafast laser-induced thermal elastic

stress waves in polycrystalline metallic films are given demonstrated in Chapter 4. Chapter 5 presents the computational and discretization schemes developed for numerically solving the thermo-elasto-plasto-dynamic model. Near-field dynamic responses of the electrons and thermal-mechanical fields along with their implications for fragment ejection are discussed in Chapter 6. More concluding remarks are given in Chapter 7.

1.4. References

[1] Gamaly, E. G., Rode, A. V., and Luther-Davies, B., "Ablation of Solids by Femtosecond Lasers: Ablation Mechanism and Ablation Thresholds for Metals and Dielectrics," *Physics of Plasmas*, Vol.9, No.3, 2002, pp.949-957.

[2] Pecholt, B., Vendan, M., Dong, Y., and Molian, P., "Ultrafast Laser Micromachining of 3C-SiC Thin Films for MEMS Device Fabrication," *The International Journal of Advanced Manufacturing Technology*, Vol. 39 No. 3-4, 2008, pp. 239-250.

[3] Yasseen, A. A., Zorman, C. A., and Mehregany, M., "Surface Micromachining of Polycrystalline SiC Films Using Microfabricated Molds of SiO/sub 2/and Polysilicon," *Journal of Microelectromechanical Systems*, Vol. 8, No. 3, 1999, pp. 237-242.

[4] Sugioka, K., and Cheng, Y., "Ultrafast lasers—reliable tools for advanced materials processing." *Light: Science & Applications*, Vol. 3, No. 4, 2014, pp. 149.

[5] Bulgakova, N. M., Stoian, R., Rosenfeld, A. Hertel, I. V., Marine, W. and Campbell, E. E. B, "A general continuum approach to describe fast electronic transport in

pulsed laser irradiated materials: The problem of Coulomb explosion," *Applied Physics A*, Vol. 81, No. 2, 2005, pp. 345-356.

[6] Cheng, J., Liu, C. -S., Shang, S., Liu, D., Perrie, W., Dearden, G., and Watkins, K., "A review of ultrafast laser materials micromachining," *Optics & Laser Technology*, Vol. 46, 2013, pp. 88-102.

[7] Rethfeld, B., Ivanov, D. S., Garcia, M. E., and Anisimov, S. "Modeling ultrafast laser ablation," *Journal of Physics D: Applied Physics*, Vol. 50, No. 19, 2017, pp. 3001-3039.

[8] Malinauskas, M., Zukauskas, A., Hasegawa, S., Hayasaki, Y., Mizeikis, V., Buividas, R., and Juodkazis, S., "Ultrafast laser processing of materials: from science to industry," *Light: Science & Applications*, Vol. 5, 2016, pp. e16133.

[9] Labutin, T. A., Lednev, V. N., Ilyin, A. A., and Popov, A. M., "Femtosecond laser-induced breakdown spectroscopy," *Journal of Analytical Atomic Spectrometry*, Vol. 31, No. 1, 2016, pp. 90-118.

[10] Hendel, R. "Lasers Play a Significant Role in the Development of New Production Processes in Photovoltaics," *Laser Technik Journal*, Vol. 5, No. 1, 2007, pp. 32-35.

[11] Zhigilei, L. V., Lin, Z., and Ivanov, D. S., "Atomistic modeling of short pulse laser ablation of metals: connections between melting, spallation, and phase explosion," *The Journal of Physical Chemistry C*, Vol. 113, No. 27, 2009, pp. 11892-11906.

[12] Rethfeld, B., Sokolowski-Tinten, K., Von der Linde, D., and Anisimov, S. I., "Ultrafast thermal melting of laser-excited solids by homogeneous nucleation," *Physical review B*, Vol. 65, No. 9, 2002, pp. 092103.

[13] Huang, J., Zhang, Y., Chen, J. K., and Yang, M., "Modeling of ultrafast phase change processes in a thin metal film irradiated by femtosecond laser pulse trains," *Journal of Heat Transfer*, Vol. 133, No. 3, 2011, pp. 031003.

[14] Nolte, S., Momma, C., Jacobs, H., Tünnermann, A., Chichkov, B. C., Wellegehausen, B. N., and Welling, H., "Ablation of metals by ultrashort laser pulses," *JOSA B*, Vol. 14, No. 10, 1997, pp. 2716-2722.

[15] Sokolowski-Tinten, K., Bialkowski, J., Cavalleri, A., von der Linde, D., Oparin, A., Meyer-ter-Vehn, J., and Anisimov, S. I., "Transient states of matter during short pulse laser ablation," *Physical Review Letters*, Vol. 81, No. 1, 1998, pp. 224.

[16] Perez, D., and Lewis, L. J., "Molecular-dynamics study of ablation of solids under femtosecond laser pulses," *Physical review B*, Vol. 67, No. 18, 2003, pp. 184102.

[17] Niso, D., Francesca, C. G., Sibillano, T., Mezzapesa, F. P., Ancona, A., and Lugarà, P. M., "Role of heat accumulation on the incubation effect in multi-shot laser ablation of stainless steel at high repetition rates," *Optics express*, Vol. 22, No. 10, 2014, pp. 12200-12210.

[18] Liu, J., Jia, X., Wu, W., Cheng, K., Feng, D., Zhang, S., Sun, Z., and Jia, T., "Ultrafast imaging on the formation of periodic ripples on a Si surface with a prefabricated nanogroove induced by a single femtosecond laser pulse," *Optics express*, Vol. 26, No. 5, 2018, pp. 6302-6315.

[19] Das, S. K., Messaoudi, H., Debroy, A., McGlynn, E., and Grunwald, R., "Multiphoton excitation of surface plasmon-polaritons and scaling of nanoripple

formation in large bandgap materials," *Optical Materials Express*, Vol. 3, No. 10, 2013, pp. 1705-1715.

[20] Tsibidis, G. D., Stratakis, E., and Aifantis, K. E., "Thermoplastic deformation of silicon surfaces induced by ultrashort pulsed lasers in submelting conditions," *Journal of Applied Physics*, Vol. 111, No. 5, 2012, pp. 053502.

[21] Leitz, K. H., Redlingshofer, B., Reg, Y., Otto, A., and Schmidt, M., "Metal Ablation with Short and Ultrashort Laser Pulses," *Physics Procedia*, Vol. 12, Part B, 2011, pp. 230-238.

[22] Hashida, M., Semerok, A. F., Gobert, O., Petite, G., and Wagner, J. F., "Ablation thresholds of metals with femtosecond laser pulses," *Nonresonant Laser-Matter Interaction (NLMI-10)*, Vol. 4423, 2001, pp. 178-186.

[23] Oh, B., Kim, D., Kim, J., and Lee, J. H, "Femtosecond laser ablation of metals and crater formation by phase explosion in the high-fluence regime," *Journal of Physics: Conference Series*, Vol. 59, No. 1, 2007, pp.567.

[24] Gallais, L., Bergeret, E., Wang, B., Guérin, M., and Bènevent, E., "Ultrafast laser ablation of metal films on flexible substrates," *Applied Physics A*, Vol. 115, No. 1, 2014, pp. 177-188.

[25] Zhang, Q. G., Cao, B. Y., Zhang, X., Fujii, M. and Takahashi, K., "Size effects on the thermal conductivity of polycrystalline platinum nanofilms," *Journal of Physics: Condensed Matter*, 18(34), 7937, (2006).

[26] Qiu, T. Q. and Tien, C. L., "Size effects on nonequilibrium laser heating of metal films," *Journal of Heat Transfer*, 115(4), pp. 842-847, (1993).

[27] Anisimov, S. I., Bityurin, N. M. and Luk'yanchuk, B. S., "Models for laser ablation," *Photo-Excited Processes, Diagnostics and Applications*, Springer, Boston, MA, 2003, pp. 121-159.

[28] Elsayed-Ali, H. E., Juhasz, T., Smith, G. O., and Bron, W. E., "Femtosecond Thermoreflectivity and Thermotransmissivity of Polycrystalline and Single-Crystalline Gold Films," *Physical Review B*, Vol. 43, No. 5, 1991, pp. 4488-4491.

[29] Hostetler, J. L., Smith, A. N., Czajkowsky, D. M., and Norris, P. M., "Measurement of the Electron-Phonon Coupling Factor Dependence on Film Thickness and Grain Size in Au, Cr, and Al," *Applied Optics*, Vol. 38, No. 16, 1999, pp. 3614-3620.

[30] Anisimov, S. I., Kapeliovich, B. L., and Perelman, T. L., "Electron emission from metal surfaces exposed to ultrashort laser pulses," *Zh. Eksp. Teor. Fiz*, Vol. 66, No. 2, 1974, pp. 375-377.

[31] Zhao, X., and Shin, Y. C., "Coulomb explosion and early plasma generation during femtosecond laser ablation of silicon at high laser fluence," *Journal of Physics D*: *Applied Physics*, No. 46, No. 33, 2013, pp. 335501.

[32] Bulgakova, N. M., Stoian, R., Rosenfeld, A., Hertel, I. V., Marine, W., and Campbell, E. E. B., "A general continuum approach to describe fast electronic transport in pulsed laser irradiated materials: The problem of Coulomb explosion," *Applied physics A*, Vol. 81, No. 2, 2005, pp. 345-356.

[33] Qiu, T. Q., and Tien, C. L., "Heat transfer mechanisms during short-pulse laser heating of metals," *Journal of heat transfer*, Vol. 115, No. 4, 1993, pp. 835-841.

[34] Chen, J. K., and Beraun, J. E., "Numerical study of ultrashort laser pulse interactions with metal films," *Numerical Heat Transfer: Part A: Applications*, Vol. 40, No. 1, 2001, pp. 1-20.

[35] Qi, X., and Suh, C. S., "Generalized thermo-elastodynamics for semiconductor material subject to ultrafast laser heating. Part I: Model description and validation," *International Journal of Heat and Mass Transfer*, Vol. 53, No. 1-3, 2010, pp. 41-47.

[36] Qi, X., and Suh, C. S., "Ultrafast laser-induced elastodynamics in single crystalline silicon part I: model formulation," *Journal of Thermal Stresses*, Vol. 32, No. 5, 2009, pp.477-493.

[37] Rabroker, G. A., Suh, C. S., and Chona, R., "Laser-induced stress wave thermometry applied to silicon wafer processing: Modeling and experimentation," *Experimental mechanics*, Vol. 45, No. 1, 2005, pp. 3-8.

[38] Qiu, T. Q., Juhasz, T., Suarez, C., Bron, W. E., and Tien, C. L., "Femtosecond laser heating of multi-layer metals—II. Experiments," *International Journal of Heat and Mass Transfer*, Vol. 37, No. 17, 1994, pp. 2799-2808.

[39] Sakakura, M., Fukuda, N., Shimotsuma, Y., and Miura, K., "Dynamics of interference of femtosecond laser-induced stress waves and crack formation inside a LiF single crystal," *In Laser Applications in Microelectronic and Optoelectronic Manufacturing (LAMOM) XIX*, Vol. 8967, 2014, pp. 89670C.

[40] Zhao, X., and Shin, Y. C., "A two-dimensional comprehensive hydrodynamic model for femtosecond laser pulse interaction with metals," *Journal of Physics D: Applied Physics*, Vol. 45, No. 10, 2012, pp. 105201.

[41] Beuton, R., Chimier, B., Breil, J., Hébert, D., Mishchik, K., Lopez, J., Maire. P. H., and Duchateau, G., "Thermo-elasto-plastic simulations of femtosecond laser-induced multiple-cavity in fused silica," *Applied Physics A*, Vol. 124, No. 4, 2018, pp. 324.

[42] Yilbas, B. S., "Short-pulse laser heating of gold-chromium layers: thermo-elasto-plastic analysis," *Journal of Physics D: Applied Physics*, Vol. 35, No. 11, 2002, pp. 1210.

2. THERMO-ELASTO-DYNAMICS OF POLYCRYSTALLINE GOLD FILMS – GRAIN SIZE EFFECTS[*]

2.1. Introduction

Study on the energy transport that underlies ultrafast laser heating has been very active. Because the pulse duration is much shorter than the thermalization time of electron-phonon interaction [1], and the threshold fluence for which ablation occurs is typically lower than when a nanosecond pulsed laser is used, ultrashort pulse laser machining is receiving increasing interest in nano- and micro-machining [1]-[3] where fabrication quality is significantly enhanced with reduced heat-affected zone. Ultrashort pulsed laser heating is explored for processing polycrystalline metallic thin films that are widely used as interconnects in semiconductors [4] and [5]. As well-known, ultrafast laser heating in materials is a complicated process that combines the laser absorption, electron-lattice equilibrium, plasma plume formation and expansion, coupled thermal-mechanical generation and thermal stress wave propagation. The dynamics involved is complex and difficult to be depicted. And it is also common that the underlying time scale that dictates the ablation mechanism is routinely ignored. However, lacking a fundamental understanding for the non-thermal ablation mechanism impacts the broader application of ultrafast lasers.

---

[*]Reprinted with permission from "Generalized Thermo-Elastodynamics for Polycrystalline Metallic Thin Film in Response to Ultrafast Laser Heating" by Xu Mao and C. Steve Suh, 2018. *International of Thermophysics and Heat Transfer*, 1-11, Copyright [2018] by the American Institute of Aeronautics and Astronautics, Inc.

Although experimental investigations on the property and microstructure of polycrystalline metallic films are plenty [4] and [6]-[8], nevertheless, publications on electron-lattice energy transport model and the induced thermo-mechanical response to ultrashort pulse laser heating are few and far between. When the dimensions of focal volume become comparable to the electron mean-free-path, the material properties are found to be greatly reduced from the corresponding bulk value [4]. In addition to providing the essential knowledge base for characterizing microstructures when film thickness is comparable to electronic mean-free-path, many experimental and theoretical studies indicate that scattering of carrier current from grain boundaries is prominent. Commonly viewed as the macroscopic quantifications of carriers in the transport of electron energy in polycrystalline thin films, electron thermal conductivity and electron-phonon coupling are rarely examined for the impact that size effect and surface and grain boundary scatterings have on them. Some studies are therefore required to be reviewed and examined in this study to identify the proper polycrystalline electrical and thermal conductivities in ultrashort laser heating.

At the experiment of ultrafast laser irradiation with extremely low laser fluence [9], it demonstrated that the lattice temperature changes generate the thermal stress waves which are characteristic as dispersive, broad in frequency bandwidth and of extremely high power density. Such generated short-time scale shock waves high-possibly causes the initiation or creation of micro-cracking. Such damage, however, cannot be estimated by the ablation threshold since no melting occurs, and cannot be investigated by the classical heat conduction model with no consideration of thermo-elasticity. Therefore, in

order to precisely describe both the electron and lattice energy transport dynamics in a wide-range of time-scale and simultaneously obey the energy conservation in progress, be applicable to consider the grain size effects by varying film thicknesses and averaged grain diameters, and provide the reasonable evidence for the initiation of micro-cracking in the thermo-elastic stress field, developing the comprehensive and essential knowledge regarding the thermo-mechanical coupled field is primary.

Moreover, different electron and lattice energy transport models are also reviewed. The concept of energy transport was first proposed by Kaganov. Anisimov further derived a phenomenological two-step parabolic model that neglects thermal relaxation time and renders an infinite energy transport speed [10]. Qiu and Tien presented a more general two-step hyperbolic model to resolve the dilemma of energy transport by considering electron and phonon relaxation times [11]. Van Driel also modelled the non-equilibrium process by considering heat diffusion based on carrier density [12]. The model was found to agree well with experimental results by many [13] and [14]. However, the above models do not take into account neither of the downward movement of the top surface during the electron-lattice transport or the thermal-mechanical interaction at sub-ns scales [17], which is the coupled thermal-elastoplastic deformation. Moreover, the temporal evolution of dynamics induced by the ultrafast laser heating is required to be checked and verified to ensure the consistency in the entire optical process, thus obeying the conservation of energy.

Considering the complexity of modelling laser-induced thermo-stress wave propagation in three-dimension and the further reliability for initiating micro-cracking, the

primary work is to investigate the proper description of important thermophysical properties that govern energy transport, investigate the size effects on the resulted thermal-mechanical field of metallic thin films and bulk, respectively, and the one-dimensional model for depicting thermo-elasticity in the laser-irradiating direction and the validation for applying the established model.

In the section that follows, a one-dimensional model is presented for the description of ultrashort laser pulse induced thermo-elastodynamic responses in both single- and poly-crystalline metallic films. When the spot size is much greater than the optical penetration depth, the lateral deviation of ultrafast laser absorption or diffusion can be assumed to be negligible and thus, it is capability to employ the model which is one-dimensional. The thermal-mechanical field equations are derived from a hyperbolic two-step temperature model incorporating a term of energy dissipation to the generation of thermal-induced mechanical disturbance which is the thermo-elasticity. Size effects due to film surface and grain-boundary scatterings on thermophysical properties that characterize the energy transport of electrons are in-depth investigated for their impact on the response of the single- and polycrystalline metallic films. Therefore, electron energy transport in polycrystalline thin film is further applicable by considering temperature-dependence and size effects incorporating both film surface and grain boundary scattering. Using the one-dimensional model, the numerical results of a single-crystalline gold film is favorably examined against published experimental data, thus validating the model. The parametric study with different sets of film thickness and averaged grain diameter is determined to investigate the coupled thermal-mechanical response for polycrystalline

crystalline gold films, and the impact of size effect on single- and poly-crystalline films is analyzed. The section provides the fundamental knowledge essential for establishing a comprehensive understanding of the underlying mechanism governing ultrafast laser heating and the induced stress distribution using formulation of higher dimensionality.

2.2. Thermophysical Properties of Polycrystalline Metals

2.2.1. Electron Heat Capacity

Material properties that characterize the ultrashort laser-target interaction are commonly assumed to be temperature-invariant for simplicity. This inevitably leads to a simplified description of linear electron diffusion. Linear thermophysical properties are supported by experimental data acquired under specific conditions for electron heat capacity and electron thermal conductivity [26] and [27]. Comparison between theoretical calculation and experimental data available in [28] shows that the normalized electron temperature predicted by the two-temperature model using constant electron heat capacity and electron thermal conductivity agrees well with physical measurements. Moreover, the electron temperature T_e is much lower than the Fermi temperature and that the electron heat capacity C_e is proportional to T_e as $C_e(T_e) = C_{eo}T_e$ [27].

However, the linear behavior is only valid for a certain range of electron temperature. When electron temperature increases comparably with the Fermi temperature, the electron heat capacity and electron thermal conductivity varies nonlinearly. A remedy was presented by Jiang [29] that considered quantum effect and incorporated the Fermi-Dirac distribution. Based on the work of Jiang's, Chen *et al* [15] approximated C_e in four definitive ranges of electron temperature. The approximation

imparts temperature-dependent nature to electron heat capacity for metallic films and renders practicality to theoretical work as follows:

$$\begin{cases} C_e(T_e) = C_{eo} T_e \quad , & T_e < T_F / \pi^2 \\ C_e(T_e) = 2C_{eo} T_e / 3 + C_e^{'} / 3 \quad , & T_F / \pi^2 \le T_e < 3T_F / \pi^2 \\ C_e(T_e) = nk_B + C_e^{'} / 3 \quad , & 3T_F / \pi^2 \le T_e < T_F \\ C_e(T_e) = 3nk_B / 2 \quad , & T_e \ge T_F \end{cases} \tag{1}$$

With

$$C_e^{'} = C_{eo} \frac{T_F}{\pi^2} + \frac{\frac{3}{2} nk_B - C_{eo} \frac{T_F}{\pi^2}}{T_F - \frac{T_F}{\pi^2}} \left(T_e - \frac{T_F}{\pi^2} \right) \tag{2}$$

and C_{eo} being a coefficient, n the number density of free electron, k_B the Boltzmann constant, and T_F the Fermi temperature. During non-equilibrium, electron thermal conductivity and electron-phonon coupling factor macroscopically demonstrate electron thermalizing via electron-electron collision and electron-phonon interaction. Furthermore, it has been shown that when film thickness becomes comparable to the electronic mean-free-path, the electrical and thermal conductivities are found to be reduced from the corresponding bulk value. As for polycrystalline metallic thin films, since the grain size is of the same order as the film thickness and electron mean-free-path, these two properties specific to polycrystalline films also differ from their single crystalline counterparts. Film thickness along with size effect is therefore significant for determining the thermophyscial properties of metallic thin films.

2.2.2. Grain Size Effect on Film and Grain Boundary Scattering

All the literature reviewed above focus exclusively on the electron-lattice energy transport process in single crystalline materials that interact with femtosecond laser pulses.

Compared with the number of reports on investigating and characterizing polycrystalline nano-films [6]-[8] using physical apparatus of one kind or the other, publications on modelling the thermal-mechanical response of polycrystalline metallic materials in response to ultrafast heating are significantly fewer. Many a physical and theoretical study suggest that (1) film surface and grain boundary scatterings contribute to the increase in carrier resistivity and (2) material thermophysical properties are strongly dependent on if the material thickness is of the scale of the corresponding electronic mean-free-path. Electron thermal conductivity and electron-phonon coupling, the two properties commonly viewed as the macroscopic quantification of carrier behaviors, are central to describing electron energy transport in polycrystalline thin films. Despite all the above, polycrystalline metallic film under ultrafast heating rarely considers the impact that material grain size and surface and grain boundary scatterings have on the thermo-elasto-dynamic response. Therefore, the thermophysical properties, including electron thermal conductivity and electron-phonon coupling factor, are firstly investigated with related to the surface film and grain boundary scattering and the corresponding film thickness.

2.2.3. Electron Thermal Conductivity

Size effect is a type of resistivity in the transport mechanism of polycrystalline metallic films. A theoretical model was developed to explain the increase of electrical resistivity in thin metal films with decreasing thickness [31]. Surface scattering is considered the main mechanism for such a phenomenon [30]. Nevertheless, grain boundaries also attribute to electron scattering, thus an additional resistivity needs to be incorporated to obey the Matthiessen's rule. Consequently, Mayadas and Shatzkes [31]

extended Fuchs' work by introducing grain boundary scattering to address the situation when thickness and averaged grain size are comparable to the corresponding electron mean-free-path. Both film surface and grain boundary scatterings impede charge transport (flowing of carriers). By considering size effect along with the electron mean-free-path $\Lambda(T_l)$, Qiu and Tien [4] submitted the following that defines the thin-film thermal conductivity, $\kappa_{e,f}(T_e, T_l)$ with its bulk value obtained in equilibrium as

$$\frac{\kappa_{e,f}(T_e,T_l)}{\kappa_{e,b}(T_l)} = \frac{C_e(T_e)}{C_e(T_l)} \cdot \frac{\Lambda_f(T_l)}{\Lambda_b(T_l)} \tag{3}$$

Note that Eq. (1) indicates decreasing thermal conductivity (from the bulk value) when the film dimension approaches the electron mean-free-path. Before deriving the electron thermal conductivity for metallic thin films, temperature-dependence is considered. The expression in Eq. (4) is valid for approximating $C_e(T_e)/C_e(T_l)$ when the electron temperature T_e is varied between the Debye temperature, T_D, and $0.1T_F$ [29] and [32],

$$\frac{C_e(T_e)}{C_e(T_l)} = \frac{T_e}{T_l} \tag{4}$$

The temperature-independency featured in the equation suggests that it would not be proper to use the approximation to profile the temperature distribution associated with damage threshold. A more general expression was introduced by Anisimov [33] that has been shown to be in good agreement with experimental data for a wide range of electron and lattice temperatures,

$$\frac{C_e(T_e)}{C_e(T_l)} = \frac{\left(\varphi_e{}^2 + 0.16\right)^{5/4}\left(\varphi_e{}^2 + 0.44\right)\varphi_e}{\left(\varphi_e{}^2 + 0.092\right)^{1/2}\left(\varphi_e{}^2 + \eta\varphi_l\right)} \tag{5}$$

Where $\varphi_e \equiv T_e/T_F$ and $\varphi_l \equiv T_l/T_F$ are the normalized electron and lattice temperature and $\eta = 0.16$ is a constant.

For low normalized temperatures, $\varphi_e \ll 1$, the general expression is reduced to the approximation in Eq. (4). It is noted that at a high normalized temperature, $\varphi_e \gg 1$, when the damage threshold is reached and the electron gas becomes non-degenerative, the general equation results in the well-known dependence, $\kappa_e \sim T_e^{5/2}$, which is characteristic of low-density plasma.

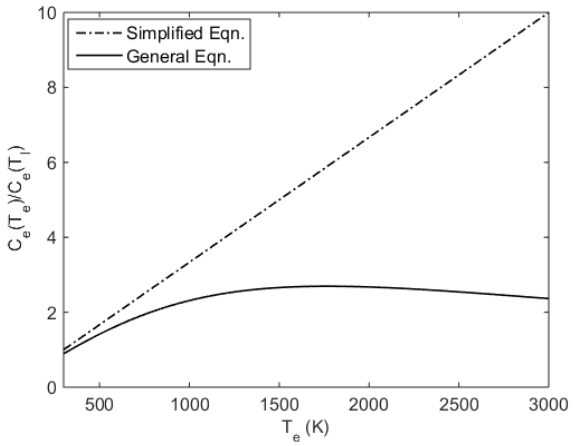

Figure 1. $C_e(T_e)/C_e(T_l)$ as a function of electron temperature

Figure 1. demonstrates the significant difference between the simplified formula $C_e(T_e)/C_e(T_l) = T_e/T_l$ and the revised expression in Eq. (5). As seen in the figure, at

relatively low temperatures in which $T_D < T_e < 0.1T_F$, the two ratios as described by Eqs. (4) and (5) coincide, suggesting that $C_e(T_e)/C_e(T_l)$ can be approximated using the simple relation defined in Eq. (4) when a low laser fluence is involved. When the electron temperature is higher than $0.1T_F$, the two deviate from each other with the approximation increasing linearly while the general expression reaching a peak before trailing off. Thermal conductivity described by the simplified approximation is no longer valid when temperature reaches up to 1,000K. Thus, when a laser fluence is close to or above the ablation threshold, the general expression ought to be followed for the determination of the electron thermal conductivity.

The simple relation $C_e(T_e)/C_e(T_l) = T_e/T_l$ was further modified by Qiu and Tien to approximate the electron thermal conductivity ratio,

$$\frac{\kappa_{e,f}(T_e,T_l)}{\kappa_{e,b}(T_l)} = \frac{C_e(T_e)}{C_e(T_l)} \cdot \frac{\Lambda_f(T_l)}{\Lambda_b(T_l)} = \frac{T_e}{T_l} \cdot \frac{\Lambda_f(T_l)}{\Lambda_b(T_l)} \tag{6}$$

Electrical conductivity in thin films is a sensitive function of surface and grain boundary scatterings [31]. As is dictated by the Widemann-Franz Law [4], the corresponding thermal conductivity is also related to the electrical conductivity at high temperature. Such a correlation is made explicit in Eq. (7) which defines the ratio of the electron mean-free-path of the thin film material with the electron mean-free-path of its bulk material [4] as,

$$\frac{\Lambda_b}{\Lambda_f} = 1 - \frac{3}{2}\alpha + 3\alpha^2 - 3\alpha^3 \ln\left(1+\frac{1}{\alpha}\right) - \frac{6(1-P)}{\pi\beta}\int_0^{\pi} d\theta \int_0^1 \times \frac{\cos^2\theta}{H^2}\left(u-u^3\right)\cdot\frac{1-\exp\left(-\beta H/u\right)}{1-P\exp\left(-\beta H/u\right)}du \tag{7}$$

Where the grain diameter parameter $\alpha = R_f\,\Lambda_b/\left(1-R_f\right)/D$, $\beta = L/\Lambda_b$ is the film thickness parameter, R_f is the grain boundary reflectivity, L is the film thickness, and P is the specular reflection parameter at surface. Note that P is zero as the reflection of electrons at film surface is diffusive for most films. Eq. (7) can be simplified in the region defined by $\alpha < 10$ and $\beta > 0.1$ as,

$$\frac{\Lambda_f}{\Lambda_b} = \left(1+\frac{3}{8\beta}(1-P)+\frac{7}{5}\alpha\right)^{-1} \tag{8}$$

The ratio of thermal conductivity can be obtained by combining Eqs. (1) with (8),

$$\frac{\kappa_{e,f}\left(T_e,T_l\right)}{\kappa_{e,b}\left(T_l\right)} = \frac{T_e}{T_l}\cdot\left(1+\frac{3}{8\beta}(1-P)+\frac{7}{5}\alpha\right)^{-1} \tag{9}$$

Applying the general expression in Eq. (5) which is valid for a wider range of electron temperature T_e, the electron thermal conductivity ratio $C_e\left(T_e\right)/C_e\left(T_l\right)$ for polycrystalline metallic thin films is therefore,

$$\frac{\kappa_{e,f}}{\kappa_{eq,b}} = \frac{\left(\varphi_e{}^2+0.16\right)^{5/4}\left(\varphi_e{}^2+0.44\right)\varphi_e}{\left(\varphi_e{}^2+0.092\right)^{1/2}\left(\varphi_e{}^2+\eta\varphi_l\right)}\cdot\left[1+\frac{3}{8\beta}(1-P)+\frac{7}{5}\alpha\right]^{-1} \tag{10}$$

The bulk value of $\kappa_{eq,b}\left(T_l\right)$ is defined below using the electron mean-free-path obtained in the equilibrium state in Eq. (11) with the reference lattice temperature $T_l = 300$ K, and m and υ_F being the effective mass and the Fermi velocity, respectively.

$$\kappa_{eq,b}(T_l) = \frac{\pi^2 n k_B^{\ 2}}{3m\upsilon_F} \cdot T_l \cdot \Lambda(T_l) \tag{11}$$

2.2.4. Impact of Size Effects on Electron Thermal Conductivity

Per Eqs. (10) and (11), the correlation of the ratio of thermal conductivity with film thickness parameter β for polycrystalline thin films is illustrated in Figure 2. for different electron and lattice temperatures. Three averaged grain diameters D are considered for three film thicknesses as L=20D, L=10D and L=5D using P=0 and R=0.17 as the two scattering parameters.

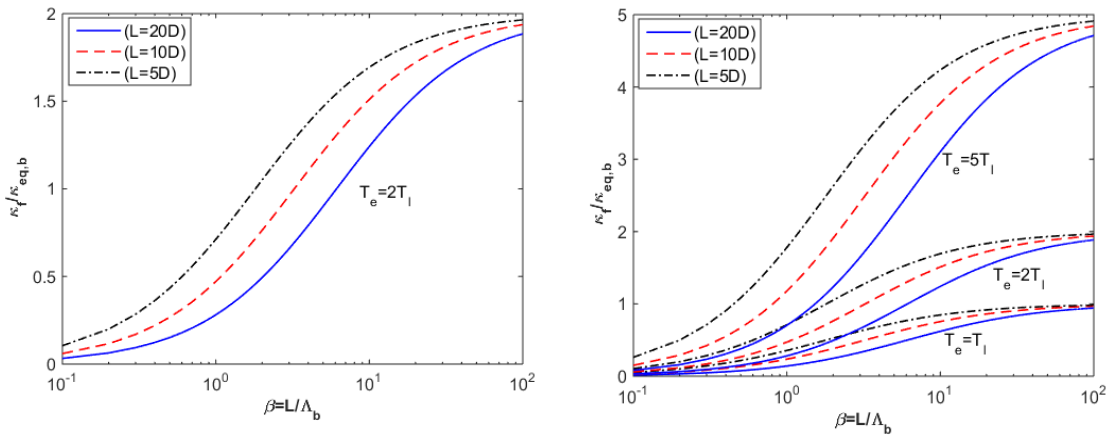

(a) **(b)**

Figure 2. $\kappa_f/\kappa_{eq,b}$ vs. β for polycrystalline films

(a) T_l=300K and T_e= 2T_l; (b) T_l=300K and T_e= T_l, 2T_l and 5T_l

Figure 2.(a) shows the impact of $\beta = L/\Lambda_b$ (size effect) on $\kappa_f/\kappa_{eq,b}$ at three different D's, where $\Lambda_b(300\text{K}) = 400$ Å is the electron mean-free-path of the bulk material

when the lattice temperature is 300K. It is seen that the size effect is prominent when $\beta < 10$. $\kappa_f / \kappa_{eq,b}$ increases significantly with increasing film thickness, thus suggesting that when the film thickness is comparable to the electron mean-free-path, the impact of grain size on thermal conductivity is significant. On the other hand, as $\beta > 10$, $\kappa_f / \kappa_{eq,b}$ is seen to approach a constant. This would necessarily mean that the impact of grain boundary scattering on thermal conductivity reduces when the film thickness is sufficiently large. In this study, the film thickness is 1000Å, thus rendering $\beta < 10$ and the associated size effect not negligible. It is necessary to investigate the averaged grain diameter as one important parameter when considering grain-boundary scattering. As more gains and grain boundaries are associated with a smaller grain diameter and that scattering from grain boundaries hinders electron thermal conduction and thermal diffusion through electron-electron collisions, $\kappa_f / \kappa_{eq,b}$ is also seen to decrease with decreasing the averaged grain diameter. Figure 2.(b) shows the effect of non-equilibrium heating on $\kappa_f / \kappa_{eq,b}$ which is highly sensitive to electron and lattice temperatures.

2.2.5. Electron-Phonon Coupling Factor

Electron-phonon (e-ph) coupling factors have been extensively investigated both theoretically and experimentally [4] and [6]-[8]. Qiu and Tien investigated the e-ph coupling factor G_f for polycrystalline films by evaluating the size effect attributable to the free-electron scattering from film surface and grain-boundary. The mean-free-path, Λ_f, is a function of the film thickness (*L*) and the averaged grain diameter (*D*),

$$\frac{G_f}{G_b} = \frac{\Lambda_b}{\Lambda_f} = 1 + \frac{3}{8\beta}(1-P) + \frac{7}{5}\alpha \qquad (12)$$

By taking into account phonon emission and absorption probability, the G_b in equilibrium is,

$$G_b = \frac{9}{16} \cdot \frac{n k_B^{\,2} T_D^{\,2} \upsilon_F}{\Lambda(T_l) T_l E_F} \qquad (13)$$

Where T_D is the Debye temperature, E_F is the Fermi energy with the corresponding electron mean-free-path Λ_b = 400Å at T_l = 300K. The calculated G_b agrees well with the averaged constant value $G = 2.2\times10^{16}$ Wm^{-3}K^{-1} obtained from measurement [8]. Simultaneously, the e-ph coupling factor can be viewed as a constant independent of the electron temperature even as T_e approaches 10,000K [8]. However, at a high ultrashort laser fluence or when the electron temperature is above 10,000K, further revision of G_b would be needed. The trend of G_f reveals that (1) the *G*-factor for polycrystalline metallic films increases with decreasing average grain diameter, as seen in Figure 3, and (2) both the magnitude and trend are shown to agree with physical data for various laser fluences [7]. Also, the *G*-factors for polycrystalline thin-films are larger than the corresponding values for single-crystalline films [6]. The magnitude of G_f agrees with the measured $G = (3.0\pm0.5)\times10^{16}$ Wm^{-3}K^{-1} that was obtained when fluence was varied from 0.4 to 1.6 mJ/cm^2 [34]. The electron thermal conductivity and e-ph coupling factor for single crystalline and polycrystalline films can be determined using Eqs. (10) and (12). It is noted that $\alpha = 0$ for single crystalline films as there are no grain-boundaries to signify

scattering when calculating the electron thermal conductivity and the electron-phonon coupling factor.

2.2.6. Impact of Size Effects on Electron-Phonon Coupling Factor

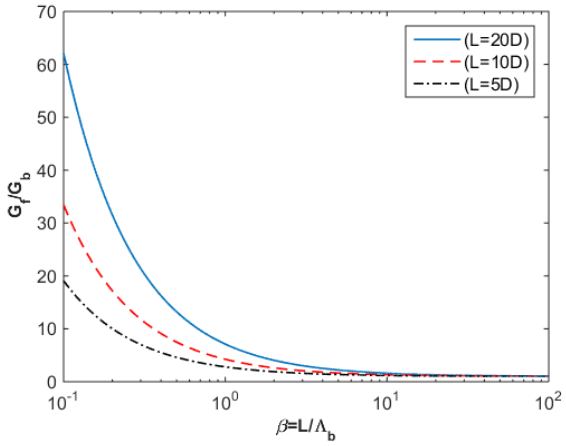

Figure 3. G_f/G_b as a function of film thickness parameter β for polycrystalline film

Per Eqs. (12) and (13), the correlation of the ratio of electron-phonon (e-ph) coupling factor G_f/G_b with the film thickness parameter β for polycrystalline thin films is illustrated in Figure 3 for 3 different averaged grain diameters (D's) that give L=20D, L=10D and L=5D. Given that the e-ph coupling factor is experimentally shown to be independent of temperature for relatively low laser fluence, the size effect of the polycrystalline gold film is investigated in the followings using Eq. (12). For $\beta > 10$, G_f/G_b approaches a constant, thus signifying negligible grain-boundary scattering. Additionally, for $1 < \beta < 10$, G_f/G_b decreases with increasing film thickness. It shows that for decreasing averaged grain diameter, G_f/G_b increases. This indicates that more

energy is transferred from the electron to lattice when grain diameter decreases with increasing number of grains. Thus, the resulted electron temperature is lower in the polycrystalline film than in the single-crystalline film.

2.3. Energy Balance Equations and Constitutive Equations

The notion of electron-phonon energy transport was conceived to understand how optical energy was involved in evolving a microscopic scale heat transfer to an eventual macroscopic description of the dynamic process. Qiu and Tien [11] developed the energy transport equations using a two-step parabolic model, admitting energy inequality and energy exchange between the electron and lattice subsystem. Moreover, the hyperbolic nature of the electron energy transport in metals is considered for an improved description of electron diffusion. Chen [15] extended Qiu and Tien's model by introducing a heat flux equation and resolved the dilemma that thermal disturbances in lattice subsystem diffuse with infinite speed. Energy loss to thermal diffusion was further revised in the one-dimensional, two-temperature model. However, one-dimensional models do not account for the thermal-mechanical interaction at the sub-picosecond scale [17]. As a remedy, several studies considering relaxation times were explored to gain insight into the effect of thermomechanical coupling on the dynamics of energy transport in metals irradiated by ultrafast lasers. Qi and Suh [18]-[20] developed a thermo-elastodynamic and a thermo-elasto-viscoplastic model that are valid for single-crystalline silicon undergoing ultrafast laser heating. It was found that, as a mode of coupled thermal-mechanical response admitted by the models, high-frequency propagating stress waves were probable at non-melting fluence [21]-[23].

2.3.1. Laser Intensity Source Term

The temporal distribution of a laser pulse is a Gaussian function given by [15] and [26],

$$S(z,t)=\sqrt{\frac{\beta}{\pi}}\frac{1-R}{t_p\delta_s}\phi\cdot\exp\left(-z\Big/\delta_s-\beta\left(\left(t-2t_p\right)\Big/t_p\right)^2\right) \tag{14}$$

Where ϕ is laser fluence, R is reflectivity, t_p is laser pulse duration, δ_s is optical penetration depth, and $\beta=4\ln(2)$. The irradiated laser energy is absorbed by free electrons in the target material. Hot electrons are initially localized within the optical penetration depth. After laser energy absorption, collisions occur between hot electrons possessing energy around the Fermi level to drive thermal diffusion into lattice. However, based on a set of physical data on Au films, Wellershoff [24] argued that an additional absorption process, namely, ballistic energy transport, needs be taken into account. When the laser fluence is relatively low, melting does not occur and film thickness exceeds the ballistic range of the optical penetration, the effect of ballistic motion and hot electron diffusion absorb energy into a deeper depth than the expected optical penetration depth. Detail definition of the ballistic range of the optical penetration depth can be found in [24] and [25]. Without considering ballistic motion, higher energy density is localized and higher electron temperature near the surface is induced compared with experimental results. As a remedy, an effective initial absorption depth is considered by incorporating an optical absorption depth δ_s and a ballistic range δ_b into the following to replace δ_s in Eq. (14),

$$\delta = \frac{\exp\left(-z/\left(\delta_s + \delta_b\right)\right)}{\left(\delta_s + \delta_b\right)\left(1 - \exp\left(-L/\left(\delta_s + \delta_b\right)\right)\right)} \tag{15}$$

Where L is the film thickness. Thus, the laser source in Eq. (14) is revised as,

$$S(z,t) = \sqrt{\frac{\beta}{\pi}} \frac{1-R}{t_p\left(\delta_s + \delta_b\right)\left[1 - e^{-L/(\delta_s+\delta_b)}\right]} \phi \cdot \exp\left(-z/\left(\delta_s + \delta_b\right) - \beta\left(\left(t - 2t_p\right)/t_p\right)^2\right) \tag{16}$$

2.3.2. Electron Energy Balance Equation

The following two-step temperature heat transfer model is derived from Boltzmann transport equation of electron. In the energy balance equation of electrons, the finite nature of energy transport is embodied by the hyperbolic heat flux equation through τ_e, the relaxation time of free electron, and the equation is obtained as,

$$\begin{aligned} C_e\left(T_e\right)\frac{\partial T_e}{\partial t} &= -\nabla \cdot q_e - G\left(T_e - T_l\right) + S \\ \tau_e \frac{\partial q_e}{\partial t} + q_e &= -\kappa_e \nabla T_e \end{aligned} \tag{17}$$

It is noted that the subscripts *e* and *l* represent electron and lattice, respectively. Specifically, in the equations above, variable T_e is the electron temperature, and q_e is the electron heat flux. The parameter C_e is the electron heat capacity, κ_e is the electron thermal conductivity, and *G* is the electron-phonon coupling factor, which governs the energy exchange between electron and lattice subsystems. And the term S is obtained by the calculation of Eq. (14) as the energy source term due to the absorption of laser intensity.

2.3.3. Lattice Energy Balance Equation

The rigorous model [15] also features a hyperbolic heat flux equation for the lattice energy transport process where the presence of the lattice thermal relaxation time, τ_l, renders a finite thermal propagation speed as follows,

$$C_l(T_l)\frac{\partial T_l}{\partial t} = -\nabla \cdot q_l + G(T_e - T_l)$$
$$\tau_l \frac{\partial q_l}{\partial t} + q_l = -\kappa_l \nabla T_l \tag{18}$$

Accounting for the thermal-mechanical interaction during the non-equilibrium process, an energy dissipation term L_M is considered in the energy balance of the lattice as [18],

$$C_l(T_l)\frac{\partial T_l}{\partial t} = -\nabla \cdot q_l + G(T_e - T_l) - L_M \tag{19}$$

Because the electron energy transferred into the lattice subsystem leads to thermal expansion and consequently initiates the propagation of mechanical waves, the following energy term is incorporated to accommodate the particular energy loss to the generation of thermoelastic response,

$$L_M = (3\lambda + 2\mu)\alpha' T_l \dot{\varepsilon}_{kk} \tag{20}$$

Where λ and μ are the Lamé constants, α' is the thermal expansion coefficient, and $\dot{\varepsilon}_{kk}$ is the rate of lattice dilation. The incorporation results in a revised Eq. (18) as follows,

$$C_l(T_l)\frac{\partial T_l}{\partial t} = -\nabla \cdot q_l + G(T_e - T_l) - (3\lambda + 2\mu)\alpha' T_l \dot{\varepsilon}_{kk} \tag{21}$$

2.3.4. Constitutive Equations for One-Dimensional Thermo-elasticity

The section presents the constitutive laws that govern the coupled thermal-mechanical behaviors of monocrystalline and polycrystalline materials in response to laser heating. Lattice deformation is the result of lattice temperature variation. When a relatively low fluence is applied, thermo-elasto-dynamics dictates and the generated mechanical response in the target material is predominantly elastic. The anisotropy of single crystalline films is not considered in the one-dimensional model formulation to be derived in the followings. The equation of motion expressed in the uniaxial coordinate is [36],

$$\rho \frac{\partial^2 u_z}{\partial t^2} = \frac{\partial \sigma_{zz}}{\partial z} \tag{22}$$

Where u_z is the displacement in the *z*-direction, ρ is the material density, and σ_{zz} is the normal stress in the *z*-direction. The stress-strain relation is,

$$\begin{aligned} \sigma_{zz} &= (\lambda + 2\mu)\varepsilon_{zz} - (3\lambda + 2\mu)\alpha'(T_l - T_0) \\ \sigma_{xx} &= \sigma_{yy} = \lambda\varepsilon_{zz} - (3\lambda + 2\mu)\alpha'(T_l - T_0) \end{aligned} \tag{23}$$

Where T_0 is the reference temperature as 300K and ε_{zz} denotes the non-zero normal strain in the *z*-direction with all other strains being zeros,

$$\varepsilon_{xx} = \varepsilon_{yy} = \varepsilon_{xz} = \varepsilon_{xy} = \varepsilon_{yz} = 0 \tag{24}$$

The temporal rate of the lattice dilation $\dot{\varepsilon}_{kk}$ is therefore $\dot{\varepsilon}_{kk} = \dot{\varepsilon}_{zz}$ and the strain-displacement relation in the normal z-direction is $\varepsilon_{zz} = \frac{\partial u_z}{\partial z}$.

Eqs. (17), (18), (21), (16), and (22)-(24) are the field equations dictating the thermo-elasto-dynamical response of both the single- and poly-crystalline metallic films to ultrafast irradiation. Of these equations, Eqs. (17), (18), (21) and (16) define electron dynamics as one that admits hyperbolic energy transport. Laser absorption mechanism and temperature-dependent heat capacity are considered to better understand the electron dynamics during non-equilibrium. Two significant properties, namely, electron thermal conductivity and electron-phonon coupling factor, are defined to incorporate the scatterings from film surface and grain boundary – a prevalent size effect that becomes non-negligible when the film thickness is comparable to the electron mean-free-path. Eqs. (22)-(24) govern the coupled thermal-mechanical field response in the thin film material. $G\left(T_e - T_l\right)$, the source term dictating energy diffusion to lattice in Eq. (21), becomes negligible when thermal equilibrium is reached at $T_e = T_l$. As such, Eqs. (22)-(24) along with the modified Eq. (21) govern the subsequent physical process in the state of post-equilibrium.

2.3.5. Initial and Boundary Conditions

The field equations are time-integrated using a finite difference scheme. Except for determining the electron temperature T_e at the two exposed boundaries at z=0 and z=L when an implicit method is followed, all numerical time integrations are performed with an explicit algorithm. Single- and poly-crystalline gold films of L=1000Å in thickness are studied whose optical, thermal, and mechanical properties are tabulated in Table 1. A laser beam of 630nm in wavelength, t_p=100fs in pulse duration, and ϕ=13.4J/m^2 in fluence is considered as the heating source. It is noted that the optical parameters follow

from [28] in which an ultrashort pulse heating experiment is reported. The ambient temperature T_0 is set to be 300K. The initial conditions defined for the electron and lattice temperatures are,

$$\begin{cases} T_e(z,0) = T_l(z,0) = T_0 \\ \sigma_{zz}(z,0) = \sigma_{xx}(z,0) = \sigma_{yy}(z,0) = 0 \\ u_z(z,0) = \dot{u}_z(z,0) = 0 \end{cases} \tag{25}$$

For simplicity, the following thermal-insulation boundary conditions are assigned by neglecting the heat loss from the front and back surfaces during ultrashort laser pulsing [26],

$$\begin{cases} q_e(0,t) = q_l(0,t) = 0 \\ q_e(L,t) = q_l(L,t) = 0 \\ \sigma_{zz}(0,t) = 0 \\ u_z(L,t) = 0 \end{cases} \tag{26}$$

Where the front surface at z=0 is assumed to be traction-free while the back surface at z=L is constrained. 50 grid points in the film thickness direction are used along with a 0.1fs integration time step for resolving the pre-thermal equilibrium state. The particular mesh size and integration time steps are the results of a comprehensive convergence study performed to ensure solution stability. A time step of 5fs is followed to time-integrate the ultrafast heating dynamics of the single- and poly-crystalline gold films when thermal equilibrium is reached.

2.4. Modelling Results

Table 1. Optical, thermal, and mechanical properties of gold material

Parameter	Value
τ_e	0.04 [ps] [15]
τ_l	0.8 [ps] [15]
E	74.9 [GPa] [38]
ν	0.42 [38]
α'	14.2×10^{-6} [K^{-1}] [38]
R	0.93 [26]
δ_s	15.3 [nm] [26]
C_{eo}	70 [$J/(m^3K^2)$] [38]
C_l	2.5×10^{6} [$J/(m^3K)$] [15]
κ_l	315 [$W/(m \cdot K)$] [15]
n	5.9×10^{28} [m^{-3}] [4]
k_B	1.38×10^{-23} [J/K] [15]
T_F	6.42×10^{4} [K] [15]
Λ_b	400 [Å] [4]
P	0 [4]
R_f	0.17 [4]
η	0.16 [15]
m	9.10938×10^{-31} [kg] [4]
υ_F	1.39×10^{6} [m/s] [4]
T_D	165 [K] [4]
E_F	8.82×10^{-19} [J] [4]
ρ	1.93×10^{4} [kg/m^3] [38]

2.4.1. Model Verification: Normalized Change of Electron Temperature

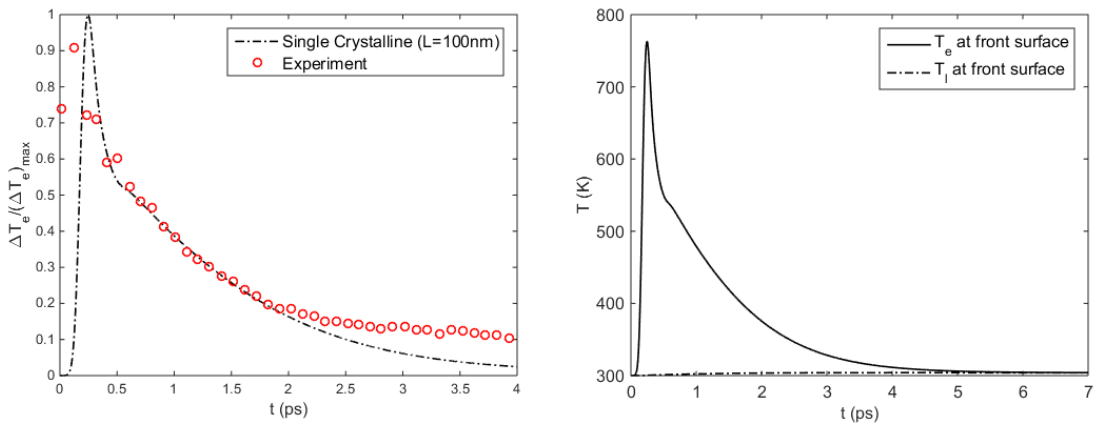

(a) **(b)**

Figure 4. Temperature time profiles

(a) Comparison of normalized electron temperature change (b) Electron and lattice temperatures

For verification purpose, the normalized change of the electron temperature in a single crystalline gold film of 100nm in thickness is considered against the experimental result reported in [28] where a 100fs laser with a 13.4J/m^2 in fluence was employed.

Figure 4(a) shows that the theoretical electron temperature profile at the front surface is in excellent agreement with the physical data, thus demonstrating the validity of the presented theoretical formulation in describing electron transport dynamics in the single crystalline film irradiated by a non-ablating ultrashort pulse. It is worthy to mention that though published in 1998, the experimental data in [28] by using reflectivity change with the transient thermoreflectance technology (TTR) remains being widely referenced

for model validation propose as found in Ref. [39] and [40] for its reliability and effectiveness in research of recent. To resolve the effects of grain size on scattering and carrier current flow, the film thickness needs be comparable to the electronic mean-free-path. While the time-domain thermoreflectance (TDTR) or frequency domain thermoreflectance techniques (FAFDTR) can be more advanced pump-probe techniques for ultrafast laser heating to take the measurement further and effectively reduce the error bound of the uncertainty or the inevitable noise in signal detecting. At smaller time, the disagreement is due to the instrumentation not being able to resolve the non-equilibrium state – the state of electron equilibrium. This is considered as noise in Ref. [28]. The slight deviation of the predicted line from the measured data is deem acceptable [15]. As noticed, the main difference between the simulation and the measured signal in Figure 4 is observed after 2.5ps, where the predicted line stays slightly below the measurement. The prediction of the model agrees well with the experimental data. Similar conclusions can also be found in Ref. [26] and [27]. As the experimental signals were acquired with certain error, the simulated line is believed to stay within the error bound. Since the standard deviation associated with the data is unknown, and that the deviation is not significant, the predicted line agrees well with the physical data. On the other hand, the experimental uncertainty or the noise in the photon detecting process can impact the detected reflectivity. After t=2.5ps, the reflectivity is relatively small and the number of photon-excited electrons are not large in number to render a higher signal-to-noise ratio. The noise level observed at t=4ps is much higher than the observed at t=1ps when an increase of photon-excited electron (caused by the noise) are expected. Considering all

the uncertainty, it is still appropriate that the simulation is valid throughout the entire time window considered.

The profile in the figure also indicates the mechanism of energy transport during non-equilibrium – a rapid elevation of electron temperature resulted from the radiation absorption, followed by a subsequent decline that corresponds to the thermal relaxations of the electron and lattice. Initially, a rapid photon-absorption excites electrons into a higher energy level and aggravates electron-electron collisions following a time scale that is characterized by the electron relaxation time. Electron temperature is seen to increase steeply within 0.5ps. The associated heat flux along the thickness direction then develops into a dominant source of energy dissipation, driving the electron temperature to drop while the corresponding lattice temperature stays relatively constant at 300K as indicated in Figure 4(b). The drop in the electron temperature is characterized by the hyperbolic nature of the electron heat flux. Energy is subsequently transferred to lattices and eventually diffuse further into the adjacent "cold" region via electron-phonon collision.

Electron temperature reaches a maximum value at approximately t=0.24ps, lagging behind the peak laser intensity registered at t = 0.2ps ($2t_p$). This characteristic delay in time is dictated by the electron relaxation time τ_e (~ 0.04ps for gold material). Lattice temperature stays increasing before it finally reaches the state of thermal equilibrium with electrons at t = 5.83ps. At the location impinged by the laser pulse, a maximum lattice temperature of 304.018K is observed at t = 4.402ps.

2.4.2. Size Effects on Thermal-Mechanical Fields

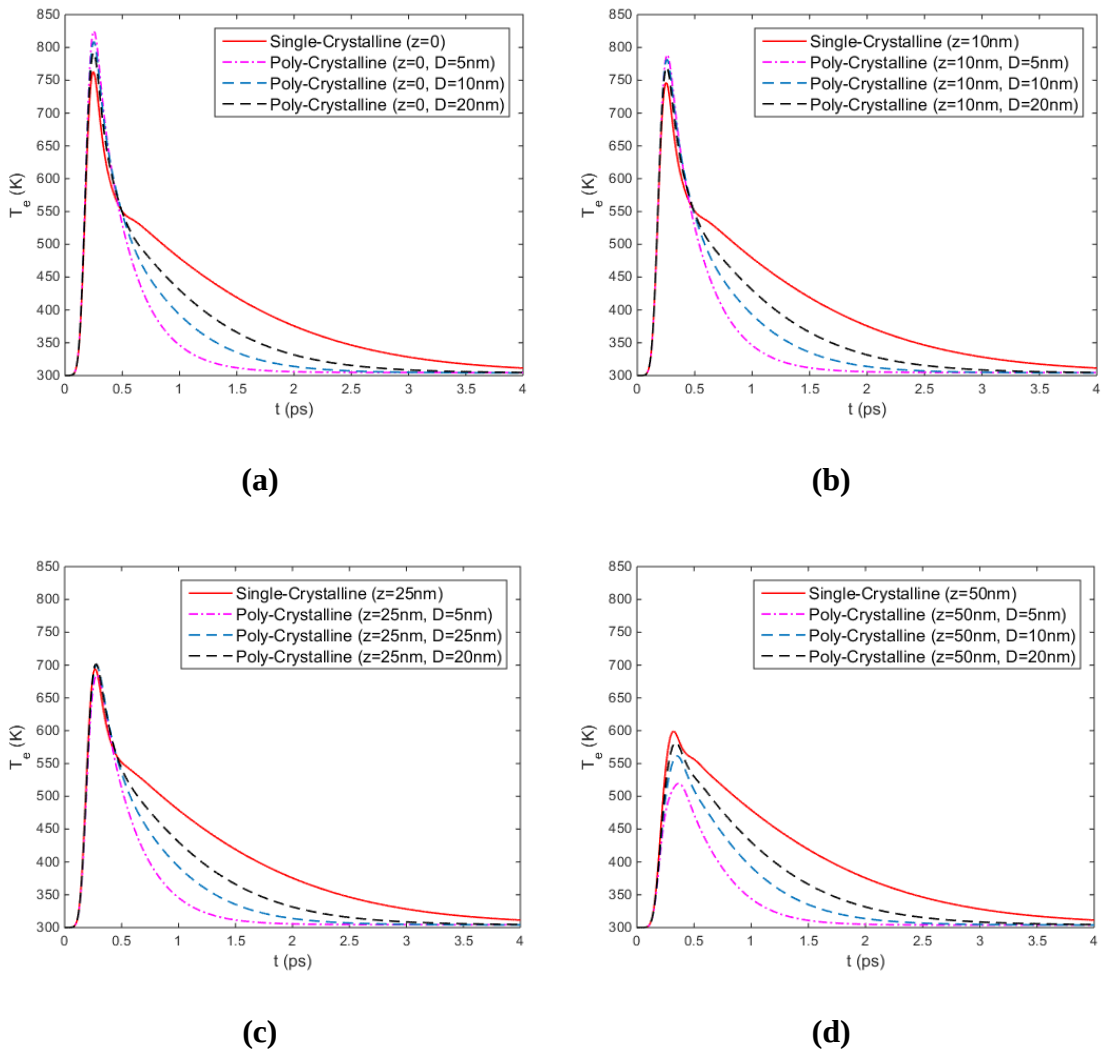

Figure 5. Size effect on electron temperature (T_e) evolution

(a) z=0; (b) z=10nm; (c) z=25nm; (d) z=50nm

Figure 5 compares the electron temperatures resolved in the single- and poly-crystalline target films. To investigate the size effect in the polycrystalline film, several

averaged grain sizes (D = 5nm, 10nm, and 20nm) are applied to a film of 100nm in thickness. Four different positions at z = 0nm, 10nm, 25nm, and 50nm are considered for their responses to the same optical input of a 100fs pulse with a 13.4J/m^2 in fluence.

It is evident from Figure 5 that, at all the locations considered and prior to reaching the peak temperature, electron temperatures in the polycrystalline film are identical to those of the single-crystalline film's. This is due to the fact that the underlying absorption mechanism is the same. However, significant deviations are observed at the peak temperature. At near-field on the front surface, the maximum electron temperature registered by the polycrystalline films of different D's are larger than the maximum temperature of the single crystalline counterpart. As indicated by Figure 5(a) and Figure 5 (b), electron energy is localized at the surface and diffuses within only a few tens of nanometers into the thickness direction of the polycrystalline films. In other words, less electron energy is transferred to the deeper region. This is primarily attributed to the fact that electron thermal conductivity is a strong function of the (grain) size effect and non-equilibrium heating. Recall that in Figure 2., $\kappa_{e,f}$, the property for describing heat conduction macroscopically, is seen to decrease in value in the polycrystalline film. As more electron energies are localized closed to the irradiated surface rather than being transferred into the deeper region, a higher maximum electron temperature is observed in the near field while lower temperature is registered at locations away from the surface and into the film thickness, as is indicated in Figure 5 (c) and Figure 5 (d). Another observation with the figure attributable to the same dynamics is that smaller the averaged grain diameter of the polycrystalline film, higher the maximum electron temperature.

Absorbed laser energy decreases sharply after the peak laser intensity is reached. Electron temperature is not seen to display noticeable variations up until about t = 0.4ps ($4t_p$). In Figure 5 (a), Figure 5 (b), and Figure 5 (c), an obvious deviation occurs at t=0.5ps for both the single- and poly-crystalline films. After that, the electron temperature of the single crystalline film decreases while others starting a precipitous decline. This results in a higher electron temperature in the single crystalline film afterward in time. The rates of decrease of the polycrystalline films with different averaged grain diameters are so distinct that they differentiate themselves from their single crystalline counterpart as being nano-structurally different. The electron temperature of the single crystalline film is seen to decrease with a rate that is significantly lower than the rest. This is due to the difference in electron-lattice energy exchange as characterized by the electron-phonon coupling factor. As electron temperature varies with grain size and declines with increasing number of grain boundaries, the energy diffusion through electrons would thereby decline accordingly. The enhanced electron temperature cooling rate predicted in the polycrystalline film also agrees with the measured result from a transient thermoreflectivity experiment reported in [35].

In Figure 6, unlike the lattice temperature of the single crystalline film, all temperature profiles of the polycrystalline films feature a steeper climb and reach a plateau faster. This is due to the larger electron-phonon coupling factor that is characteristic of the polycrystalline films. Recall that the G-factor of the polycrystalline film was larger than the corresponding G-factor of the single crystalline film when $\beta < 10$. Thus, a higher energy transport rate is realized in the electron subsystem and a shorter relaxation time is

afterwards followed to establish thermal equilibrium in the polycrystalline metallic films. As is evident from Figure 6(a) and Figure 6(b), additional scatterings impede the transport of the electron energy, thus having more number of excited electrons in near-field to give rise to a higher lattice temperature in the polycrystalline films. This perturbation to lattice structure is physically recognized as a rapid thermal expansion from which propagating stress waves of exceedingly high frequency content are generated [23], [36] and [37].

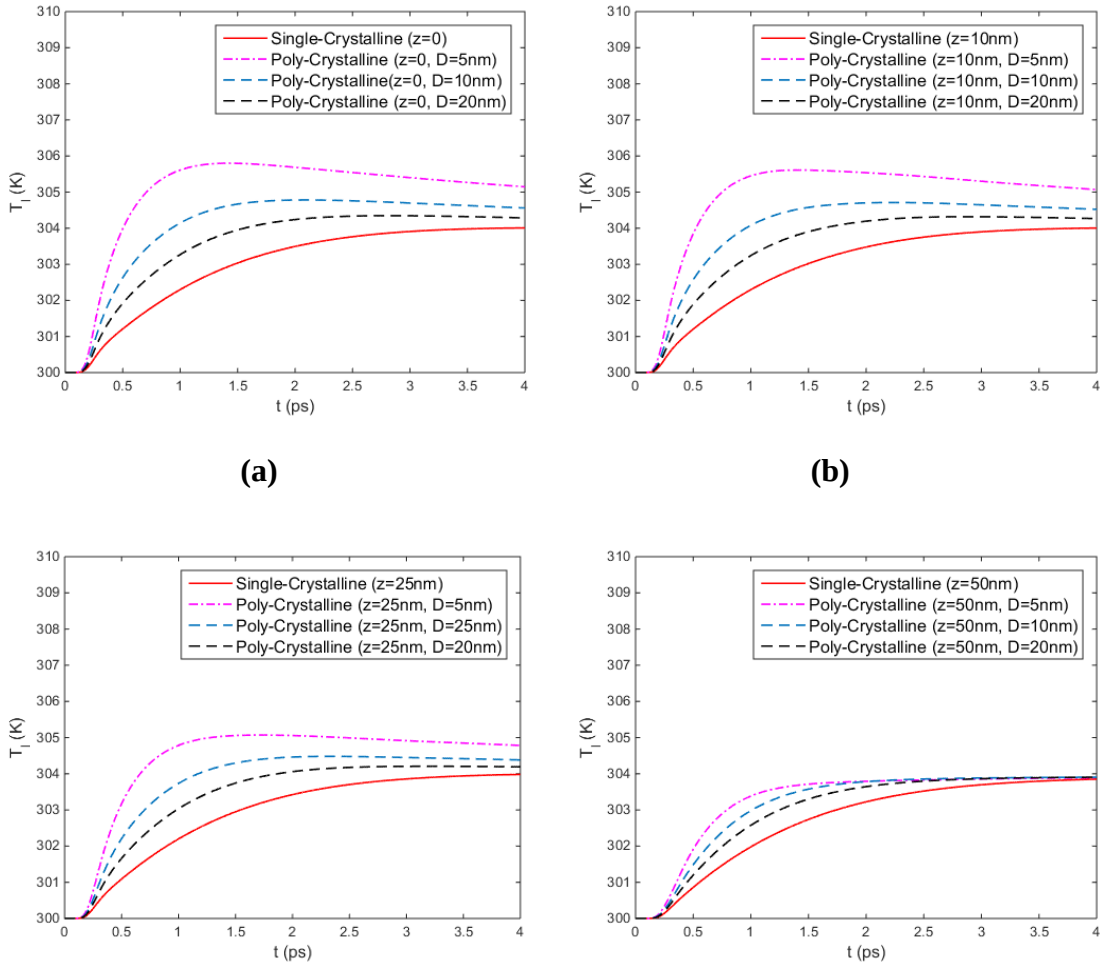

(a) **(b)**

(c) **(d)**

Figure 6. Size effect on lattice temperature (T_l) evolution

(a) z=0; (b) z=10nm; (c) z=25nm; (d) z=50nm

Another observation with regard to the size effect is that smaller averaged grain size is associated with a higher rate of lattice temperature increase and a shorter time of relaxation for reaching thermal equilibrium in the polycrystalline films. The thermalization time for the polycrystalline films in Figure 6 are 2.77ps, 3.26ps, and 4.29ps

with respect to D=5nm, 10nm, and 20nm, respectively, whereas the thermalization time for the single crystalline film is 5.83ps.

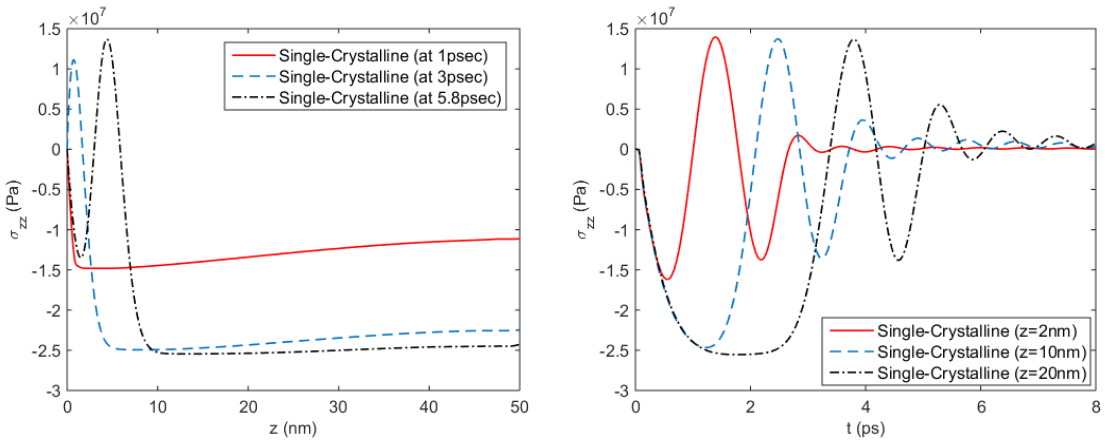

(a) **(b)**

Figure 7. σ_{zz} in single crystalline film

(a) t=1ps, 3ps and 5.8ps; (b) z=2nm, 10nm and 20nm

Figure 7 gives the spatial and temporal evolutions of the corresponding thermally induced normal stress σ_{zz} in the 100nm in thickness single crystalline film. Figure 7(a) shows the spatial variation of σ_{zz} at times t=1ps, 3ps, and 5.8ps when the thermal balance is reached. It is seen that the stress induced at the initial stage of time at t=1ps is compressive in the immediate vicinity of the irradiated surface. The initiation of the stress is attributed to the rapid contraction of the material undergoing non-equilibrium heating. As heating progresses to t=3ps, lattice temperatures escalate and the resulted thermal expansion paves the way for a tensile stress at the location that was in compression just a brief moment ago, as seen in Figure 7(a). Such a tension-compression stress alternation

becomes more prominent at t=5.8ps. It then propagates further into the film as a stress wave.

Figure 7(b) presents the temporal evolution of the induced thermal stress acquired at 3 different locations at z=2nm, 10nm, and 20nm. Within the 20ps time window, all σ_{zz} exhibit definitive features characteristic of a full-fledged propagating wave that is also unmistakably dispersive. The maximum magnitude of the tensile stress is 1.396×10^7 Pa at z = 2nm, 1.374×10^7 Pa at z = 10nm, and 1.369×10^7 Pa at z = 20nm. The field of negative temperature gradient the wave encounters as it propagates further into the material contributes to the decrease in stress magnitude. Moreover, the maximum tensile stress is at least one order-of-magnitude lower than the yield stress of the gold material, thus being evident of only elastic deformation is involved. It is noted that these waves, though of relatively low stress in magnitude, are also of very high frequency and high power density [36] and [37]. They can be detrimental to the host material causing micro-cracking and physical damage if not properly mitigated.

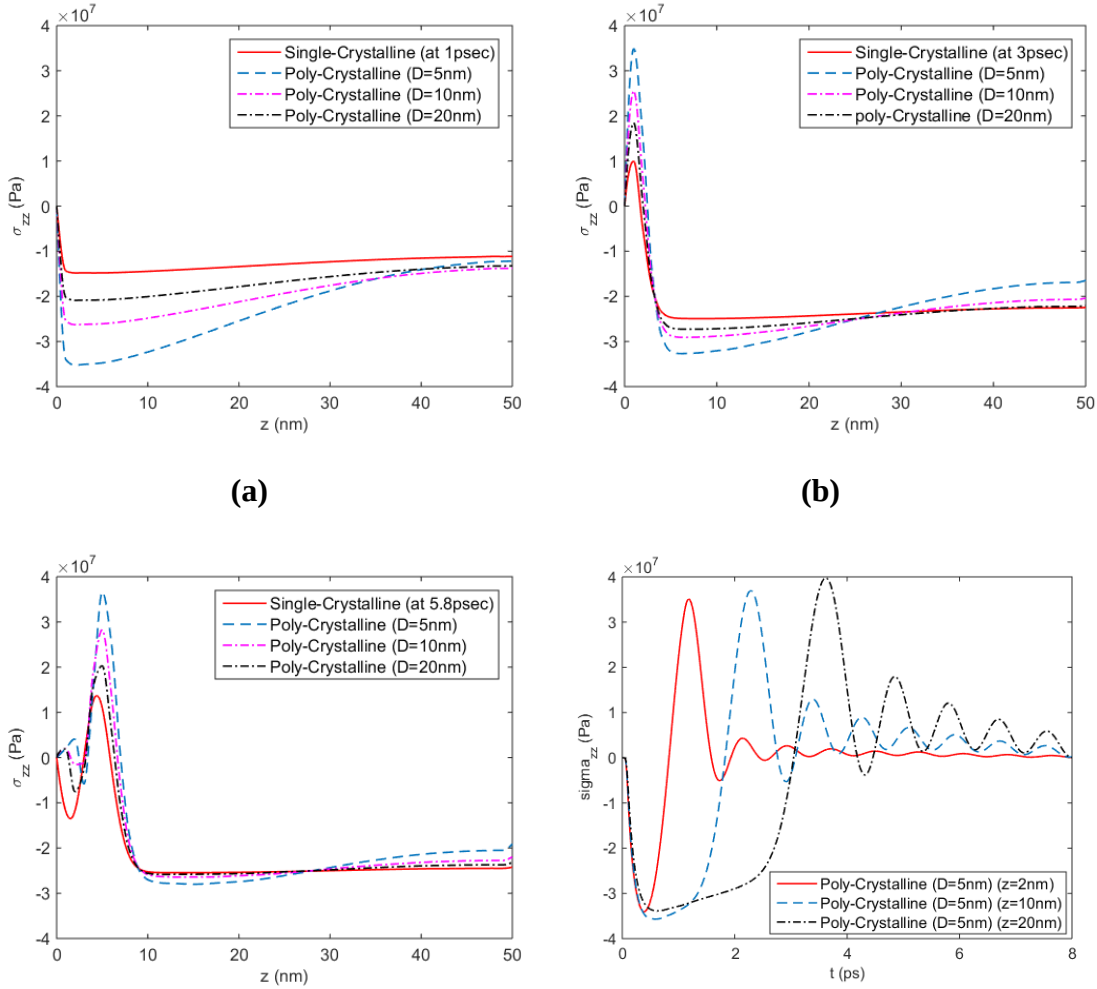

Figure 8. σ_{zz} in single- and poly-crystalline films

(a) t=1ps; (b) t=3ps; (c) t=5.8ps; (d) D=5nm; (e) D=10nm; (f) D=20nm

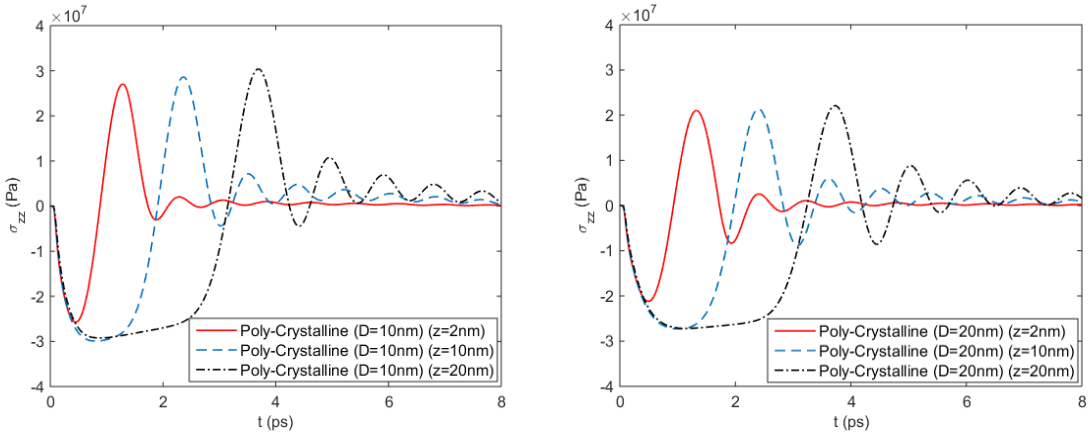

(e) **(f)**

Figure 8. Continued

Figure 8 provides the spatial and temporal evolutions of the normal stress σ_{zz} obtained for the single- and poly-crystalline films. Size effects on the mechanical responses of the materials are also studied by considering the initiation of σ_{zz} in films of D=5nm, 10nm, and 20nm. Figure 8(a)-(c) present the time histories of σ_{zz} and Figure 8(d)-(f) show the stress responses at z=2nm, 10nm, and 20nm in time. Albeit different in magnitude, the stress profiles of the polycrystalline films seen in Figure 8(a)-(c) all demonstrate similar features of compression and tension as that of the single crystalline film's. The magnitudes of the compressive and tensile stresses acquired at locations beneath the irradiated surface increase markedly with decreasing D, the averaged grain diameter. Variations in the lattice temperature induce the thermal expansion that gives rise to the propagating stress wave. The distinction in the stress profiles corresponds well with the corresponding difference in the lattice temperature which is size-effect dependent.

As heating progresses, the distinction in stress profiles for the single- and poly-crystalline films slowly diminishes. Moreover, in regions deeper than 50nm, the magnitude of the compressive stress tends to be smaller in polycrystalline films having more grain boundaries. This is implicitly caused by the grain-boundary scattering since more electron energy is confined in the vicinity of the irradiated surface, thus less energy is transferred farther into the film to result in lower lattice temperature and diminishing stress magnitude.

Figure 8(d)-(f) illustrate that for the polycrystalline film having an averaged grain diameter D=5nm, the corresponding peak tensile stresses are 3.506×10^7 Pa at z=2nm, 3.695×10^7 Pa at z=10nm, and 3.976×10^7 Pa at z=20nm. For D=10nm the values are 2.703×10^7 Pa at z=2nm, 2.861×10^7 P at z=10nm, and 3.038×10^7 Pa at z=20nm. For D=20nm, the maximum stresses are 2.103×10^7 Pa at z=2nm, 2.138×10^7 Pa at z=10nm, and 2.211×10^7 Pa at z=20nm. All these results are a marked feature particular of the polycrystalline metallic film in which the peak tensile stress is seen to increase with decreasing D's.

The observations and comparisons made with the temporal and spatial evolutions of the normal stresses suggest that the laser induced dynamic state of stress is more rigorous in polycrystalline films, thus providing a greater probability for dislocation gliding and grain boundary sliding. Even with a fluence that is below the damage threshold, ultrafast heating could potentially generate high frequency shear stresses that would in turn set off dislocation gliding and inelastic deformation. It is therefore essential

to understanding how polycrystalline materials respond to ultrafast heating in the presence of size effect and grain boundary scattering.

2.5. Summary

The fundamental mechanism underlying laser-material interaction in polycrystalline metallic thin films irradiated by an ultrafast laser of low laser fluence was explored. A generalized formulation viable for describing the non-melting, thermo-elastodynamical responses in both single- and poly-crystalline metallic thin films was presented. This section primarily aimed to investigate the correlated thermophysical properties that govern both electron and lattice energy transport in polycrystalline metallic films and the grain size effects, including film thickness and averaged grain diameter, on the corresponding thermal-mechanical fields. The one-dimensional thermo-elasto-dynamic model was established and numerically resolved to meet the requirement. Normalized electron temperatures calculated using the formulation for a single-crystalline gold film were favorably examined against published physical data and thus verify the validation of model. Grain size effects were found to be of significance on

Thermal conductivity: As grain boundary scattering hinders electron thermal conduction and thermal diffusion, the decrease in electron thermal conductivity is prominent when the averaged grain diameter is small.

Electron-phonon coupling factor: A decrease in grain size is accompanied by an increase in the corresponding e-ph coupling factor, indicating that energy is transferred from electrons to lattices at a faster rate.

Thermal-mechanical field response: The responses in the thermal and mechanical fields of the polycrystalline films differentiate themselves from their single crystalline counterparts as being nano-structurally distinct. In addition, lattice temperature and the dynamic state of the near-field stress were intense in the polycrystalline films, thus signifying the likelihood for dislocation gliding and sliding along grain boundaries.

As seen in Figure 4 (a), at a low laser fluence, the normalized electron temperature profile was comparable to the physical data obtained using transient thermoreflectivity [28]. A comprehensive literature search suggests that electron energy induced thermal responses have been given the most attentions while lattice temperature and lattice thermal-mechanical coupling were comparatively less studied. Thermal-mechanical coupling and thermally induced mechanical response need be considered as the lattice temperatures in single- and polycrystalline films are so definitively different that they have profound implications for the proper understanding of thermoelastic deformation, generation of heat-affected-zone, and stress wave propagation, to name only three.

2.6. References

[1] Guo, Z., and Hunter, B., "Advances in ultrafast radiative transfer modeling and applications: A review," *Heat Transfer Research*, Vol. 44, No. 3-4, 2013, pp. 303-304.

[2] Pecholt, B., Vendan, M., Dong, Y., and Molian, P., "Ultrafast Laser Micromachining of 3C-SiC Thin Films for MEMS Device Fabrication," *The International Journal of Advanced Manufacturing Technology*, Vol. 39 No. 3-4, 2008, pp. 239-250.

[3] Yasseen, A. A., Zorman, C. A., and Mehregany, M., "Surface Micromachining of Polycrystalline SiC Films Using Microfabricated Molds of SiO/sub 2/and Polysilicon," *Journal of Microelectromechanical Systems*, Vol. 8, No. 3, 1999, pp. 237-242.

[4] Qiu, T. Q., and Tien, C. L., "Size Effects on Nonequilibrium Laser Heating of Metal Films," *ASME Transactions Journal of Heat Transfer*, Vol. 115, No. 4, 1993, pp. 842-847.

[5] Fan, L-S., Tai, Y.-C., and Muller, R. S., "Integrated Movable Micromechanical Structures for Sensors and Actuators," *IEEE Transactions on Electron Devices*, Vol. 35, No. 6, 1988, pp. 724-730.

[6] Elsayed-Ali, H. E., Juhasz, T., Smith, G. O., and Bron, W. E., "Femtosecond Thermoreflectivity and Thermotransmissivity of Polycrystalline and Single-Crystalline Gold Films," *Physical Review B*, Vol. 43, No. 5, 1991, pp. 4488-4491.

[7] Hostetler, J. L., Smith, A. N., Czajkowsky, D. M., and Norris, P. M., "Measurement of the Electron-Phonon Coupling Factor Dependence on Film Thickness and Grain Size in Au, Cr, and Al," *Applied Optics*, Vol. 38, No. 16, 1999, pp. 3614-3620.

[8] Hopkins, P. E., and Norris, P. M., "Substrate Influence in Electron–Phonon Coupling Measurements in Thin Au Films," *Applied Surface Science*, Vol. 253, No. 15, 2007, pp. 6289-6294.

[9] Rabroker, G. A., Suh, C. S., and Chona, R., "Laser-induced stress wave thermometry applied to silicon wafer processing: Modeling and experimentation," *Experimental mechanics*, Vol. 45, No. 1, 2005, pp. 3-8.

[10] Anisimov, S. I., Kapeliovich, B. L. and Perel'man, T. L., "Electron emission from the metal surfaces induced by ultrashort lasers pulses," *Zhurnal Ehksperimental'noj i Teoreticheskoj Fiziki*, 66(2), pp. 776-781, (1974).

[11] Qiu, T. Q., and Tien, C. L., "Heat Transfer Mechanisms During Short-Pulse Laser Heating of Metals," *ASME Transactions Journal of Heat Transfer*, Vol. 115, No. 4, 1993, pp. 835-841.

[12] Van Driel, H. M., "Kinetics of high-density plasmas generated in Si by 1.06-and 0.53-μm picosecond laser pulses," *Physical Review B*, 35(15), pp. 8166-8176, (1987).

[13] Daraszewicz, S. L. and Duffy, D. M., "Extending the inelastic thermal spike model for semiconductors and insulators," *Nuclear Instruments and Methods in Physics Research Section B: Beam Interactions with Materials and Atoms*, 269(14), pp. 1646-1649, (2011).

[14] Rämer, A., Osmani, O. and Rethfeld, B., "Laser damage in silicon: Energy absorption, relaxation, and transport," *Journal of Applied Physics*, 116(5), pp. 053508-1 - 053508-12, (2014).

[15] Chen, J. K., and Beraun, J. E., "Numerical Study of Ultrashort Laser Pulse Interactions with Metal Films," *Numerical Heat Transfer: Part A: Applications*, Vol. 40, No. 1, 2001, pp. 1-20.

[16] Singha, S., Hu, Z., and Gordon, R. J. "Ablation and plasma emission produced by dual femtosecond laser pulses," *Journal of Applied Physics*, 104(11), pp. 113520-1 - 113520-10, (2008).

[17] Suh, C. S., and Burger, C. P., "Effects of Thermomechanical Coupling and Relaxation Times on Wave Spectrum in Dynamic Theory of Generalized Thermoelasticity," *ASME Transactions Journal of Applied Mechanics*, Vol. 65, No. 3, 1998, pp. 605-613.

[18] Qi, X., and Suh, C. S., "Ultrafast Laser-Induced Elastodynamics in Single Crystalline Silicon Part I: Model Formulation," *Journal of Thermal Stresses*, Vol. 32, No. 5, 2009, pp. 477-493.

[19] Qi, X., and Suh, C. S., "Elasto-Viscoplastic Response of Silicon to Femtosecond Laser Heating at Elevated Temperature," *Journal of Thermal Stresses*, Vol. 34, No. 2, 2011, pp. 115-137.

[20] Qi, X., Liu, L., and Suh, C. S., "Elasto-Viscoplastic Wave Thermometry for Single Crystalline Silicon Processing," *International Journal of Applied Mechanics*, Vol. 2 No. 4, 2010, pp. 827-849.

[21] Vedantham, V., Suh, C. S., and Chona, R., "Laser Induced Stress Wave Thermometry for In-situ Temperature and Thickness Characterization of Single Crystalline Silicon Wafer: Part I—Theory and Apparatus," *Experimental Mechanics*, Vol. 51, No. 7, 2011, pp. 1103-1114.

[22] Vedantham, V., Suh, C. S., and Chona, R., "Laser Induced Stress Wave Thermometry for In-Situ Temperature and Thickness Characterization of Single Crystalline Silicon Wafer: Part II—Experimental Results," *Experimental Mechanics*, Vol. 51, No. 7, 2011, pp. 1115-1122.

[23] Qi, X., and Suh, C. S., "Ultrafast Laser-Induced Elastodynamics in Single Crystalline Silicon Part II: Near-Field Response," *Journal of Thermal Stresses*, Vol. 32, No. 5, 2009, pp. 494-511.

[24] Wellershoff, S. -S., Hohlfeld, J., Güdde, J., and Matthias, E., "The Role of Electron–Phonon Coupling in Femtosecond Laser Damage of Metals." *Applied Physics A*, Vol. 69, Suppl. 1, 1999, pp. S99-S107.

[25] Hohlfeld, J., Wellershoff, S. -S., Güdde, J., Conrad, U., Jähnake, V., and Matthias, E., "Electron and Lattice Dynamics Following Optical Excitation of Metals," *Chemical Physics*, Vol. 251, No. 1, 2000, pp. 237-258.

[26] Qiu, T. Q., and Tien, C. L., "Femtosecond Laser Heating of Multi-Layer Metals—I. Analysis," *International Journal of Heat and Mass Transfer*, Vol. 37, No. 17, 1994, pp. 2789-2797.

[27] Qiu, T. Q., and Tien, C. L., "Short-pulse Laser Heating on Metals," *International Journal of Heat and Mass Transfer*, Vol. 35, No. 3, 1992, pp. 719-726.

[28] Qiu, T. Q., Juhasz, T., Suarez, C., Bron, W. E., and Tien, C. L., "Femtosecond laser heating of multi-layer metals—II. Experiments," *International Journal of Heat and Mass Transfer*, Vol. 37, No. 17, 1994, pp. 2799-2808.

[29] Jiang, L., and Tsai, H. L., "Improved Two-Temperature Model and Its Application in Ultrashort Laser Heating of Metal Films," *ASME Transactions Journal of Heat Transfer*, Vol. 127, No. 10, 2005, pp. 1167-1173.

[30] Durkan, C., and Welland, M. E., “Size Effects in the Electrical Resistivity of Polycrystalline Nanowires,” *Physical Review B*, Vol. 61. No. 20, 2000, pp. 14215-14218.

[31] Mayadas, A. F., and Shatzkes, M., “Electrical-Resistivity Model for Polycrystalline Films: The Case of Arbitrary Reflection at External Surfaces,” *Physical Review B*, Vol. 1, No. 4, 1970, pp. 1382-1389.

[32] Bulgakova, N. M., Stoian, R., Rosenfeld, A., Hertel, I. V., and Campbell, E. E. B., “Electronic Transport and Consequences for Material Removal in Ultrafast Pulsed Laser Ablation of Materials,” *Physical Review B*, Vol. 69, No. 5, 2004, 054102.

[33] Anisimov, S. I., and Rethfeld, B., “Theory of Ultrashort Laser Pulse Interaction with A Metal,” *SPIE Proceedings 3093, Nonresonant Laser-Matter Interaction (NLMI-9)*, 4 April 1997.

[34] Fann, W. S., Storz, R., Tom, H. W. K., and Bokor, J., “Direct Measurement of Nonequilibrium Electron-Energy Distributions in Subpicosecond Laser-Heated Gold Films,” *Physical Review Letters*, Vol. 68, No. 18, 1992, pp. 2834-2837.

[35] Juhasz, T., Elsayed-Ali, H. E., Smith, G. O., Suárez, C., and Bron, W. E., “Direct Measurements of The Transport of Nonequilibrium Electrons in Gold Films with Different Crystal Structures," *Physical Review B*, Vol. 48, No. 20, 1993, pp. 15488-15491.

[36] Qi, X., and Suh, C. S., “Generalized Thermo-Elastodynamics for Semiconductor Material Subject to Ultrafast Laser Heating. Part I: Model Description and

Validation," *International Journal of Heat and Mass Transfer*, Vol. 53, No. 1, 2010, pp. 41-47.

[37] Qi, X., and Suh, C. S., "Generalized Thermo-Elastodynamics for Semiconductor Material Subject to Ultrafast Laser Heating. Part II: Near-Field Response and Damage Evaluation," *International Journal of Heat and Mass Transfer* Vol. 53, No. 4, 2010, pp. 744-752.

[38] Chen, J. K., Beraun, J. E. and Tham, C. L., "Ultrafast thermoelasticity for short-pulse laser heating," *International Journal of Engineering Science* Vol. 42, No. 8-9, 2004, pp. 793-807.

[39] Pattamatta, A., and Madnia, C. K., "Modeling electron-phonon nonequilibrium in gold films using Boltzmann transport model," *Journal of Heat Transfer*, Vol. 131, No. 8, 2009, pp. 082401.

[40] Wang, H-D., Ma, W., Zhang, X., Wang, W., and Guo, Z.-Y., "Theoretical and experimental study on the heat transport in metallic nanofilms heated by ultra-short pulsed laser," *International Journal of Heat and Mass Transfer*, Vol. 54, No. 4, 2011, pp. 967-974.

[41] Malen, J. A., Baheti, K., Tong, T., Zhao, Y., Hudgings, J. A., and Majumdar, A., "Optical measurement of thermal conductivity using fiber aligned frequency domain thermoreflectance," *Journal of Heat Transfer*, Vol. 133, No. 8, 2011, pp. 081601.

3. THERMO-ELASTO-DYNAMICS OF POLYCRYSTALLINE GOLD FILMS – THERMAL-MECHANICAL MODELLING

3.1. Introduction

It was shown that lattice temperatures induced by below-damage-threshold laser fluence were far lower than the melting temperature of the gold material and that thermally generated stress waves propagated with a maximum amplitude at least one order-of-magnitude lower than gold's yield stress or ultimate tensile strength. Femtosecond lasers with fluence below damage threshold have been exploited in many engineering applications such as nondestructive evaluation (NDE). Thermo-elastically generated laser acoustic waves are applicable to identifying surface cracks and material flaws. Laser ultrasounds are also found to be viable for measuring residual stresses and for profiling temperature by exploring the dispersion that is characteristic of optically initiated propagating waves or the investigation for the elimination of crack formation and elongation in Refs. [1] and [5]. Ultrafast laser heating and the propagation of high frequency thermo-elastic waves are a complex dynamic process involving laser energy absorption, thermal diffusion, electron-phonon energy transport and thermal-mechanical coupling. However, lacking a comprehensive understanding of the underlying physical mechanism that governs the process inevitably impedes the broader application of ultrashort optics to polycrystalline metallic materials. This is particularly true with applications involving ultrafast laser ablation.

It was experimentally observed that the localized thermal stress and its propagating wave have significant effect on the formation of dislocations and cracks. Even though no crack is formed, the target was still be observed to expand by the tensile stress and return back to the origin after a while. Such phenomena is more prominent in the single crystal target due to the anisotropic propagation leading to the stress concentration in certain directions, and thus forms the cracks. Another extended research area is the modulation of transient laser-induced thermo-elastic stress distribution for controlling crack formation or eliminating the elongation at the crack tip. By modulating the multiple spots of ultrafast laser pulses and resulting in the ideal transient stress distribution, the crack elongation at the crack tip is able to be reduced or even eliminated [2].

As metallic thin films are widely utilized in micro-electromechancial systems and semiconductors as interconnects, employing ultrashort laser heating to the removal of material in polycrystalline metallic nanofilms in Ref. [3] and [4] raises the concern over whether such high frequency disturbances would inflict physical damages that impact fabrication quality.

Although numerous studies have observed the generation and propagation of the thermo-elastic stress waves being caused by the relaxation of laser-induced thermal energy localized near the irradiated surface by the ultrafast laser heating with low fluence, publications and theoretical investigations on the ultrafast laser-induced thermo-mechanical coupling or the significant characteristics of the induced stress wave propagation are rare. Moreover, the correlation between the ultrafast laser input parameters, specific material properties, and the finally generated thermo-elastic waves

on different categories of material targets is still not fully understood and elusive. This demands the study on mechanism on the entire process of the thermo-elasto-dynamics involving by the ultrafast laser heating and the detailed investigation for the formed thermo-elastic stress waves and its propagation both temporally and spatially. Otherwise, the unexpected micro- or macro- cracking potentially impedes the stability and reduces the micromachining resolution of the use of non-destructive evaluation, or the methodology is ineffective and greatly restricted by the determination of the monotonous patterning on various categories of materials with plenty of trials and errors.

Albeit generating no plasma or thermally induced damage, however, ultrafast lasers of low fluence can initiate thermo-elastodynamical disturbances of extremely high propagation frequency. The negative impact of the high-frequency propagating stress waves generated with non-melting fluence was also indicated in [6]. Coupled thermal-mechanical disturbance must therefore be incorporated into the governing field equations to ensure that the total energy is properly balanced obeying the principle of energy conservation. In light of the arguments made in Refs. [5] – [9], it would be insufficient to attempt to characterize ultrafast thermo-elastodynamics using models of low dimensionality where lateral distributions of laser energy absorption and heat diffusion along with the resulted stress waves cannot be properly described. Therefore, to better develop the model of thermo-elasto-dynamics induced by the ultrafast laser heating and analyze the finally generated elastic stress waves and the corresponding feature of wave propagation inside the target, a three-dimensional model is demanded, rather than the one-dimensional model proposed in the previous section.

Consequently, in the present section, an axisymmetric model is developed and implemented following a staggered-grid numerical scheme for the investigation of the ultrashort heating induced thermoelasticity in polycrystalline metallic films. The hyperbolic two-step temperature model provides the basis for obtaining the near-field, thermal-mechanical responses within the picoseconds regime. The grain size effects attributable to film surface and grain boundary scatterings are also necessary to be considered for determining the dominant thermophysical properties for the energy transport and the ultimate impact they bring about on temperature and stress distributions. The staggered-grid finite different scheme reported in Ref. [11] is adopted and further modified for time-integrating the coupled thermal-mechanical field variables. Numerical results are then provided and compared with reported physical data for validating the model formulation. A parametric study is performed in the following sections incorporating different averaged grain diameters and grain boundaries to study the laser-induced thermal-mechanical response in the proposed three-dimensional model. More computational results along with an elaborated discussion of the thermo-mechanical response, a methodology for analyzing the features of wave propagation and the associated mechanism for initiating micro-cracking are presented in the next section of the paper.

3.2. Energy Balance Equations and Constitutive Equations

3.2.1. Axisymmetric Model

One-dimensional model considering responses only in the thickness direction is commonly applied to describe the thermal effect in films irradiated by ultrafast laser. Electron temperature would be over-estimated as the lateral effects of both the beam

profile and thermal diffusion cannot be accounted for using uniaxial models [5] and [11], impacting the proper description of the lattice temperature and corresponding coupled thermal-mechanical response as results. When laser fluence is high, 1D models are insufficient to fully comprehend the thermally induced shear stress field that is essential for initiating plastic deformation (through slip and slide) in polycrystalline nanostructures. To model ultrafast heating thermo-elastodyamics, both the lateral and thickness directions are considered using an axisymmetric model that allows for the spatial profile of the beam be incorporated and the thermal-mechanical interaction in both the radial and thickness directions be resolved. The model is feasible for resolving ultrashort heating responses in polycrystalline metallic materials because such materials are macroscopically homogeneous and isotropic along the radial and transverse (thickness) directions.

The polycrystalline metallic films considered in the sections that follow are of a 1μm (in thickness) by 4μm (in radius) configuration. Irradiated by an ultrashort laser pulse, the microscale section defines the problem domain in which the induced thermo-elastodynamic responses are studied as functions of electron heat capacity, surface and grain boundary scatterings, and film thickness.

3.2.2. Laser Intensity Source Term

Eq. (27) defines the temporal and spatial profile of the ultrashort laser pulse in the cylindrical coordinates to be employed as the heat source. The volumetric intensity of the laser beam which follows a Gaussian distribution attenuates exponentially with increasing depth (z-axis) and radius (r-axis)

$$S(z,r,t)=\sqrt{\frac{4\ln(2)}{\pi}}\cdot\frac{1-R}{t_p(\delta_s+\delta_b)\left[1-\mathrm{e}^{-L/(\delta_s+\delta_b)}\right]}$$
$$\cdot\phi\cdot\exp\left[-\left(\frac{r}{r_s}\right)^2-\left(\frac{z}{\delta_s+\delta_b}\right)-4\ln(2)\left(\frac{t-2t_p}{t_p}\right)^2\right] \tag{27}$$

Where ϕ is the fluence of the laser pulse at $r=0$, t_p is the laser pulse duration, $r_s=1\mu\mathrm{m}$ is the spot size of the Gaussian beam, L is the thickness, R is the reflectivity, δ_s is the optical penetration depth and δ_b is the ballistic range by taking into account the ballistic motion as in [7].

3.2.3. Electron Energy Balance Equation

As stated in the previous one-dimensional mode, the thermo-elasto-dynamic model formulated features the energy transport dynamics in both electron and lattice subsystem that delineate the finite and hyperbolic nature of the heat flux. Moreover, the energy dissipated to initiate mechanical field response is incorporated into the energy transport equations to establish the coupled thermo-elasticity in polycrystalline metallic films. The generalized energy transport equations of electrons in the vector-form is followed as,

$$C_e(\mathbf{T_e})\frac{\partial\mathbf{T_e}}{\partial t}=-\nabla\cdot\mathbf{q_e}-G(\mathbf{T_e}-\mathbf{T_l})+\mathbf{S}$$
$$\tau_e\frac{\partial\mathbf{q_e}}{\partial t}+\mathbf{q_e}=-\kappa_e\nabla\mathbf{T_e} \tag{28}$$

Where the vector $\mathbf{T_e}$ and $\mathbf{T_l}$ represent the electron and lattice temperature field, $\mathbf{q_e}$ is the electron heat flux vectors, and $\mathbf{S}$ is the laser energy source calculated by using Eq. (27). Properties κ_e represents the electron thermal conductivity with respect to the

field vector $\mathbf{T_e}$, C_e is the electron heat capacity, and G is the electron-phonon coupling factor. τ_e in Eq. (28), the hyperbolic heat flux equation, is the relaxation time of free electrons.

3.2.4. Lattice Energy Balance Equation

$$C_l\left(\mathbf{T_l}\right)\frac{\partial \mathbf{T_l}}{\partial t} = -\nabla\cdot\mathbf{q_l} + G\left(\mathbf{T_e}-\mathbf{T}_l\right) - \left(3\lambda+2\mu\right)\alpha'\mathbf{T}_l\dot{\boldsymbol{\varepsilon}}_{\mathbf{kk}}$$
$$\tau_l\frac{\partial \mathbf{q_l}}{\partial t} + \mathbf{q_l} = -\kappa_l\nabla\mathbf{T_l} \tag{29}$$

Where $\mathbf{q_l}$ represents the lattice heat flux vector, and the energy term in the lattice energy balance equation, $\mathbf{L_M} = \left(3\lambda+2\mu\right)\alpha'\mathbf{T_l}\dot{\boldsymbol{\varepsilon}}_{\mathbf{kk}}$, where $\dot{\boldsymbol{\varepsilon}}_{\mathbf{kk}} = \dot{\boldsymbol{\varepsilon}}_{\mathbf{rr}} + \dot{\boldsymbol{\varepsilon}}_{\boldsymbol{\theta\theta}} + \dot{\boldsymbol{\varepsilon}}_{\mathbf{zz}}$ is the volumetric strain rate defined in the cylindrical coordinates, is the energy dissipated to the generation of mechanical disturbance. Properties κ_l represents the lattice thermal conductivity, C_l is the lattice heat capacity, and τ_l in Eq. (29) is the thermal relaxation time constant of lattices which renders a finite thermal transport velocity for the thermal diffusions of lattice. All the relevant properties above are calculated with respect to the field vector of temperature $\mathbf{T_l}$, which contains both r- and z- components. λ and μ are the Lamé constants and α' is the coefficient of thermal expansion.

Therefore, aiming to describe the field equations Eqs. (28) and (29) into the cylindrical coordinate (r- and z- directions), the specific expression is followed as,

$$C_e\left(T_e\left(z,r\right)\right)\frac{\partial T_e\left(z,r\right)}{\partial t} = -\frac{\partial q_{er}}{\partial r} - \frac{q_{er}}{r} - \frac{\partial q_{ez}}{\partial z} - G\left(T_e\left(z,r\right)-T_l\left(z,r\right)\right) + S\left(z,r\right) \tag{30}$$

$$\tau_e \frac{\partial q_{er}}{\partial t} + q_{er} = -\kappa_e \frac{\partial T_e(z,r)}{\partial r} \tag{31}$$

$$\tau_e \frac{\partial q_{ez}}{\partial t} + q_{ez} = -\kappa_e \frac{\partial T_e(z,r)}{\partial z} \tag{32}$$

$$\begin{aligned} C_l\left(T_l(z,r)\right)\frac{\partial T_l(z,r)}{\partial t} &= -\frac{\partial q_{lr}}{\partial r} - \frac{q_{lr}}{r} - \frac{\partial q_{lz}}{\partial z} \\ &+G\left(T_e(z,r) - T_l(z,r)\right) - (3\lambda + 2\mu)\alpha' T_l(z,r)\cdot\left(\dot{\boldsymbol{\varepsilon}}_{\mathbf{rr}} + \dot{\boldsymbol{\varepsilon}}_{\boldsymbol{\theta\theta}} + \dot{\boldsymbol{\varepsilon}}_{\mathbf{zz}}\right) \end{aligned} \tag{33}$$

$$\tau_l \frac{\partial q_{lr}}{\partial t} + q_{lr} = -\kappa_l \frac{\partial T_l(z,r)}{\partial r} \tag{34}$$

$$\tau_l \frac{\partial q_{lz}}{\partial t} + q_{lz} = -\kappa_l \frac{\partial T_l(z,r)}{\partial z} \tag{35}$$

It is understood that subscripts r and z represent, respectively, the radial and thickness directions.

As discussed in the previous section that the thermophysical properties need to consider the grain size effect in polycrystalline metallic films, since they greatly govern the electrical, electron thermal diffusion and electron-lattice energy exchange during non-equilibrium energy transport. For polycrystalline metallic films, the electrical and thermal conductivity are found to be greatly reduced from the corresponding bulk values and varied due to the averaged grain diameter, which can be theoretically explained by the (grain) size effects on resistivity and scattering due not only to the film surface, but also the grain boundaries [14]. Furthermore, the temperature-dependency on electron heat capacity is considered to be prominent especially at higher laser irradiating fluence. Therefore, the modification of significant thermophysical properties, including electron thermal conductivity and electron-phonon coupling factor, are adopted in the present

model, and the previously proposed expression of the electron heat capacity with temperature-dependency is also incorporated. Here the electron heat capacity C_e, electron thermal conductivity κ_e and electron-phonon coupling factor G are respectively expressed by Eqs. (36) – (44).

$$\begin{cases} C_e(\mathbf{T_e}) = C_{eo}\mathbf{T_e} \quad , & T_e < T_F/\pi^2 \\ C_e(\mathbf{T_e}) = 2C_{eo}\mathbf{T_e}/3 + C_e^{'}/3 \quad , & T_F/\pi^2 \le T_e < 3T_F/\pi^2 \\ C_e(\mathbf{T_e}) = nk_B + C_e^{'}/3 \quad , & 3T_F/\pi^2 \le T_e < T_F \\ C_e(\mathbf{T_e}) = 3nk_B/2 \quad , & T_e \ge T_F \end{cases} \tag{36}$$

With

$$C_e^{'} = C_{eo}\frac{T_F}{\pi^2} + \frac{\frac{3}{2}nk_B - C_{eo}\frac{T_F}{\pi^2}}{T_F - \frac{T_F}{\pi^2}}\left(\mathbf{T_e} - \frac{T_F}{\pi^2}\right) \tag{37}$$

Where C_{eo} is a coefficient for the electron heat capacity, n is the free electron density, k_B is the Boltzmann constant and T_F is the Fermi temperature.

Thermal conductivity of metal is characterized by electron mean-free-path, Λ and is further established considering the effects of surface scattering and grain boundary scattering, with the incorporated to the ratio of the electronic mean-free-path, as

$$\frac{\kappa_{e,f}(T_e, T_l)}{\kappa_{eq,b}(T_l)} = \frac{C_e(T_e)}{C_e(T_l)} \cdot \frac{\Lambda_f(T_l)}{\Lambda_b(T_l)} \tag{38}$$

Where $\kappa_{e,f}(\mathbf{T_e}, \mathbf{T_l})$ and $\kappa_{eq,b}(\mathbf{T_l})$ denote the film and bulk electron thermal conductivities, respectively. $C_e(\mathbf{T_e})/C_e(\mathbf{T_l})$ is the ratio of electron heat capacity and Λ_f/Λ_b is the ratio of electronic mean-free-path. $\kappa_{eq,b}(\mathbf{T_l})$ is defined as the bulk value

corresponding to the electron mean-free-path of the equilibrium state at the reference lattice temperature $T_l = 300\mathrm{K}$ as,

$$\kappa_{eq,b}(\mathbf{T_l}) = \frac{\pi^2 n k_B{}^2}{3m\upsilon_F} \cdot \mathbf{T_l} \cdot \Lambda_b(T_l) \tag{39}$$

With *m* being the effective mass and υ_F the speed of electron, respectively. And the ratio of electronic mean-free-path is obtained as,

$$\frac{\Lambda_f}{\Lambda_b} = \left(1 + \frac{3}{8\beta}(1-P) + \frac{7}{5}\alpha\right)^{-1} \tag{40}$$

Where $\alpha = R_f \Lambda_b / (1 - R_f) / D$ is the grain diameter parameter and $\beta = L/\Lambda_b$ is the film thickness parameter with *L* being the film thickness, *D* the averaged grain diameter, R_f the electron reflectivity at grain boundary and *P* the specular reflection parameter at surface. In the present study, *P* is set to be zero for the reason that the reflection of electrons at film surface is diffusive for most metallic films. The expression for the temperature-dependent ratio of electron heat capacity is,

$$\frac{C_e(T_e)}{C_e(T_l)} = \frac{\left(\varphi_e{}^2 + 0.16\right)^{5/4}\left(\varphi_e{}^2 + 0.44\right)\varphi_e}{\left(\varphi_e{}^2 + 0.092\right)^{1/2}\left(\varphi_e{}^2 + \eta\varphi_l\right)} \tag{41}$$

Where $\varphi_e \equiv \mathbf{T_e}/T_F$ and $\varphi_l \equiv \mathbf{T_l}/T_F$ are the vectors of normalized electron and lattice temperatures, and η is a constant equal to 0.16. Thus, the finalized form of electron thermal conductivity is obtained by combing Eqs. (38) – (41) as,

$$\frac{\kappa_{e,f}}{\kappa_{eq,b}} = \frac{\left(\varphi_e{}^2 + 0.16\right)^{5/4}\left(\varphi_e{}^2 + 0.44\right)\varphi_e}{\left(\varphi_e{}^2 + 0.092\right)^{1/2}\left(\varphi_e{}^2 + \eta\varphi_l\right)} \cdot \left[1 + \frac{3}{8\beta}(1-P) + \frac{7}{5}\alpha\right]^{-1} \tag{42}$$

And the electron-phonon coupling factor G of a polycrystalline film with the thickness *L* and averaged grain diameter *D* and electronic mean-free-path Λ_f is expressed as,

$$\frac{G}{G_b} = \frac{\Lambda_b}{\Lambda_f} = 1 + \frac{3}{8\beta}(1-P) + \frac{7}{5}\alpha \tag{43}$$

where the bulk value G_b is obtained in the equilibrium state, taking into account phonon emission and absorption probability as [3],

$$G_b = \frac{9}{16} \cdot \frac{n k_B^{\,2} T_D^{\,2} \upsilon_F}{\Lambda_b (T_l) T_l E_F} \tag{44}$$

where T_D is the Debye temperature and E_F is the Fermi energy that corresponds to Λ_b =400Å, the electron mean-free-path of the bulk material at T_l =300 K.

3.2.5. Constitutive Equations for Three-Dimensional Thermo-Elasticity

The equations of motion expressed in the cylindrical coordinates are,

$$\rho \frac{\partial^2 u_r}{\partial t^2} = \frac{\partial \sigma_{rr}}{\partial r} + \frac{\partial \sigma_{rz}}{\partial z} + \frac{\sigma_{rr} - \sigma_{zz}}{r} \tag{45}$$

$$\rho \frac{\partial^2 u_z}{\partial t^2} = \frac{\partial \sigma_{rz}}{\partial r} + \frac{\partial \sigma_{zz}}{\partial z} + \frac{\sigma_{rz}}{r} \tag{46}$$

where u_r and u_z denote the displacement components in the r- and z-direction, respectively. ρ is the material density. The constitutive law is defined using the normal stress, σ_{ii}, and shear stress, σ_{rz} as,

$$\sigma_{ii} = 2\mu\varepsilon_{ii} + \lambda\varepsilon_{kk} - (3\lambda + 2\mu)\alpha'(T_l - T_0) \quad , \quad i = r, \theta, z \tag{47}$$

$$\sigma_{rz} - 2\mu\varepsilon_{rz} \tag{48}$$

With ε_{ii} and ε_{rz} being strains. In the present study a low laser fluence of 13. 4J/m^2 with a 0.1ps pulse duration is applied to irradiate the film surface. The corresponding laser intensity is insufficient to generate plastic deformation or inflict heat-affected zone. Thus, only elastic strains need be considered,

$$\varepsilon_{rr}=\frac{\partial u_r}{\partial r};\quad \varepsilon_{zz}=\frac{\partial u_z}{\partial z};\quad \varepsilon_{\theta\theta}=\frac{u_r}{r};\quad \varepsilon_{rz}=\frac{1}{2}\left(\frac{\partial u_r}{\partial z}+\frac{\partial u_z}{\partial r}\right) \tag{49}$$

3.3. Computational Scheme

3.3.1. Initial and Boundary Conditions

An optical source of 0.1ps in pulse duration, 630nm in wavelength and 13.4J/m^2 in laser fluence is employed. It is noted that these optical parameters followed from the experimental work reported in Ref. [13]. The spot radius of the Gaussian beam is r_s =1μm. With an ambient temperature T_o =300K, the following initial and boundary conditions are defined for the model system as,

$$\begin{gathered}
T_e(z,r,0)=T_l(z,r,0)=T_0 \\
q_{er}(z,r,0)=q_{ez}(z,r,0)=0 \\
q_{lr}(z,r,0)=q_{lz}(z,r,0)=0 \\
\sigma_{rr}(z,r,0)=\sigma_{\theta\theta}(z,r,0)=\sigma_{zz}(z,r,0)=\sigma_{rz}(z,r,0)=0 \\
u_r(z,r,0)=\dot{u}_r(z,r,0)=0 \\
u_z(z,r,0)=\dot{u}_z(z,r,0)=0
\end{gathered} \tag{50}$$

And

$$q_{er}\left(z,0,t\right)=q_{er}\left(z,r_{\max},t\right)=0$$

$$q_{ez}\left(0,r,t\right)=q_{ez}\left(z_{\max},r,t\right)=0$$

$$q_{lr}\left(z,0,t\right)=q_{lr}\left(z,r_{\max},t\right)=0$$

$$q_{lz}\left(0,r,t\right)=q_{lz}\left(z_{\max},r,t\right)=0 \qquad (51)$$

$$\sigma_{zz}\left(0,r,t\right)=\sigma_{zz}\left(z_{\max},r,t\right)=0$$

$$\sigma_{rz}\left(0,r,t\right)=\sigma_{rz}\left(z_{\max},r,t\right)=0$$

$$u_{r}\left(z,r_{\max},t\right)=0$$

Given that the laser pulse duration is extremely short, all heat fluxes on the exposed faces are assumed to be negligible. The boundary conditions for the mechanical field are traction-free for both the front ($z=0$) and back ($z=z_{\max}$) faces of the film model. The circumference ($r=r_{\max}$) is constrained in the r-direction.

3.3.2. Finite Difference Scheme of Three-Dimensional Model

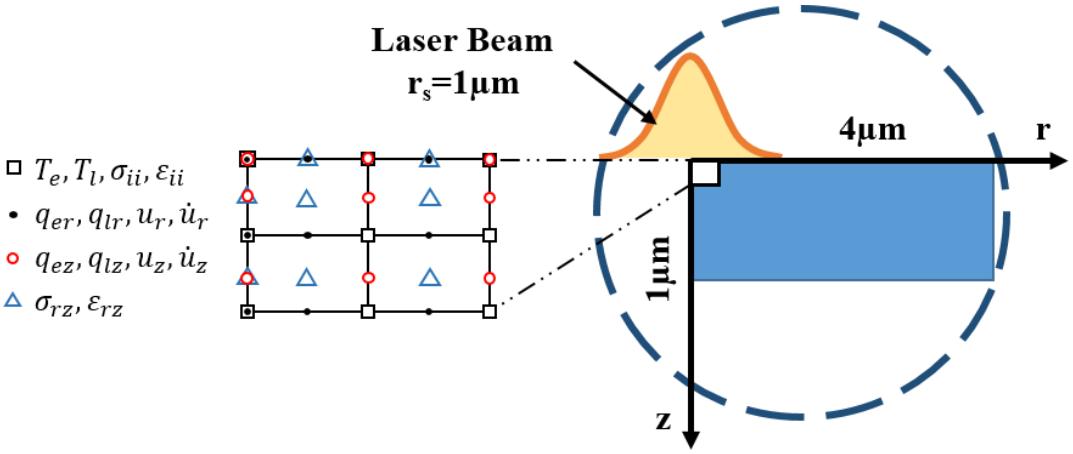

Figure 9. Staggered-grid finite different scheme

The model domain is an orthogonal rectangle section with 1μm in thickness and 4μm in radius as shown in Figure 9. 100 mesh grids along the depth direction and 200 mesh grids along the radial direction are used to ensure proper convergence and minimal computational error. During non-equilibrium of the energy transport process, a time step of 0.2fs is applied. After equilibrium is reached, a larger time step of 0.5fs is followed to time-integrate the evolutions of both the thermal and mechanical responses from the equilibrium state up to t=30ps.

The inherent complexity of the coupled governing equations of motion renders the use of conventional finite difference method inefficient for numerically resolving the field response. In addition to the primary variables $\mathbf{T_e}$ and $\mathbf{T_l}$, first-order spatial derivate terms q_{er} and q_{ez}, shear stress σ_{rz}, and velocity variables $\dot{u}_r$ and $\dot{u}_z$ also need be time-

integrated. A finite difference method with staggered grids in Ref. [9] and [11] is employed in the study to address the noted complexity. Figure 9 gives the schematic of the staggered-grid finite difference scheme. All primary variables ($\mathbf{T_e}$ and $\mathbf{T_l}$, normal stresses $\boldsymbol{\sigma_{ii}}$ and normal strains ε_{ii}) are resolved at grid points. The velocity fields $\dot{u}_r$ and $\dot{u}_z$ and the first-order spatial derivative terms ($\partial/\partial r$ and $\partial/\partial z$) are determined halfway between two consecutive grid points. Shear stresses σ_{rz} are calculated at the center location surrounded by velocity components. By using the staggered-grid finite difference scheme along with a sufficiently small time step, numerical oscillations are properly controlled and avoided. When calculations are performed on grid points located at r=0 (the center line of the film model) that involve the $1/r$ term, the L'Hôpital's rule is applied to $1/r$ which is undefined. They are replaced with the corresponding partial derivative of r, i.e. $\lim_{r\to 0}(u/r) = \partial u/\partial r|_{r=0}$.

3.3.3. Numerical Discretization

As an illustration, Eqs. (30) – (35), and (45) – (49) are the field equations expressed in asymmetric model (three-dimensional model) and govern the entire thermo-elasto-dynamics of polycrystalline metallic films during non-equilibrium state in response to the ultrafast laser irradiation. Of these equations, Eqs. (30) – (32) define the energy transport dynamics in electron subsystem, while others define the lattice energy transport by the coupled thermal-mechanical fields. During each time-iterative step, Eq. (27) updates the spatial profile of the laser source term in the cylindrical coordinate (r- and z- direction). And all the Eqs. (36), (37) and (42) denote the significant thermophysical properties

during the dynamic process and are updated with respect to the r- and z- components of variable vector $\mathbf{T_e}$ and $\mathbf{T_l}$. When thermal equilibrium arrives ($T_e = T_l$), the energy source term $G(T_e - T_l)$ in Eq. (33) becomes negligible with its effect on the lattice dynamics and thus is eliminated to generate a simplified form of Eq. (33). As such, the simplified Eq. (33) along with Eqs. (45) – (49) take over the subsequent physical dynamics in the state of post-equilibrium.

As exhibited below, the essential discretized equations of the involved variables that are arranged following the staggered-grid scheme are expressed as,

$$\begin{aligned} T_e(j,i,p+1) = {} & T_e(j,i,p) - \frac{\Delta t}{C_e\left(T_e(j,i,p)\right)}\left[\frac{q_{er}(j,i-1,p) - q_{er}(j,i+1,p)}{\Delta r}\right] \\ & - \frac{\Delta t}{C_e\left(T_e(j,i,p)\right)}\frac{1}{r}\left[\frac{q_{er}(j,i-1,p) + q_{er}(j,i+1,p)}{2}\right] \\ & - \frac{\Delta t}{C_e\left(T_e(j,i,p)\right)}\left[\frac{q_{ez}(j-1,i,p) - q_{ez}(j+1,i,p)}{\Delta z}\right] \\ & - \frac{\Delta t}{C_e\left(T_e(j,i,p)\right)}G\left[T_e(j,i,p) - T_l(j,i,p)\right] \\ & + \frac{\Delta t}{C_e\left(T_e(j,i,p)\right)}\cdot S(j,i,p) \end{aligned} \tag{52}$$

$$\begin{aligned} q_{er}(j,i+1,p+1) = {} & \left(1 - \frac{\Delta t}{\tau_e}\right)q_{er}(j,i+1,p) \\ & - \frac{\Delta t}{\tau_e}\left(\frac{\kappa_e(j,i+2,p) + \kappa_e(j,i,p)}{2}\right)\cdot\left(\frac{T_e(j,i,p) - T_e(j,i+2,p)}{\Delta r}\right) \end{aligned} \tag{53}$$

$$\begin{aligned} q_{ez}(j+1,i,p+1) = {} & \left(1 - \frac{\Delta t}{\tau_e}\right)q_{ez}(j+1,i,p) \\ & - \frac{\Delta t}{\tau_e}\left(\frac{\kappa_e(j+2,i,p) + \kappa_e(j,i,p)}{2}\right)\cdot\left(\frac{T_e(j,i,p) - T_e(j+2,i,p)}{\Delta z}\right) \end{aligned} \tag{54}$$

$$
\begin{aligned}
T_l(j,i,p+1) &= T_l(j,i,p) - \frac{\Delta t}{C_l(T_l)}\left[\frac{q_{lr}(j,i-1,p) - q_{lr}(j,i+1,p)}{\Delta r}\right] \\
&- \frac{\Delta t}{C_l}\frac{1}{r}\left[\frac{q_{lr}(j,i-1,p) + q_{lr}(j,i+1,p)}{2}\right] \\
&- \frac{\Delta t}{C_l}\left[\frac{q_{lz}(j-1,i,p) - q_{lz}(j+1,i,p)}{\Delta z}\right] \\
&+ \frac{\Delta t}{C_l} G\left[T_e(j,i,p) - T_l(j,i,p)\right] \\
&- \frac{\Delta t}{C_l}(3\lambda + 2\mu)\alpha' T_l(j,i,p)\left[\dot{\varepsilon}_{rr}(j,i,p) + \dot{\varepsilon}_{\theta\theta}(j,i,p) + \dot{\varepsilon}_{zz}(j,i,p)\right]
\end{aligned}
\tag{55}
$$

$$
\begin{aligned}
q_{lr}(j,i+1,p+1) &= \left(1 - \frac{\Delta t}{\tau_l}\right) q_{lr}(j,i+1,p) \\
&- \frac{\Delta t}{\tau_l} \cdot \kappa_l \cdot \left(\frac{T_l(j,i,p) - T_l(j,i+2,p)}{\Delta r}\right)
\end{aligned}
\tag{56}
$$

$$
\begin{aligned}
q_{lz}(j+1,i,p+1) &= \left(1 - \frac{\Delta t}{\tau_l}\right) q_{lz}(j+1,i,p) \\
&- \frac{\Delta t}{\tau_l} \cdot \kappa_l \cdot \left(\frac{T_l(j,i,p) - T_l(j+2,i,p)}{\Delta z}\right)
\end{aligned}
\tag{57}
$$

$$
\begin{aligned}
&\dot{u}_z\left(j+\frac{1}{2},i,p+1\right) \\
&= \dot{u}_z\left(j+\frac{1}{2},i,p\right) + \frac{\Delta t}{\rho}\left[\frac{\sigma_{rz}\left(j+\frac{1}{2},i-\frac{1}{2},p\right) - \sigma_{rz}\left(j+\frac{1}{2},i+\frac{1}{2},p\right)}{\Delta r}\right] \\
&+ \frac{\Delta t}{\rho}\left[\frac{\sigma_{zz}(j,i,p) - \sigma_{rz}(j+1,i,p)}{\Delta z}\right] \\
&+ \frac{\Delta t}{\rho}\frac{1}{r}\left[\frac{\sigma_{rz}\left(j+\frac{1}{2},i-\frac{1}{2},p\right) + \sigma_{rz}\left(j+\frac{1}{2},i+\frac{1}{2},p\right)}{2}\right]
\end{aligned}
\tag{58}
$$

$$\dot{\varepsilon}_{rr}\left(j,i,p\right)=\frac{\dot{u}_r\left(j,i-\frac{1}{2},p\right)-\dot{u}_r\left(j,i+\frac{1}{2},p\right)}{\Delta r} \tag{59}$$

$$\dot{\varepsilon}_{\theta\theta}\left(j,i,p\right)=\frac{\dot{u}_r\left(j,i-\frac{1}{2},p\right)+\dot{u}_r\left(j,i+\frac{1}{2},p\right)}{2}\frac{1}{r} \tag{60}$$

$$\dot{\varepsilon}_{zz}\left(j,i,p\right)=\frac{\dot{u}_z\left(j-\frac{1}{2},i,p\right)-\dot{u}_z\left(j+\frac{1}{2},i,p\right)}{\Delta z} \tag{61}$$

$$\dot{\varepsilon}_{rz}\left(j+\frac{1}{2},i+\frac{1}{2},p\right)=\frac{1}{2}\left[\begin{array}{l}\dfrac{\dot{u}_r\left(j,i+\frac{1}{2},p\right)-\dot{u}_r\left(j+1,i+\frac{1}{2},p\right)}{\Delta z}\\ +\dfrac{\dot{u}_z\left(j+\frac{1}{2},i,p\right)-\dot{u}_z\left(j+\frac{1}{2},i+1,p\right)}{\Delta r}\end{array}\right] \tag{62}$$

$$\begin{aligned}\sigma_{rr}\left(j,i,p+1\right)&=\sigma_{rr}\left(j,i,p\right)\\&+\Delta t\left[2\mu\dot{\varepsilon}_{rr}\left(j,i,p\right)+\lambda\left(\dot{\varepsilon}_{rr}\left(j,i,p\right)+\dot{\varepsilon}_{\theta\theta}\left(j,i,p\right)+\dot{\varepsilon}_{zz}\left(j,i,p\right)\right)\right]\\&-\left(3\lambda+2\mu\right)\alpha'\left[T_l\left(j,i,p+1\right)-T_l\left(j,i,p\right)\right]\end{aligned} \tag{63}$$

$$\begin{aligned}\sigma_{\theta\theta}\left(j,i,p+1\right)&=\sigma_{\theta\theta}\left(j,i,p\right)\\&+\Delta t\left[2\mu\dot{\varepsilon}_{\theta\theta}\left(j,i,p\right)+\lambda\left(\dot{\varepsilon}_{rr}\left(j,i,p\right)+\dot{\varepsilon}_{\theta\theta}\left(j,i,p\right)+\dot{\varepsilon}_{zz}\left(j,i,p\right)\right)\right]\\&-\left(3\lambda+2\mu\right)\alpha'\left[T_l\left(j,i,p+1\right)-T_l\left(j,i,p\right)\right]\end{aligned} \tag{64}$$

$$\begin{aligned}\sigma_{zz}\left(j,i,p+1\right)&=\sigma_{zz}\left(j,i,p\right)\\&+\Delta t\left[2\mu\dot{\varepsilon}_{zz}\left(j,i,p\right)+\lambda\left(\dot{\varepsilon}_{rr}\left(j,i,p\right)+\dot{\varepsilon}_{\theta\theta}\left(j,i,p\right)+\dot{\varepsilon}_{zz}\left(j,i,p\right)\right)\right]\\&-\left(3\lambda+2\mu\right)\alpha'\left[T_l\left(j,i,p+1\right)-T_l\left(j,i,p\right)\right]\end{aligned} \tag{65}$$

$$\sigma_{rz}\left(j+\frac{1}{2},i+\frac{1}{2},p+1\right)=\sigma_{rz}\left(j+\frac{1}{2},i+\frac{1}{2},p\right)+\Delta t\cdot 2\mu\dot{\varepsilon}_{rz}\left(j+\frac{1}{2},i+\frac{1}{2},p\right) \tag{66}$$

where j and i are the grid indices in the z- and r- direction, respectively, p denotes the previous time while $p+1$ denotes the new time after one time step Δt, and the "$1/2$" index represents halfway between two consecutive grid points.

3.4. Model Validation

The model formulations presented in the above part are evaluated against the physical data found in Ref. [13] using the material properties of gold. An optical source of 630nm in wavelength, 100fs in pulse width, and 13.4J/m^2 in fluence is applied to a film of 100nm in thickness. It is noted that these laser parameters along with the specific film thickness follow from the settings as employed in experiment so that the theoretical changes of the normalized electron temperature are to be assessed and compared with the corresponding experimental measurements published in [13].

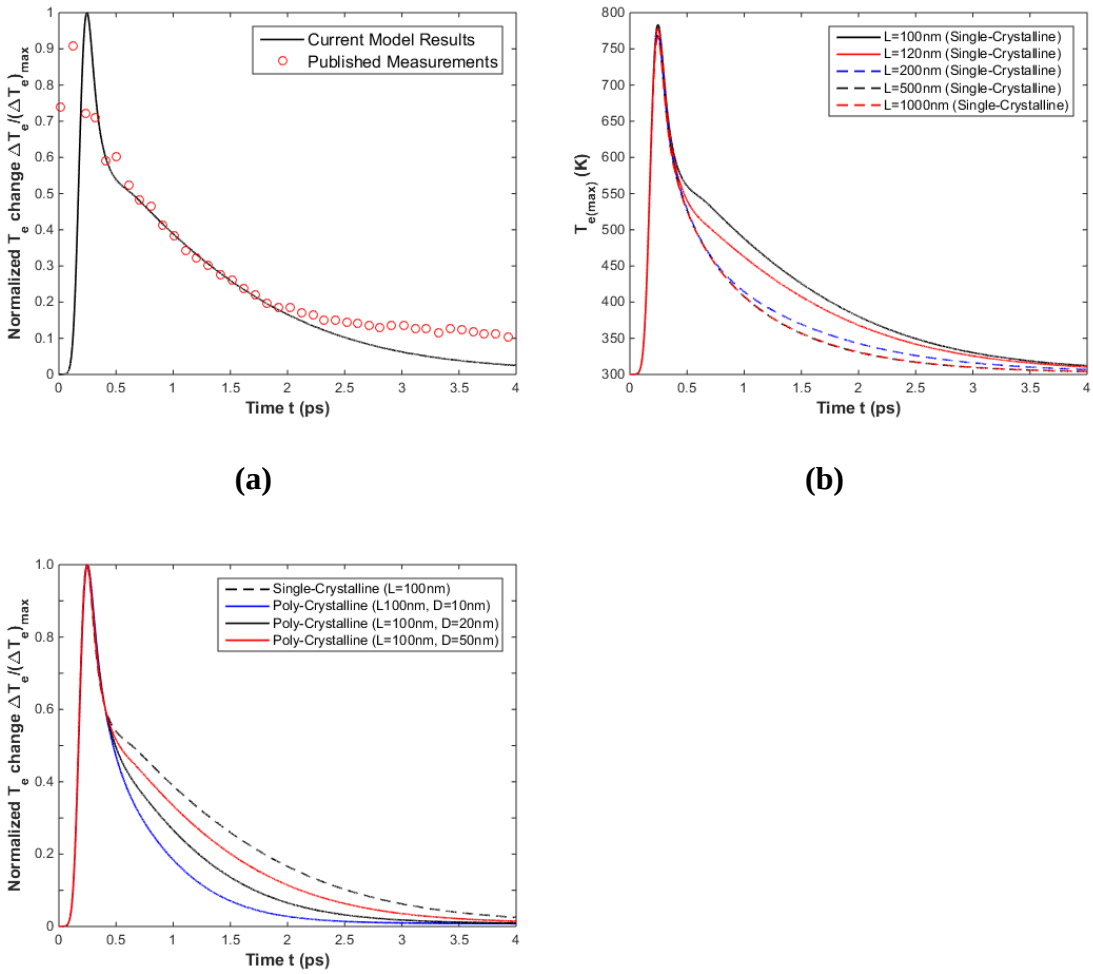

Figure 10. Temperture time profiles

(a) Comparison of normalized electron temperatures with experimental result; (b) maximum electron temperatures in single-crsytalline films of different film thicknesses; (c) normalized electron temperatures in poly-crystalline films of different averaged grain diameters

Variations of the electron temperature at the center of the irradiated surface at (z=0, r=0) as predicted by the axisymmetric model and per the experimental data are considered in Figure 10. The following thermophysical properties are adopted from Ref. [12]: 315W/(m·K) for both the electron and lattice thermal conductivities, 2.1×10^{4}J/(m^{3}·K) for the electron heat capacity, 2.5×10^{6}J/(m^{3}·K) for the lattice heat capacity, and 2.6×10^{16}W/(m^{3}·K) for the electron-phonon coupling factor. These properties are for a type of single crystalline material as the electron thermal conductivity and e-ph coupling factor are different from those of its polycrystalline counterpart's. It is necessary that the two properties be derived from their respective bulk value by using Eqs. (39) and (44), respectively. As there are no definitive grain boundaries in single crystalline nanostructure, the corresponding grain diameter must be α=0 to signify no scattering when calculating κ_e and G. Figure 10(a) shows that the calculated normalized electron temperature for the single crystalline film of 100nm in thickness is in good agreement with the physical data. While the instrumentation employed in Ref. [13] is insufficient for resolving non-equilibrium heating prior to t=0.5ps, the escalation of the non-equilibrium electron temperature is nonetheless properly described by the presented model. A parametric study considering different single-crystalline film thicknesses ranging from L=100nm up to L=1μm is presented in Figure 10(b). It is seen that the deviation is prominent among the thinner films and becomes negligible when the thickness exceeds 500nm. When the film thickness is comparably small, increase in thickness results in a larger cooling rate of the electron temperature and, thus, a more rigorous energy transfer in the near-field. Several averaged grain sizes (D=10nm, 20nm and 50nm) are considered

in Figure 10(c) with the polycrystalline films having the same thickness, L=100nm. The variation of grain size renders an opposite correction to the normalized electron temperature, $\Delta T_e/(\Delta T_e)_{\max}$ as indicated in Figure 10(c) - the cooling rate declines faster in the polycrystalline thin films with the decrease of the averaged grain diameter. The enhanced electron temperature cooling rate predicted for the polycrystalline films also agrees with the physical results reported in Ref. [10]. Validation of the predicted normalized electron temperature for polycrystalline metallic films with different film thicknesses and averaged grain diameters can be readily conducted using the transient thermoreflectance (TTR) [15] or other pump-probe techniques such as the time-domain thermoreflectance (TDTR) [16].

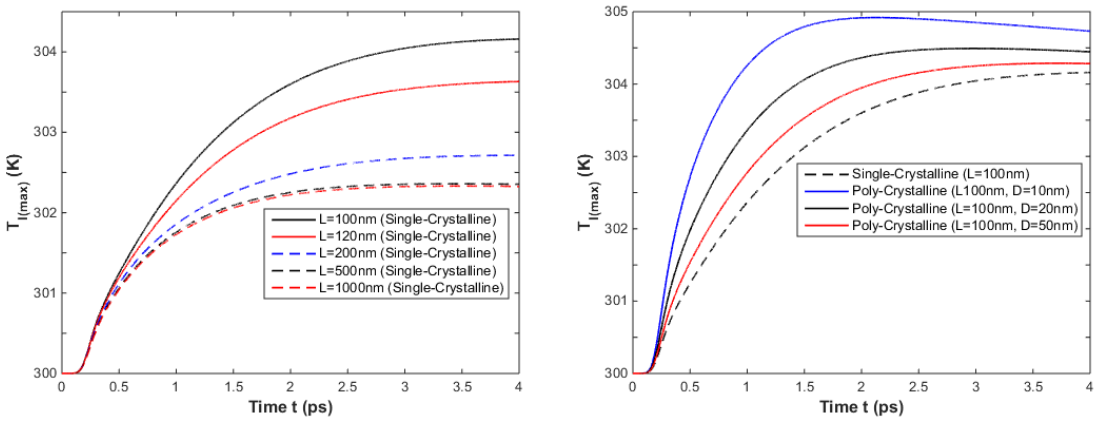

(a) **(b)**

Figure 11. Size effects on maximum lattice temperature

(a) Size effect (varying thicknesses) on maximum lattice temperature; (b) Size effect (varying grain sizes) on maximum lattice temperature

Considering that a slight difference in the lattice temperature can manifest tino a characteristically different response in the mechanical field [17], the corresponding maximum lattice temperatures due to the variation of the film thickness and the averaged grain diameter are plotted in Figure 11. As indicated in Figure 11(a), the deviation is negligible when the film thickness is greater than 500nm. However, the maximum lattice temperature increases when the thickness is comparably smaller. Unlike the lattice temperature of the single crystalline film, all the temperature profiles of the polycrystalline films feature a steeper climb and reach a plateau sooner as seen in Figure 11(b). It is also noted that smaller averaged grain sizes are associated with a higher rate of temperature increase in the polycrystalline films. Figure 10 and Figure 11 indicate that the effects of the grain size and film thickness on the thermal field are so prominent that the 2 parameters are non-negligible for characterizing the polycrystalline thin films.

3.5. Summary

The study on the fundamental mechanism underlying the thermal-mechanical responses in both single- and polycrystalline metallic films subject to the ultrafast laser heating was further explored using a three-dimensional model. The thermo-elasto-dynamics features hyperbolic energy transport equations and incorporates thermophysical properties that are functions of size effects and temperature dependency. The formulation was implemented using an axisymmetric numerical model to resolve the rapid energy transport in both the electron and lattice subsystems and the induced thermo-elastic wave propagation. To numerically resolve the proposed asymmetric model, a staggered-grid finite difference scheme was provided to time-integrate the coupled thermal-mechanical

field equations to establish the evolutions of temperature and normal and shear stresses in space. Specifically, the essential discretized equations of the involved variables are exhibited as an illustration for implementing the computational process due to its complexity and multi-dimensionality. Since physical data acquired for polycrystalline metallic films are rarely available, model validation was established by favorably considering the numerically obtained normalized electron temperature of a single crystalline gold film against the experimental results found in Ref. [13]. The implications for being able to study the impact of grain sizes on energy transport using the model formulation are many.

3.6. References

[1] Sakakura, M., Fukuda, N., Shimotsuma, Y., and Miura, K., "Dynamics of interference of femtosecond laser-induced stress waves and crack formation inside a LiF single crystal," *Laser Applications in Microelectronic and Optoelectronic Manufacturing (LAMOM) XIX*, Vol. 8967, 2014, pp. 89670C.

[2] Sakakura, M., Ishiguro, Y., Shimotsuma, Y., Fukuda, N., and Miura, K., "Modulation of transient stress distributions for controlling femtosecond laser-induced cracks inside a single crystal," *Applied Physics A*, Vol. 114, No. 1, 2014, pp. 261-265.

[3] Qiu, T. Q. and Tien, C. L., "Size Effects on Nonequilibrium Laser Heating of Metal Films," *Journal of Heat Transfer*, Vol. 115, No. 4, 1993, pp. 842-847.

[4] Fan, L.-S., Tai, Y.-C., and Muller, R. S., "Integrated Movable Micromechanical Structures for Sensors and Actuators," *IEEE Transactions on Electron Devices*, Vol. 35, No. 6, 1988, pp. 24-730.

[5] Qi, X., and Suh, C. S., "Ultrafast Laser-Induced Elastodynamics in Single Crystalline Silicon Part II: Near-Field Response," *Journal of Thermal Stresses*, Vol. 32, No. 5, 2009, pp. 494-511.

[6] Qiu, T. Q., and Tien, C. L., "Heat Transfer Mechanisms During Short-Pulse Laser Heating of Metals," *Journal of Heat Transfer*, Vol. 115, No. 4, 1993, pp. 835-841.

[7] Hohlfeld, J., Wellershoff, S.-S., Güdde, J., Conrad, U., Jähnake, V., and Matthias, E., "Electron and Lattice Dynamics Following Optical Excitation of Metals," *Chemical Physics*, Vol. 251, No. 1, 2000, pp. 237-258.

[8] Chen, J. K., and Beraun, J. E., "Numerical Study of Ultrashort Laser Pulse Interactions with Metal Films," *Numerical Heat Transfer: Part A: Applications*, Vol. 40, No. 1, 2001, pp. 1-20.

[9] Qi, X., and Suh, C. S., "Ultrafast Laser-Induced Elastodynamics in Single Crystalline Silicon Part I: Model Formulation," *Journal of Thermal Stresses*, Vol. 32, No. 5, 2009, pp. 477-493.

[10] Elsayed-Ali, H. E., Juhasz, T., Smith, G. O., and Bron, W. E., "Femtosecond Thermoreflectivity and Thermotransmissivity of Polycrystalline and Single-Crystalline Gold Films," *Physical Review B*, Vol. 43, No. 5, 1991, pp. 4488.

[11] Qi, X., and Suh, C. S., "Generalized Thermo-Elastodynamics for Semiconductor Material Subject To Ultrafast Laser Heating. Part I: Model Description and

Validation," *International Journal of Heat and Mass Transfer*, Vol. 53, No. 1, 2010, pp. 41-47.

[12] Qiu, T. Q., and Tien, C. L., "Short-Pulse Laser Heating on Metals," *International Journal of Heat and Mass Transfer*, Vol. 35, No. 3, 1992, pp. 719-726.

[13] Qiu, T. Q., Juhasz, T., Suarez, C., Bron, W. E., and Tien, C. L., "Femtosecond Laser Heating of Multi-Layer Metals - II. Experiments," *International Journal of Heat and Mass Transfer*, Vol. 37, No. 17, 1994, pp. 2799-2808.

[14] Durkan, C., and Welland, M. E., "Size Effects in the Electrical Resistivity of Polycrystalline Nanowires," *Physical Review B*, Vol. 61, No. 20, 2000, pp. 14215.

[15] Wang, H. D., Ma, W. G., Zhang, X., Wang, W., and Guo, Z. Y., "Theoretical and experimental study on the heat transport in metallic nanofilms heated by ultra-short pulsed laser," *International Journal of Heat and Mass Transfer*, Vol. 54, No. 4, 2011, pp. 967-974.

[16] Malen, J. A., Baheti, K., Tong, T., Zhao, Y., Hudgings, J. A., and Majumdar, A., "Optical Measurement of Thermal Conductivity Using Fiber Aligned Frequency Domain Thermoreflectance," *Journal of Heat Transfer*, Vol. 133, No. 8, 2011, pp. 081601.

[17] Tsibidis, G. D., "The influence of dynamical change of optical properties on the thermomechanical response and damage threshold of noble metals under femtosecond laser irradiation," *Journal of Applied Physics*, Vol. 123, No. 8, 2018, pp. 085903.

4. THERMO-ELASTO-DYNAMICS OF POLYCRYSTALLINE GOLD FILMS – THERMAL-MECHANICAL DAMAGE MODE

4.1. Introduction

The thermo-elasto-dynamics with three-dimension presented in the previous chapter allows the framework to correlate the temporal and spatial variation of temperature and thermal stress waves with the non-melting ultrafast optical parameters. The temporal profile of the predicted variation of the normalized electron temperature was shown to be in excellent agreement with physical data for a type of single-crystalline gold film. It demonstrated a rapid rise in electron temperature was followed by a relatively more gradual descend that can be characterized by electron and lattice relaxations. The behind mechanism for electron energy transport in the non-equilibrium state is widely accepted that electrons are excited into a higher energy level at which electron-electron collisions are rampant following a specific time scale that is the electron relaxation time. The kinetic energy of the electron subsequently diffuses into the adjacent regions as a hyperbolic electron heat flux. As time elapses, the energy is subsequently transferred to lattices via rigorous electron-phonon collisions. But the subsequent dynamics of energy transport and the mechanism on the ultrafast light laser-induced micro-damage in lattice is still questionable and elusive.

Arbitrated by pulse duration and laser fluence, non-thermal melting threshold is a gauge for avoiding inflicting physical damage to the material being irradiated upon. When the ablation threshold is reached, the phase transition or phase explosion are introduced

into the classical two-temperature model or molecular dynamics by plenty of researches for explaining the physical damage and the corresponding mechanism. Thus, the high lattice temperature and the liquid phase of the recessive surface layer are the consequence following the ultrafast laser heating with high intensities. On the contrary, the micro-damage or crack formation in single crystalline material by the thermo-elastic stress generated by the ultrafast laser heating with light or extremely low intensities has already reported and experimental observed in Ref. [1] and [2]. The phenomena was analyzed to be caused by the anisotropic propagation of the tensile stress leading to the stress concentration in certain directions, and thus forms the cracks. But the underlying physical mechanism on micro-cracking in polycrystalline metallic targets irradiated by the ultrafast light laser is quite different due to the isotropic behavior and lacks a comprehensive understanding. As ultrafast pulses also generate short-time scale shock waves of high frequency and high power density, micro- and macro-cracking are probable. Such damages, however, cannot be estimated or evaluated by non-thermal melting threshold without generating high lattice temperature or high magnitude of stress with the following plastic deformation.

One concept of power density in Ref. [3] – [5] was employed to investigate if such modes of physical damage would likely to occur. The concept was first developed to correlate the thermo-elastic stress waves excited by rapid thermal transient with the various damage modes in a microelectronic packaging configuration. Qualitative correlations were established by considering the temporal gradient of the oscillating elastic stress, which has the unit of power per unit volume. The concept of power density and its

implication on high cycle fatigue involving low stress amplitude provides an effective tool to investigate if pulsing below non-thermal melting threshold would initiate wave motions that wreak dynamic fatigue cracking in the polycrystalline metallic film.

Therefore, the model formulation and the analysis on the resulted thermal-mechanical fields are further studied in this chapter to explore the implication of the transport process in a polycrystalline gold film. The evolutions of the electron and lattice temperatures under non-melting ultrafast irradiation are examined to characterize (1) near-field, coupled thermal-mechanical responses and (2) the generation of propagating waves as functions of material size effects and ultrashort optical input parameters.

In the sections that follow an optical beam of 630nm in wavelength, 100fs in pulse duration, 13.4J/m^2 in fluence and 1μm in spot size is applied to the film which is 1μm (in thickness) by 4μm (in radius). Several different averaged grain sizes are considered to examine the impact of size effects. The implication of considering size effects and thermally induced variation in material properties is in the proper characterization of lattice temperature and the resulted stress gradients that drive thermal stress waves. As these waves are dispersive, characteristically broad in spectral bandwidth and of extremely high power density [3] – [5], an in-depth comprehension of their generation mechanism would help mitigate the adverse effect they are inherent of.

4.2. Three-Dimensional Thermal-Mechanical Fields

4.2.1. Electron Temperature

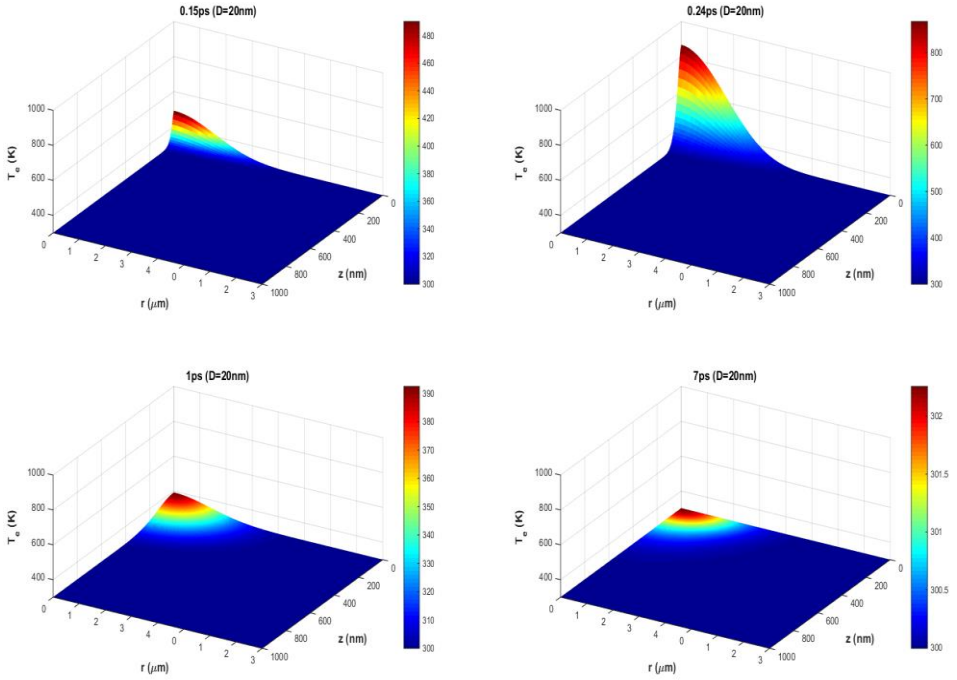

Figure 12. Evolution of electron temperature in polycyrstalline film with D=20nm

Figure 12 and Figure 13, respectively, give the time progression of electron and lattice temperature in the polycrystalline gold film. The characteristic averaged grain diameter of the thin film is D=20nm and the corresponding film thickness parameter is D/L=0.02. Four time instances at t=0.15ps, 0.24ps, 1,0ps and 7.0ps are considered. The thermal field responses indicate a rigorous energy transport process beginning with pulsed

radiation absorption to rapid elevation of electron temperature to gradual increase of lattice temperature. Figure 12 shows that at t=0.24ps, electron temperature T_e rapidly reaches the peak at (z=0, r=0), the center of the model front face. In the near-field, the rise of the electron temperature components in the z-direction demonstrates a definitive time delay than the corresponding ascending in temperature in the r-direction. This is primarily attributed by the optical penetration depth and the characteristic spot size of the laser beam. Due to the optical attenuation along the penetration depth, the region further along the thickness direction registers more energy via thermal diffusion. Additionally, as dictated by the hyperbolic electron heat diffusion that admits finite energy transport velocity, temperature rises blow the irradiated surface ($z<0$) demonstrates a lag compared to the radial electron temperatures on the exposed surface.

4.2.2. Lattice Temperature

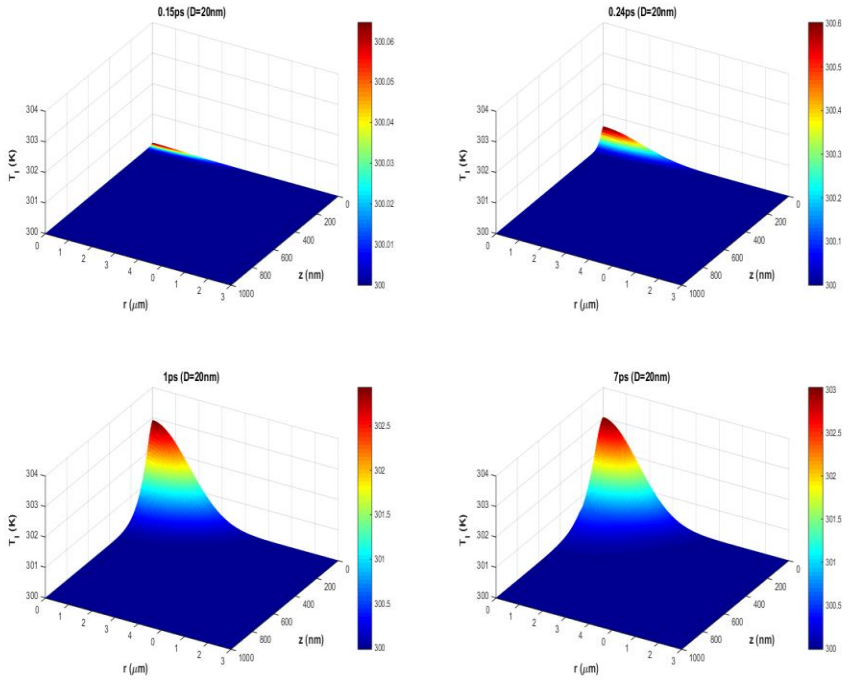

Figure 13. Evolution of lattice temperature in polycyrstalline film with D=20nm

Historically study on lattice temperature does not command the same amount of interests as electron temperature does [6]. There are significantly less efforts, experimental as well as theoretical, reported on ultrafast pulsing induced electron temperatures. Consequently the number of publications on considering coupled thermal-mechanical field responses to ultrafast laser heating are rare. For nanosecond or short pulse heating, physical damages such as heat affected zone are primarily caused by intensified thermal energy. Given their ultrashort pulse duration and limited optical

penetration depth, similar modes of thermal damage are physically not probable for femtosecond pulses. As will be demonstrated in the later part of the paper, albeit of relatively low lattice temperature, the coupled thermal-mechanical field responses associated with non-thermal melting is prominent and non-negligible.

Figure 13 shows the lattice temperature profiles at t=0.15ps, 0.24ps, 1.0ps and 7.0ps. After reaching the peak, the electron temperature starts to drop, bringing about the rise of lattice temperature at the same time. This is the stage in which energy is transferred from electrons to lattices through electron-phonon collisions. Prior to reaching the electron-lattice thermal equilibrium, lattice temperature keeps increasing from the ambient temperature at T=300K. Within the first several picoseconds, e-ph interaction dominates the rise of the lattice temperature rise, while the energy dissipation of lattice dilation is not sufficient enough to disturb. Lattice temperature becomes stabilized when the thermal equilibrium is reached at approximately t=7.0ps. And a maximum lattice temperature of 304K is registered at (z=0, r=0) in response to the 13.4J/m^2 laser input.

4.2.3. Grain Size Effects on Thermal Field

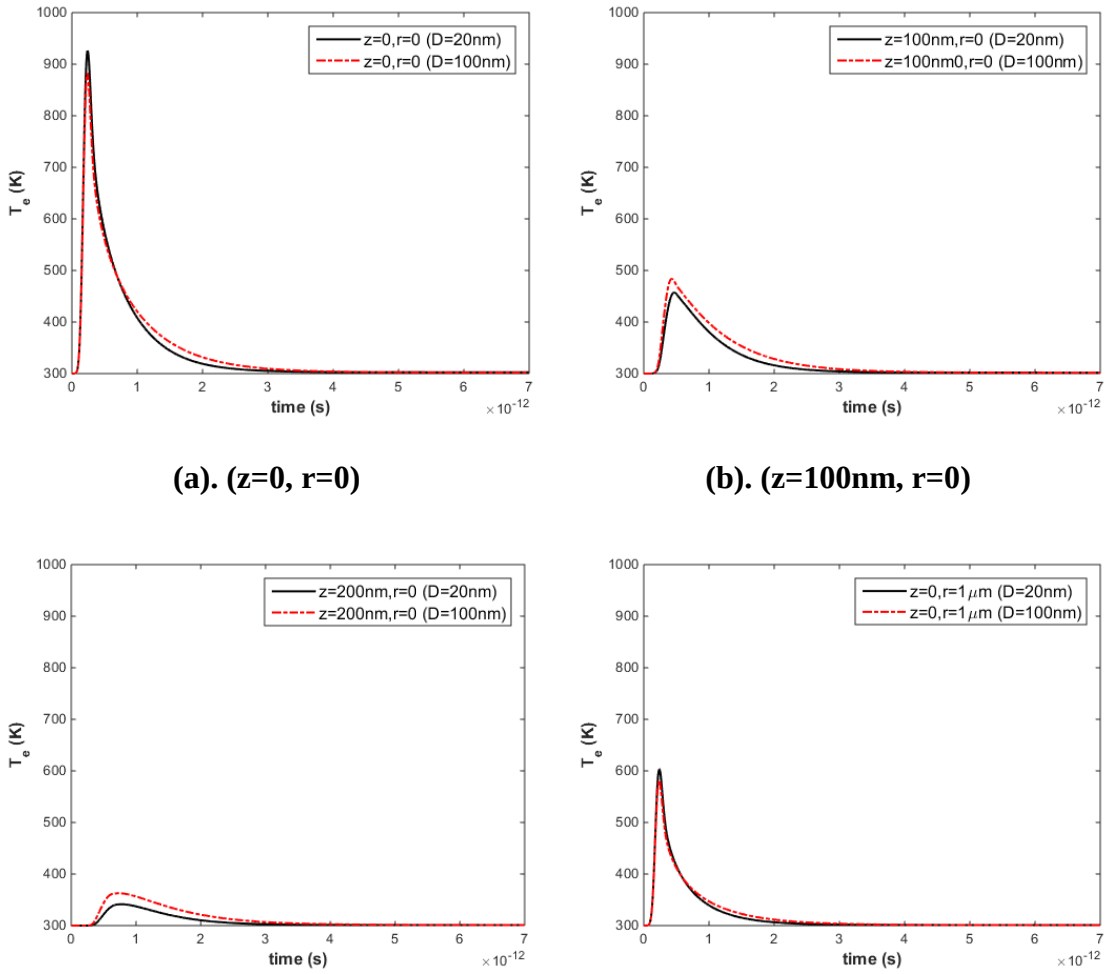

(a). (z=0, r=0) **(b). (z=100nm, r=0)**

(c). (z=200nm, r=0) **(d). (z=0, r=1μm)**

Figure 14. Temporal profiles of T_e for D=20nm and D=100nm at 4 different locations

Figure 14 depicts the temporal profiles of the electron temperature for 2 different averaged grain diameters with D=20nm and D=100nm. 4 different locations are

considered to demonstrate the spatial variations of electron energy transport along the r- and z-direction. Electron energy transfer is dictated by a characteristic (relaxation) time scale that is of the order of 10^{-14} seconds. Within the brief time period, the electron-photon interaction and the electron-electron collisions dominate the electron energy transport process that manifests as rapidly increasing T_e while the corresponding lattice temperature remains unchanged. As electron collisions define electron conductivity, the ensuing electron heat conduction is therefore affected by the averaged grain diameter involved.

The definitive differences registered in the 2 electron temperature profiles including the peak magnitudes and rates of variation in time are exclusively attributable to the size effect. The maximum value of T_e in the film with D=20nm is higher than the maximum T_e's in Figure 14(a) and Figure 14(d) where the corresponding averaged grain diameter is D=100nm. The opposite is true with Figure 14(b) and Figure 14(c) where the maximum T_e's are both higher. This necessarily suggests that more electrons are localized in near-field, thus allowing less energy to be transferred both axially and radially. It has been reported that size effects impact polycrystalline thermophysical properties including electron thermal conductivity and electron-phonon coupling factor in a significant way [7] and [8]. Such an impact can be appreciated by reviewing the following electron thermal conductivity ratio for polycrystalline metallic films:

$$\frac{\kappa_{e,f}}{\kappa_{eq,b}} = \frac{\left(\varphi_e^{\,2} + 0.16\right)^{5/4}\left(\varphi_e^{\,2} + 0.44\right)\varphi_e}{\left(\varphi_e^{\,2} + 0.092\right)^{1/2}\left(\varphi_e^{\,2} + \eta\varphi_l\right)} \cdot \left[1 + \frac{3}{8\beta}(1-P) + \frac{7}{5}\alpha\right]^{-1} \qquad (67)$$

Where $\kappa_{eq,b}(T_l)$ is the bulk value that stays unvaried during non-equilibrium. For polycrystalline gold films with a smaller averaged grain diameter D, an increasing grain diameter parameter α results in an decreasing electron thermal conductivity, $\kappa_{e,f}$, thus signifying a less rigorous state of electron energy transport that also discourages electron thermal diffusion along both the z- and r-directions to reach the deeper and farther parts of the material. This explains the observations made with the temperature profile of the film with D=20nm whose maximum T_e is higher than the film with D=100nm in near-field, whereas lower T_e magnitude becomes even lower in the deeper region for the same reason.

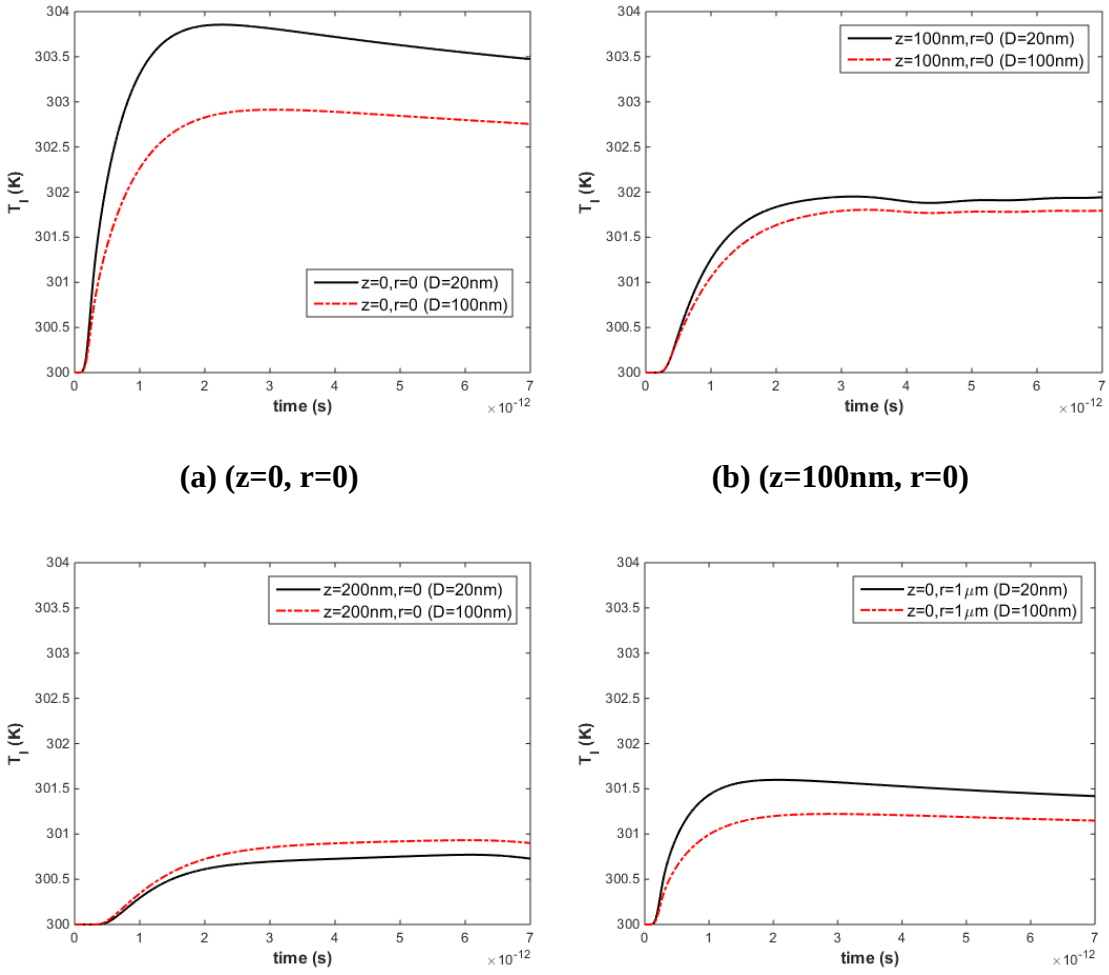

(a) (z=0, r=0) **(b) (z=100nm, r=0)**

(c) (z=200nm, r=0) **(d) (z=0, r=1μm)**

Figure 15. Temporal profiles of T_l for D=20nm and D=100nm at 4 different locations

The corresponding lattice temperature distributions are given in Figure 15. Except for Figure 15(b), all lattice temperature variations demonstrate the similar tendency as the electron temperatures observed in Figure 14 that higher electron temperature induces higher lattice temperature in the polycrystalline film. In Figure 15(b), the lattice

temperature of the film with D=20nm is higher than the film with D=100nm, while the electron temperature profile demonstrates a reverse development as shown in Figure 14(b). As previously discussed, electron-phonon interaction is the dominant parameter in lattice energy transport. Another important parameter that quantifies the energy exchange rate of electron-lattice collisions is the electron-phonon coupling factor as is indicated in Eq. (2),

$$\frac{G_f}{G_b} = \frac{\Lambda_b}{\Lambda_f} = 1 + \frac{3}{8\beta}(1-P) + \frac{7}{5}\alpha \tag{68}$$

Size effects are determined by parameters such as film thickness, averaged grain diameter, and the electron mean-free-path that defines the e-ph coupling factor G_f of polycrystalline metallic films of different microstructures. G_f for polycrystalline films is therefore not a constant. Variation of G_f due to distinct averaged grain size D therefore primarily attributes to the observation made with Figure 15(b). The electron-phonon coupling factor G_f defined in Eq. (68) accounts for the size effects of polycrystalline metallic films. With decreasing grain sizes, larger G_f values signify more energy exchange between the electron and lattice subsystems. This explains the reversal of T_l in films with D=20nm and D=100nm: more electron energies are effectively transferred into the lattice subsystem of the film of smaller grain size. The induced thermal stress gradient can be expected to be steep as a result.

4.2.4. Grain Size Effects on Stress Fields

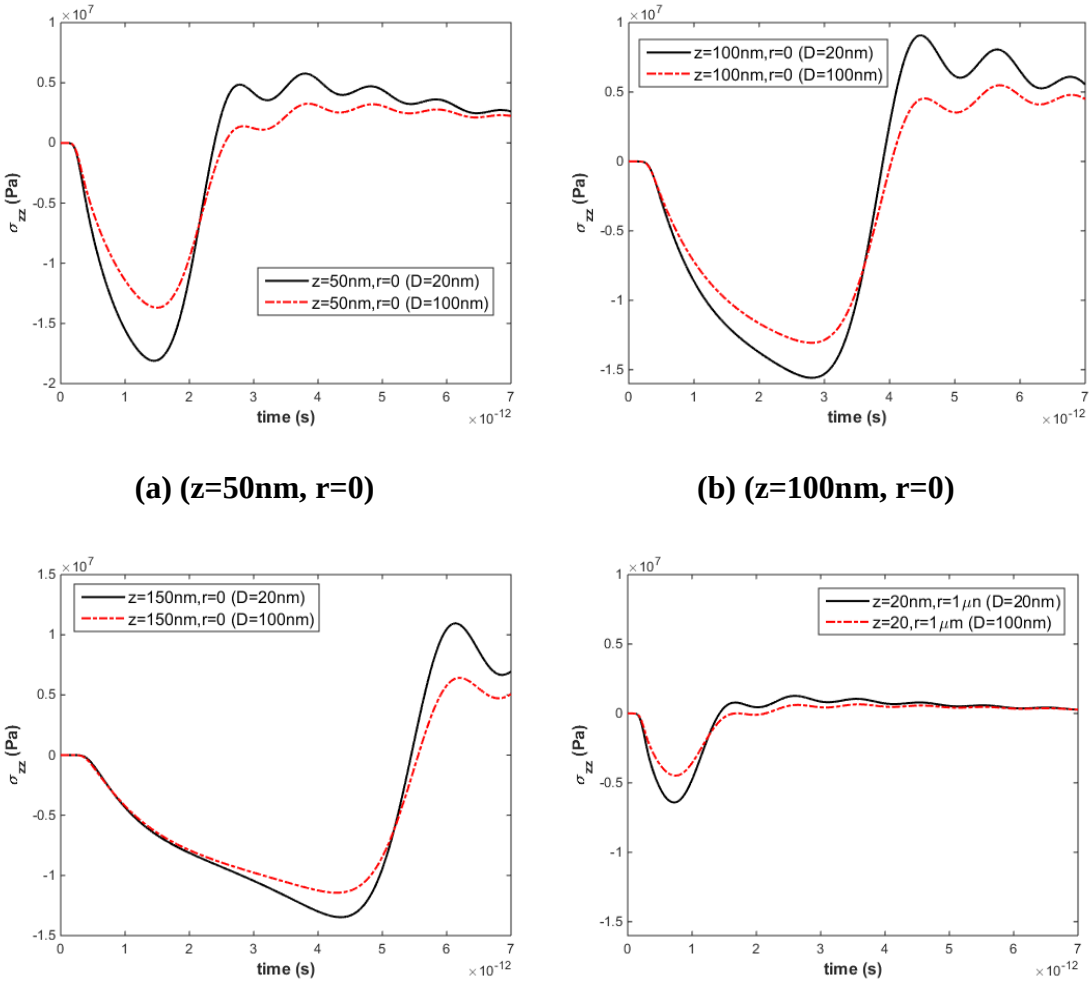

(a) (z=50nm, r=0) **(b) (z=100nm, r=0)**

(c) (z=150nm, r=0) **(d) (z=20nm, r=1μm)**

Figure 16. Temporal profiles of σ_{zz} corresponding to D=20nm and D=100nm at 4 different locations

Figure 16 exhibits the temporal evolutions of the normal stress component σ_{zz} in polycrystalline gold films with D=20nm and D=100nm. σ_{zz} are acquired at 4 locations at

(z=50nm, r=0), (z=100nm, r=0), (z=150nm, r=0), and (z=20nm, r=1μm). The first three locations are along the propagation path in the z-direction where r=0. As seen in the figure, the amplitudes of σ_{zz} are all relatively low, with the maximum value not exceeding 20 MPa and the highest peak being registered within the localized near-field where z < 150nm. Due to the size effect on thermal response and the ensuing thermal expansion, the stress responses along with their corresponding oscillation in the two polycrystalline films are consistently more intense with decreased averaged grain diameter. Identical observations can also be made with the other two normal stress components, σ_{rr} and $\sigma_{\theta\theta}$, and the shear stress component, σ_{rz}. Thus, the impact of size effects on both the thermal and mechanical field responses in polycrystalline metallic films is not negligible. The impact would be even more prominent when higher laser fluences are involved. Ignoring polycrystalline microstructure and the corresponding (grain) size effect would render the description of the elastodynamics of polycrystalline films incomplete.

4.3. Characteristics and Power Density of Thermo-Elastic Stress Waves

4.3.1. Thermal Stress Waves

Figure 16(a) - Figure 16(c) suggest features indicative of wave dispersion. Dispersion is characterized by attenuation in the time domain and time-evolving spectral response in the frequency domain. As much info pertaining to the generation and propagation of the thermal stress components can be extracted from the corresponding dispersion, Gabor Wavelet Transform (GWT) in Ref. [9] – [12] is employed. The waveforms acquired at Location 1 (z=50nm, r=0), Location 2 (z=100nm, r=0), and Location 3 (z=150nm, r=0) are processed using an in-house GWT program. Knowing that

when the averaged grain diameter is decreased, oscillations of both the normal and shear stresses become greater with a higher amplitude, only the σ_{zz} waves that correspond to D=20nm are resolved in the wavelet simultaneous time-frequency domain, as shown in Figure 17.

All σ_{zz}'s are characteristically broadband with extremely high frequency. Two frequencies, namely, $\omega_1 = 1.0\times10^{11}$ Hz and $\omega_2 = 2.5\times10^{11}$ Hz are followed to determine the corresponding group velocities of the stress components propagating from Locations 1 to 2 and from Locations 2 to 3, respectively. The group velocities tabulated in Table 2 and Table 3 show that both frequency components experience significant attenuation while propagating along the z-direction, thus substantiating that σ_{zz} is definitively dispersive.

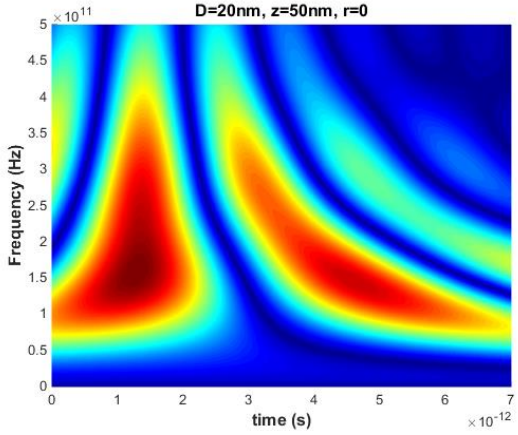

(a) (z=50nm, r=0)

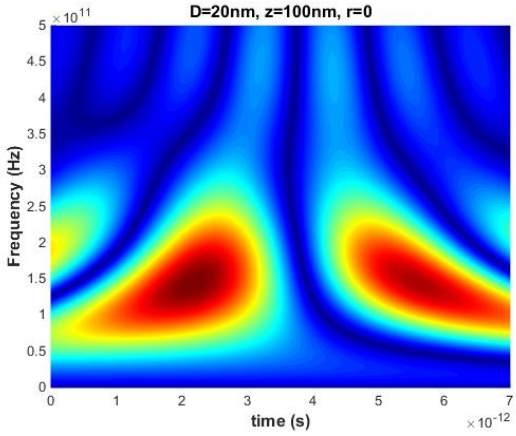

(b) (z=100nm, r=0)

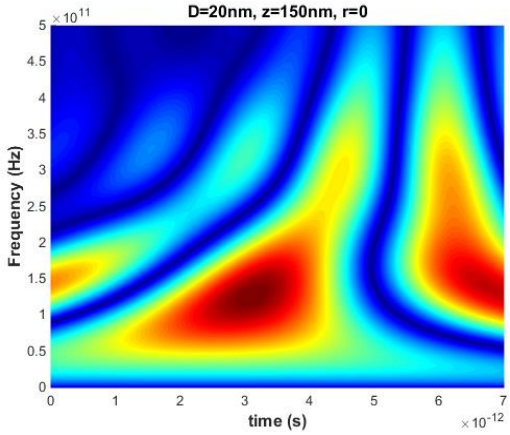

(c) (z=150nm, r=0)

Figure 17. GWT of σ_{zz} waves acquired at 3 consecutive locations

Table 2. Calculation of group velocity C_g for $\omega_1 = 1.0\times10^{11}$ Hz

Frequency ω1 (Hz)	Location z (nm)	Time of peak arrival (sec)	Δt (sec)	Group Velocity Cg (m/sec)
1.0×1011	50	0.798×10-12	0.934×10-12	5.3533×104
1.0×1011	100	1.732×10-12		
1.0×1011	150	2.896×10-12	1.254×10-12	3.9872×104

Table 3. Calculation of group velocity C_g for $\omega_2 = 2.5\times10^{11}$ Hz

Frequency ω_2 (Hz)	Location z (nm)	Time of peak arrival (sec)	Δt (sec)	Group Velocity C_g (m/sec)
2.5×10^{11}	50	3.140×10^{-12}	1.438×10^{-12}	3.4771×10^{4}
2.5×10^{11}	100	4.578×10^{-12}		
2.5×10^{11}	150	6.176×10^{-12}	1.598×10^{-12}	3.1289×10^{4}

As higher stresses were obtained in the film of small grain size, a question is being raised over if physical damage would be probable in the film with D=20nm subjected to the given optical input parameters? Figure 18 shows the spatial distributions of the three normal stress components (σ_{zz}, σ_{rr} and $\sigma_{\theta\theta}$) and the shear stress component (σ_{rz}) at t=10ps and t=30ps. All 3 normal stress components complete at least a full oscillation cycle along the thickness direction, while σ_{rr}, $\sigma_{\theta\theta}$ and σ_{rz} are in compression in near-field along the

radial direction, yet to demonstrate features characteristic of a full-fledged wave. As shown in Figure 18 the normal stresses travel at first as compressive waves through the thickness, and then change their polarity to a tensile mode upon rebounding back from the film boundary at approximately t=30ps. The shear stress component does not reach the radial boundary within the same time window. The amplitude of σ_{rz} is of the order of several MPa, which is one-tenth of all the normal stresses'. Such a low stress level is deceiving as not being potent enough to activate dislocation or slipping along the grain boundaries in the polycrystalline film. Although of small stress amplitude, the broadband dispersive wave can be detrimental given its high frequency.

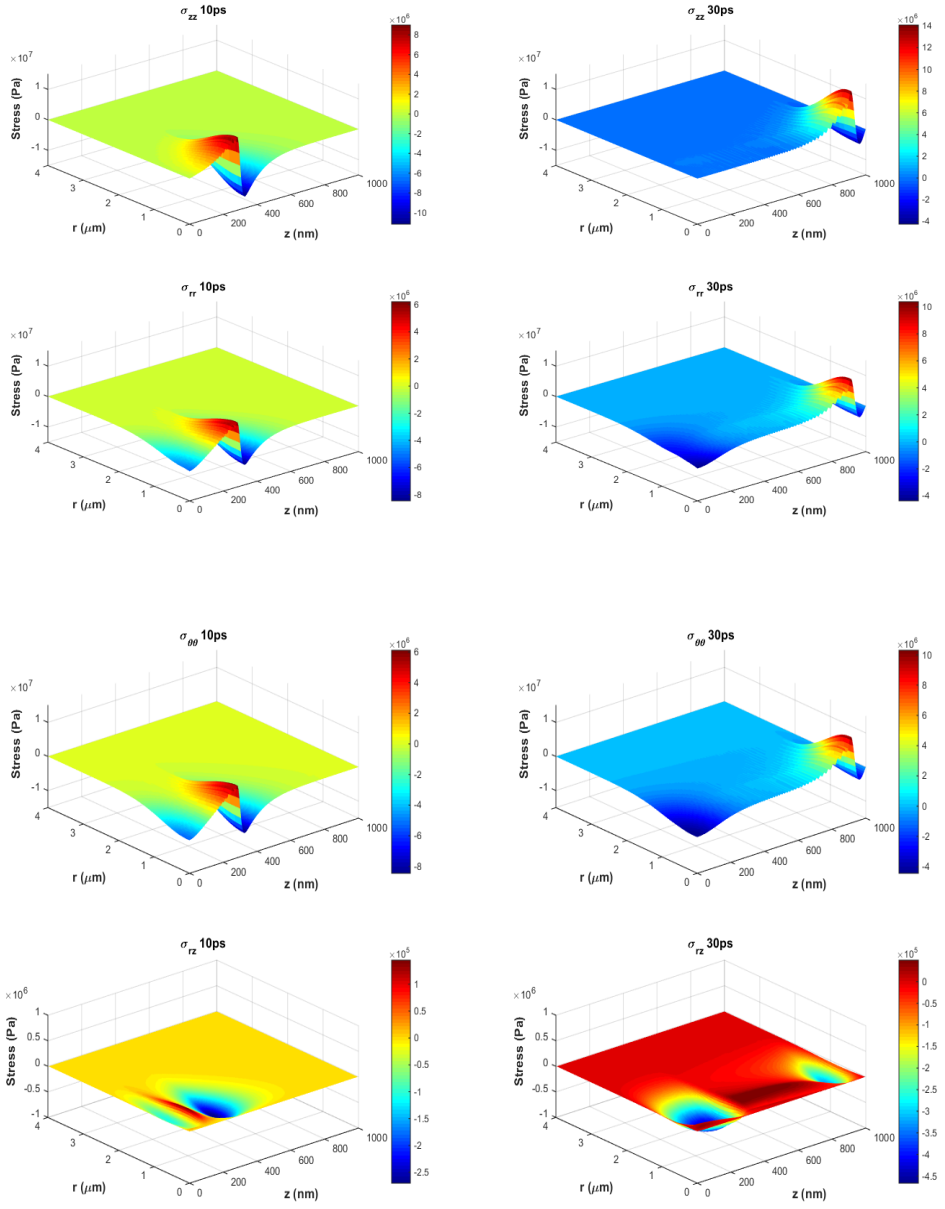

Figure 18. Spatial evolutions of stress components at 2 time instances for averaged grain size D= 20nm

4.3.2. Power Density

Short-time scale stress waves of low amplitude may not wreak imminent, large scale catastrophic failure, however, they could inflict microscale crack and defect should they carry high power density as in Refs. [3] – [5]. Power density as a fundamental concept was developed to characterize the various damage modes in microelectronic packages as fatigue cracking attributed to the propagation of dispersive thermal stress waves of extremely high frequency. The concept subsequently incorporated GWT time-frequency analysis for improved resolution for a wider range of frequencies in Ref. [13] and [14]. The time variation of an alternating stress, dS/dt, with S being the stress component, has an equivalent unit that can be obtained by considering the following SI units for stress and time as $\left[\frac{N}{m^2}\cdot\frac{1}{s}\right]\equiv\left[\frac{W}{m^3}\right]$. All stress variations in time to be considered in the section are interpreted using the equivalent unit that is called power density. Figure 19 presents the spatial distributions of the power density correspond to σ_{zz}, σ_{rr}, $\sigma_{\theta\theta}$ and σ_{rz} at t=30ps in the polycrystalline gold film with the averaged grain diameter D=20nm. All the power densities are seen to propagate in both the radial and thickness directions demonstrating specific features unlike their respective stress component counterparts. Albeit of low stress amplitude (< 20MPa), nevertheless, the magnitudes of the power densities are all extremely high, as much as 10^{18}-to-10^{19} W/m^3 in order of magnitude! Stress waves of high power density are more likely than not to initiate microscale cracks that raise the concern for high-cycle fatigue. Because $d\sigma_{zz}/dt$ comes with the highest magnitude, the power density of the stress component σ_{zz} is considered further as follows.

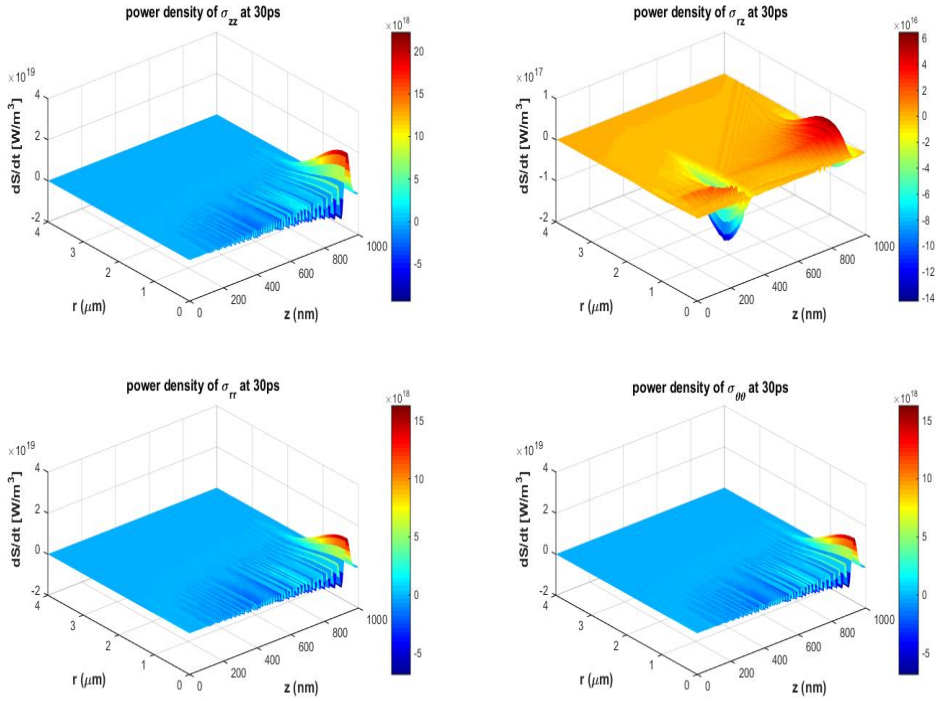

Figure 19. Spatial evolutions of power density (dS/dt) components at 2 time instances with averaged grain size D= 20nm

To establish some ideas as to where micro-cracks are most likely to initiate in the film in response to the ultrashort pulse irradiation, the σ_{zz} wave is extracted from six different locations at (z, r) = (50nm, 0), (400nm, 0), (800nm, 0), (50nm, 1µm), (400nm, 1µm) and (800nm, 1µm). The corresponding power densities are plotted in Figure 20. It is evident from the power densities established at (50nm, 0), (50nm, 1µm), (400nm, 0) and (400nm, 1µm) that the oscillation amplitude and frequency both decrease slightly over the 1µm radial range of propagation, thus indicating that the near-field response is

inconspicuous of being dispersive or attenuative. The corresponding GWT in Figure 21 says of the $d\sigma_{zz}/dt$ at (50nm, 0) as being broad in bandwidth and extremely high in frequency response (several hundreds GHz). These along with the fact that the maximum magnitude is registered at (50nm, 0) necessarily suggests that micro-cracking and dislocation slip are probable in non-melting heating in near-field.

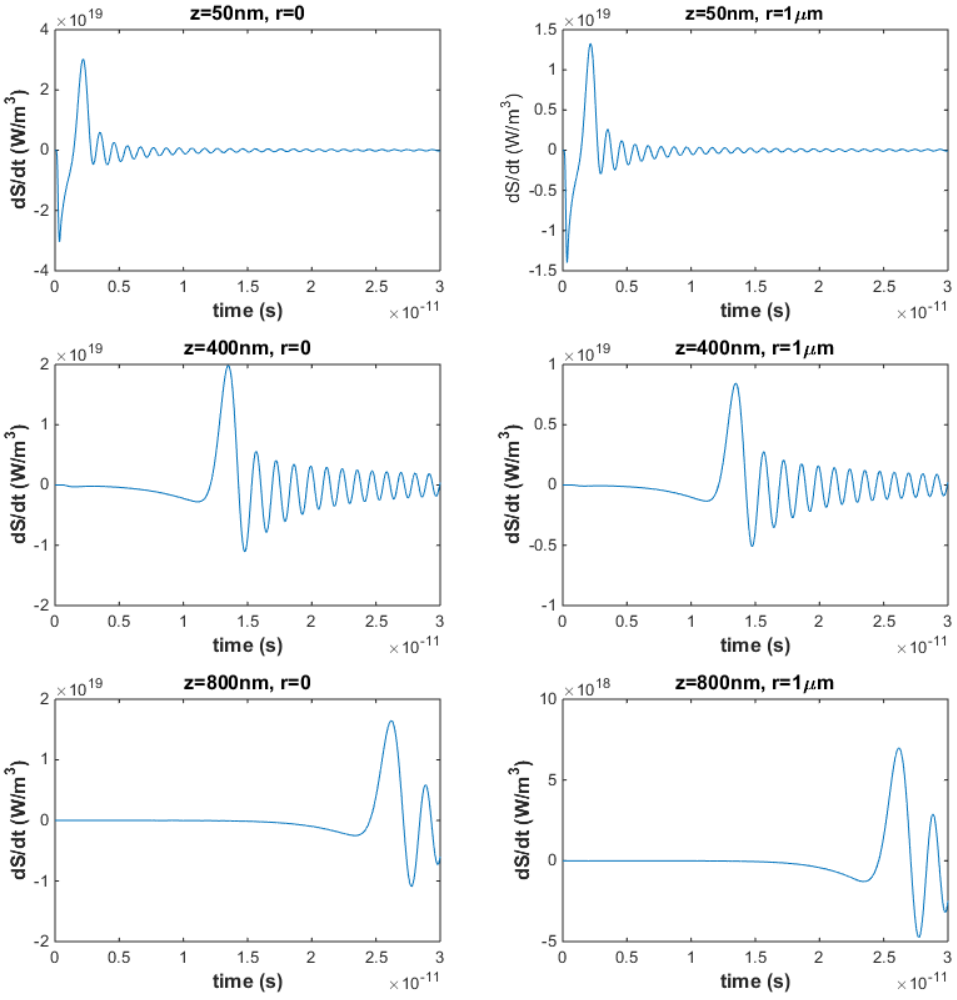

Figure 20. Temporal evolutions of power density dS/dt at six different locations

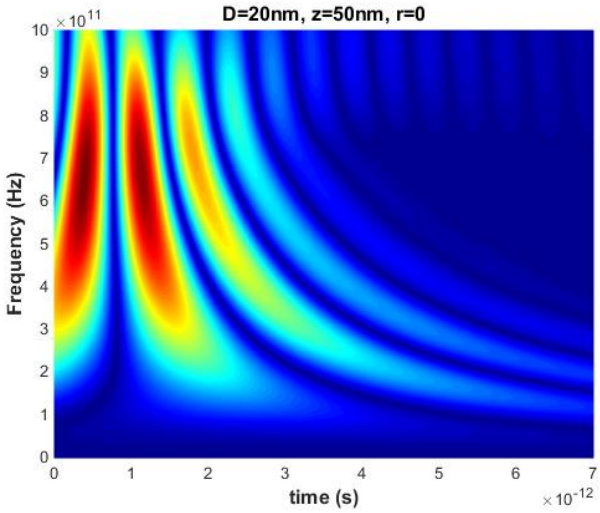

Figure 21. GWT of power density at location (z=50nm, r=0)

Drawing upon the understanding established pertaining to size effects and that the power densities calculated for the thermal stress waves are inherently high in frequency and dispersive with a broad time-varying spectrum, it can be deduced that the magnitude of dS/dt would be greater and the frequency even higher for polycrystalline metallic films having more grain boundaries and smaller grain sizes. In other words, fatigue cracking is more likely to be initiated in near-field with small grain sizes.

4.4. Summary

The three-dimensional thermo-elasto-dynamics was implemented using an axisymmetric model for the comprehensive description of the coupled thermal-mechanical behaviors induced by ultrashort laser pulse in a polycrystalline gold film. The optical input parameters that dictated radiation absorption and energy transport were correlated with the near-field responses generated by the rapid thermal expansion of lattices. Grain size effects on electron thermal conductivity and electron-phonon coupling factor were

studied to quantify the inconsistencies in the thermal stress waves generated in the film considering different averaged grain diameters. When smaller averaged grain diameters are considered, the electron and lattice temperatures in near-field were higher with a lower electron thermal conductivity and a larger electron-phonon coupling factor, indicating that electron energy was localized and the corresponding scattering attributed to the rapid ascending of temperature in near-field. Such dynamics had a profound impact on the mechanical field responses manifested as stress waves that were intensive and potentially damaging. These ultrafast laser-induced waves were found to be definitively dispersive and characteristically broad in bandwidth, low amplitude, and extremely high in frequency and power density. Near-field responses included short time scale thermal stress waves whose power densities were of the order of 10^{18}-to-10^{19} Watts per cubic meters [W/m^3]. It was shown that, despite of the non-melting heating, these waves of high power density were highly detrimental as they were potent enough to initiate fatigue cracking in near-field.

4.5. References

[1] Masaaki, S., Fukuda, N., Shimotsuma, Y., and Miura K., "Dynamics of interference of femtosecond laser-induced stress waves and crack formation inside a LiF single crystal," L*aser Applications in Microelectronic and Optoelectronic Manufacturing (LAMOM) XIX*, Vol. 8967, 2014, pp. 89670C.

[2] Masaaki, S., Ishiguro, Y., Shimotsuma, Y., Fukuda, N., and Miura, K., "Modulation of transient stress distributions for controlling femtosecond laser-induced cracks inside a single crystal." *Applied Physics A*, Vol. 114, No. 1, 2014, pp. 261-265.

[3] Oh, Y., Suh, C. S., and Sue, H.-J., "On failure mechanisms in flip chip assembly - part 1: short-time scale wave motion," *Journal of Electronic Packaging*, Vol. 130, No. 2, 2008, pp. 021008.

[4] Oh, Y., Suh, C. S., and Sue, H.-J., "On failure mechanisms in flip chip assembly - part 2: optimal underfill and interconnecting materials," *Journal of Electronic Packaging*, Vol. 130, No. 2, 2008, pp. 021009.

[5] Lin, Y., Liu, S., Zhao, X., Mao, E., Cao, C., and Suh, C. S., "Fatigue life prediction of engaging spur gears using power density," *Proc. IMechE Part C: Journal of Mechanical Engineering Science*, 2018, pp. 0954406217751557.

[6] Qiu, T. Q., Juhasz, T., Suarez, C., Bron, W. E., and Tien, C. L., "Femtosecond laser heating of multi-layer metals - II. experiments," *International Journal of Heat and Mass Transfer*, Vol. 37, No. 17, 1994, pp. 2799-2808.

[7] Qiu, T. Q., and Tien, C. L., "Size effects on nonequilibrium laser heating of metal films," *Journal of Heat Transfer*, Vol. 115, No. 4, 1993, pp. 842-847.

[8] Mayadas, A. F., and Shatzkes, M., "Electrical-resistivity model for polycrystalline films: the case of arbitrary reflection at external surfaces," *Physical Review B*, Vol. 1, No. 4, 1970, pp. 1382.

[9] Kishimoto, K., Inoue, H., Hamada, M., and Shibuya, T., "Time frequency analysis of dispersive waves by means of wavelet transform," *Journal of Applied Mechanics*, Vol. 62, No. 4, 1995, pp. 841-846.

[10] Rabroker, G. A., Suh, C. S., and Chona, R., "Laser-induced stress wave thermometry applied to silicon wafer processing: modeling and experimentation," *Experimental Mechanics*, Vol. 45, No. 1, 2005, pp. 3-8.

[11] Vedantham, V., Suh, C. S., and Chona, R., "Laser induced stress wave thermometry for in-situ temperature and thickness characterization of single crystalline silicon wafer: part I - theory and apparatus," *Experimental Mechanics*, Vol. 51, No. 7, 2011, pp. 1103-1114.

[12] Vedantham, V., Suh, C. S., and Chona, R., "Laser induced stress wave thermometry for in-situ temperature and thickness characterization of single crystalline silicon wafer: part II - experimental results," *Experimental Mechanics*, Vol. 51, No. 7, 2011, pp. 1115-1122.

[13] Qi, X., and Suh, C. S., "Ultrafast laser-induced elastodynamics in single crystalline silicon part II: near-field response," *Journal of Thermal Stresses*, Vol. 32, No. 5, 2009, pp. 494-511.

[14] Qi, X., and Suh, C. S., "Generalized thermo-elastodynamics for semiconductor material subject to ultrafast laser heating. Part II: near-field response and damage evaluation," *International Journal of Heat and Mass Transfer*, Vol. 53, No. 4, 2010, pp. 744-752.

5. THERMO-ELASTO-PLASTO-DYNAMICS OF ULTRAFAST LASER ABLATION IN POLYCRYSTALLINE METALS

5.1. Introduction

Many studies have been given to understanding ultrafast pulse induced ablation. However, a comprehensive description of the inherent ablation mechanism remains elusive for the reason that laser-material interaction is a strong function of many parameters including laser intensity, pulse duration, optical wavelength, material properties, and sample geometry. Ultrafast laser ablation is a process involving the use of high excitation that creates either heterogeneous or homogeneous nucleations. When the ultrafast pulse applied is close to the threshold of melting, the irradiated target suffers a rapid phase transition described as heterogeneous nucleation in which the liquid layer is nucleated at the solid-vapor interface and the melting layer recedes into the bulk with a receding velocity [4] – [6]. Phase transition is often described by rapid melting, vaporization, and re-solidification – all characterized by lattice temperature exceeding material's melting point and saturation temperature [2]. At a sufficiently high excitation, the material is superheated at a time scale smaller than the one that dictates heterogeneous melting. This is known as homogeneous nucleation [5]. It leads to the formation of a liquid-gas mixture in target material due to superheating and lattice instability. One approach argues that material ejection via phase explosion is dominated by spallation as a result of stress-induced void coalesce [7] while others emphasize the role of evaporation and ablation recoil pressure as the culprits for the ejection of larger liquid droplets from

the melt surface [8] and [9]. Hydrodynamic model and molecular dynamics (MD) are often employed to describe the early-stage plasma plume dynamics observed during ablation [3].

Surface morphology by ultrafast laser processing, however, does not always involve material removal through phase transition or explosion. A function of laser fluence, ultrafast ablation can involve submelting, melting, and superheating [1]. It was found in a study on ablating a Cu material using a subpicosecond laser (500fs) that when the fluence F was between 0.4 J/cm^2 and 5 J/cm^2, a thin molten layer appeared. The mechanism involved was the melt ejection due to the recoil pressure of the plasma [4]. With the use of pump-probe technology, a similar melting process was observed in Si that was irradiated by a femtosecond laser of high laser fluence [10]. When F > 5 J/cm^2, ejection of large liquid droplets was observed. A probable interpretation is that phase explosion superheated the target (lattice temperature is assumed to be above the critical temperature) and explosive decomposition dictated the material [1], [4] and [11]. Ablation at F < 0.4 J/cm^2 was observed with no indication of molten layers. This necessarily excludes phase transition or boiling explosion because lattice temperature does not exceed the melting temperature. Thus, the material removal process by ultrafast laser heating with relatively low fluence cannot be explained by phase transition or explosion. Formation of optical interference patterns and disappearance of Newton rings also indicate the role of mechanical deformation during the ablation process involving low fluence [12]. Investigations on machining quality using femtosecond lasers also concluded the same – that no molten debris were found in the ablated area morphology involving low laser

fluence [13]. And the resulted material ejection was mainly caused by the spallation of the fractured layers as a result of the induced stress alternating to the tensile mode [14]. Hence, when relatively low fluence (near the threshold of ablation) is employed, ablation is primarily attributed to thermally induced mechanical damage with fragmentation ejection (photomechanical spallation) being the mechanisms for material removal. Thermal-mechanical disturbance is believed to be the root cause for the incubation effect [15] and ripples [16] – [18] by single- or multi-laser shots at low fluence. A comprehensive understanding for laser-material interaction, thermally induced mechanical response, and fragmentation ejection and spallation is required to describe femtosecond ablation at light intensity and the induced surface morphology.

Material removal through ablation by light laser intensity irradiation generates interesting coupled thermal-mechanical effects. Not knowing how light intensity lasers would ablate materials, experiments on surface patterning in submelting condition were not able to be conducted [19]. And, experimentally observed cracking in irradiated materials cannot be properly explained by models of high laser intensity [20]. Ultrafast laser ablation has been investigated using molecular dynamics (MD). Ejection of molecules and clusters [25] and surface explosion of monolayers were derived by considering the dynamics of individual molecules and liquid droplets [4]. MD, however, is not a tool of choice for studying coupled thermal-mechanical responses on a macroscopic scale because of the forbidding need for computational resources. In addition, it is a daunting task attempting to model both the thermal and mechanical

responses using MD for a few picoseconds, which is essential to studying thermo-elasto-plastodynamics on a macroscopic scale.

Two-temperature model has its inherent advantage in macroscopically describing the energy transport dynamics for both electron and lattice subsystems. The model is supported by physical data and shown to be viable for depicting the dynamics of material response involving ultrafast laser heating with a wide range of high laser intensity. Many have contributed to improving ultrafast dynamics with the use of the two-temperature model [3], [8], [19], [21], [23], [31], [42]-[47] and [55]. However, a comprehensive ablation model is yet to be available - one that describes ultrafast heating dynamics as a physical process involving electron (ion) emission, plasma formation and plume expansion, current density in and coupled thermo-elaso-plastic behaviors of the material. The implications for having such a model are many including providing the knowledge needed to control fatigue fracture and fragmentation ejection.

Ultrashort pulsed laser irradiation is a complex process of multi-physics following several consecutive stages including laser absorption, thermal diffusion, plasma formation and expansion, electron-lattice energy exchange, coupled thermo-elasto-plastic dynamics, and ejection. The dynamics is incomplete without considering both electron transport and thermomechanical coupling. Obeying the law of conservation of energy and following the inherent time scale of each of the consecutive stage are essential to establishing the mechanism that dictates non-thermal heating and low intensity ablation. A dynamic model would not be considered feasible if the physical time scale fundamental to the complex thermo-elasto-plastodynamic process is not precisely followed.

When irradiated by femtosecond pulses, hot electrons are released through photoexcitation into a 'free-electron gas' with a velocity approaching the Fermi velocity [7] and [11]. Rigorous electron-electron collisions instantaneously occur in this energetic electron subsystem when these highly excited electrons approach the Fermi energy. Once the electron gas is thermalized after a few femtoseconds, the temperature of the electrons can be used to describe the dynamics of the electron subsystem. During and after the thermalization, excited electrons emit from the target surface with a time scale that is a few tenths of a picosecond [21]. Electrons emit from the target into the ambient by overcoming the potential barriers and induce ion ejections due to the double layer effect and the ensuing plasma formation. Though the temperature of the ions in the lattice subsystem is initially cold, however, transfer of energy from phonons to electrons gives rise to rapid lattice temperature increase in a matter of a few picoseconds. Since melting is improbable in the sub-melting condition involving low laser fluence, lattice temperatures therefore in the ablated region cannot exceed the melting temperature.

When a laser fluence set near at the ablation threshold is applied, lattice temperatures are elevated to a point that is far below the melting temperature. The high temperature gradient, however, results in rapid thermal expansion and high thermal strain rate in the region that is optically struck upon. Eventually, the induced mechanical stress exceeds the elastic limit, causing dislocation motion that is as the onset of plasticity [19], [24] and [26]. The material behaves elasto-plastically with the increase of plastic strain and eventually fractures from nucleation, crack growth or void coalesce. As the thermal stress alternates and violates certain energy criteria, spallation occurs along with a large

scale of fragmentation and ejection of fractured layers. Thermo-elasto-plastic dynamics plays a significant role in describing not only material behaviors but also providing the criteria for fracture and fragment ejection needed to characterize permanent deformation and depth of ablation. While the thermo-elasto-plastodynamic responses to ultrafast heating is understood for single-crystalline silicon substrates [22] and [23], similar studies on polycrystalline materials for their responses to ablation are few and incomplete. Lacking a comprehensive understanding for the ultrafast laser-material interaction under the sub-melting condition is hindering the facilitation of ultrafast lasers as a technology of choice for surface modification and direct laser deposition (DLD), for example. And, very few studies if none at all provide a thorough description following the time scale that characterizes the ultrafast heating process. The present chapter addresses the need for a comprehensive understanding for the underlying mechanism that dictates the laser-material interaction and ablation process induced by low fluence ultrafast input.

5.2. Hot Carrier Emission

Ionization and free-electrons (ions) emission in the form of dense plasma were observed during and after the impinging of a femtosecond laser pulse [8] and [27]. As the emitted hot electrons are of high kinetic energy, they ionize the ambient air and produce plasma plume as a reult. The ejection of hot electrons/ions dissipates a large amount of energy during the intensively competing process of energy generation by absorption and diffusion by electron-electron collisions. The principle of energy conservation demands that electrons emission and their impact on the dissipation of the electron subsystem not

be neglected when describing the electron and thermal and mechanical energy transport initiated by ultrafast laser irradiation.

5.2.1. Electron Emission

Multiphoton photoemission, or photoelectric effect, is the primary dynamics for electron emission. When photoelectrical ionization occurs on the material surface exposed to an ultrafast laser beam when the surface layer with a depth on the order of nanometers receives enough optical energy. The photoelectrons are emitted from the surface when the absorbed energy exceeds the characteristic binding energy of the molecular bond and produces free electrons of high kinetic energy. Electrons are emitted from the target surface through two mechanisms: multiphoton photoemission and thermionic emission. The process induces subsequent air-breakdown and subsides eventually after a few picoseconds [21]. Lasting up to hundreds of femtoseconds, electrons emission is experimentally reported to be predominated by photoemission [28], and the onset of multiphoton photoemission occurs prior to thermionic emission [27]. Thermionic emission is the non-equilibrium heating of electrons that imparts the electrons with temperature-dependency [29]. Caused by the electron thermal relaxation taking place on a picosecond time scale [30], thermionic emission occurs when charged carriers acquire enough thermal energy to overcome the work function of the target material. Thermionic effect was observed to be greater than the competing photoelectric effect on a picosecond time scale [27]. Decreasing in optical wavelength is seen to increase the thermionic effect as an alternative hot electron emission. The onset of thermal electron emission is found

to be delayed and lagged behind multiphoton photoemission due to the thermal relaxation time.

5.2.2. Ion Emission Mechanism

In response to laser energy absorption, ionization and free-electron emission result in ions being rapidly emitted from the irradiated surface. It remains controversial as to the dominant mechanism that governs ion emission. Thermion and non-thermal emission are known as the two competing mechanisms in describing ion emission [3]. In non-thermal emission, electrons are emitted in the local region of the irradiated surface via the photoelectric effect. The positive charges being accumulated as a result of the rigorous emission generate a strong electrostatic field that expels positive charges from the surface layer when the covalence bonds between the ions are severed. This kind of ion emission process is known as Coulomb explosion. The non-thermal process would take place when the generated electric field is greater than the Coulomb explosion threshold at several 10^8 V/cm. Otherwise Coulomb explosion would be absent from the ablation process [3], [7] and [8]. Thermionic emission takes place on a picosecond scale characterized by thermal relaxation time. It has been observed in experiments that ions thermal emission or thermally enhanced photoemission become dominant at high laser intensity [29], thus indicating that thermal emission is strongly temperature dependent. However, at light laser intensity, the probability for the thermal emission of ions to occur is low given that the temperature involved is significantly lower. It should be noted that Coulomb explosion or other multiphoton photoemissions is inhibited in metals due to the screening effect in which the residual electrons of high mobility effectively neutralize the positive charges

generated by the electron emission in the surface layers [31]. Nevertheless, experimental observations seem to support that Coulomb explosion can take place in the irradiated surface subject to relatively low laser intensity [32] and [33]. The debate over the dominant ion emission mechanism gives rise to the investigation of the resulted electric field, which is the gauging criteria for the occurrence of Coulomb explosion.

5.3. Thermo-Elasto-Plasto-Dynamics

When the intensity of the ultrashort laser pulse is sufficiently high or close to the ablation threshold, the induced response is no longer elastic. The irradiated material would experience plastic flow and hardening as it yields and deforms irreversibly. Tension-compression alternation, referred to as cyclic loading, is characteristic of the thermo-elastodynamic response to ultrafast laser heating involving low fluence. The rapid expansion and contraction of the lattices give rise to high frequency propagating stress waves that are potent in inflciting micro cracking and fatigue failure. A proper description of such characteristic cyclic behaviors requires the study of thermo-elasto-plasto dynamics. Isotropic hardening and kinematic hardening are popular for describing the plastic deformation under cyclic loading. In isotropic hardening, the yielding surface is affine and expanded uniformly in all directions following a von Mises-type yielding criterion [34]. However, isotropic hardening fails to represent the Bauschinger effect often observed in metals subject to cyclic loading. Kinematic hardening on the other hand addresses the Bauschinger effect in the uniaxial loading of polycrystalline metals [35] and [65].

While considering the Bauschinger effect, however, linear kinematic hardening model is deficient in producing accumulated plastic stress [35]. Further modifications were made to consider both strain hardening and dynamic recovery for pastic stress accumulation. One of the nonlinear kinematic hardening rules shown to represent well the stress-strain hysteresis loop under cyclic loading [36] is the Armstrong-Frederick (AF) model [66]. Applicable to polycrystalline metals under cyclic loading, the model considers the Bauschinger's effect and incorporates strain hardening with the evolution history of the backstress [38]. The nonlinear AF kinematic hardening model is widely adopted by commercial packages for real-world applications [37] – [39]. Modifications to the model are available including decomposing backstress into several independent components to allow for each component to be individually evolved following the AF hardening rule and improving the tracing of hysteresis curve [40] and [41]. The Armstrong-Frederick model is adopted in the current study to characterize the cyclic thermal plasticity induced by ultrafast laser pulse of low laser intensity.

5.4. Electronic Transport Dynamics

The ultrafast laser induced dynamics of carrier emission and the accompanying effect on the energy transport of electrons are considered in the followings. A model based on the ambipolar diffusion [42] was employed to describe the carrier dynamics in single crystalline semiconductor materials where the flow of electrons was explained using a relaxation-time approximation of the Boltzmann equation [43]. The electron subsystem is not conservative and the carrier dynamics is incomplete without considering electrical

and energy currents in energy transport. As indicated in [44] where a self-consistent model was shown to correlate well with physical data, carrier dynamics is non-negligible.

Unlike in semiconductors, free electrons within the limited control volume in metals can be viewed as if infinite, thus negligible carrier flow. However, electron emission causes an intense transport of electrons from the bulk to the target surface in the form of an electric flux, evoking the formation of an intense electric current that subsequently induces the ion dynamics. The associated carrier dynamics and its effect on energy transport are prominent due to the large number of emitted electrons and the high mobility of the carriers. Consequently the transport of electrons and ions and the corresponding impact on the material must be considered. Or else the electron temperature, which is representative of the thermalized free-electron gas induced by the ultrafast laser pulse, would be overestimated and the electron-lattice interaction that follows be misinterpreted. The aforementioned self-consistent model and its variations [42], [44] – [46] are not applicable to describing the dynamics of surface emission because they do not consider the transport of electrons and ions as the mechanism of emission.

Of the many articles on modeling ultrafast laser heating employing the two-temperature model, hydrodynamic formulations, or molecular dynamics plenty, only a handful few are on the surface emission induced by ultrafast laser pulses and the associated electric transport. As electron transport dynamics and the corresponding effect on the transport of energy are nonnegligible, a self-consistent description of the generation of the electric field was proposed [3], [8] and [31] which includes the drift and diffusion of the carriers induced by ultrafast laser pulsing. The drift-diffusion description found in Ref.

[8] is revised in the study by considering the physics of multiphoton photoemission and the electric continuity equations are modified to address photoelectric and thermionic emissions and the result electric field. The revision is used in the following sections to evaluate the contribution made by two- and three- photon photoemissions, to determine the dominant emission mechanism, and to establish the condition of Coulomb explosion.

5.4.1. Surface Emission Rate

The target material being considered in the section has its irradiated face located at z=0 where a laser beam is applied. Upon the illumination of the laser pulse, electrons of high kinetic energy break away from the potential energy barrier and subsequently escape from the target surface via multiphoton photoemission and thermionic emission. The emission process is accompanied by an intense electron flux. At z=0, the total surface emission rate j_t is the sum of both the multiphoton photoemission rate, $\sum_{N=1}^{\infty} j_N$, and the thermionic emission rate, j_{th},

$$j_t = j_{th} + \sum_{N=1}^{\infty} j_N \tag{69}$$

Thermal emission of the high-temperature electrons is prominent at the picosecond scale at which the increase of electron temperature is significant [47]. Thermal contribution to the ejected electron flux (the thermionic emission rate, j_{th}) is considered in the following Richardson-Duschman equation,

$$j_{th} = A_0 T_{es}^2 \exp\left(-\frac{\varphi}{k_B T_{es}}\right) \tag{70}$$

where the theoretical Richardson coefficient A_0 =120 A/(cm^{2}K^2), T_{es} is the electron temperature on the target surface, the work function φ = 4.25 eV is the barrier height of electrons.

As mentioned, two different mechanisms of electron emission are present subject to ultrashort pulsed laser irradiation. In photoelectric photoemission electrons in the conduction band each absorb one or more photons to overcome the barrier height for electron promotion. The rate of photoelectric emission is defined by the generalized Fowler-DuBridge theory where the photoemission cross-section temperature-dependent [8],

$$j_N = a_N \left(\frac{q}{\hbar \nu} \right)^N A_0 I_0^N \left(1-R\right)^N T_{es}^2 \cdot F\left(\frac{N\hbar\nu - \varphi}{k_B T_{es}} \right) \tag{71}$$

where I_0 is the incident laser beam intensity, the reflectivity I =0.949 per the experiment reported in [47]. The term $\left(1-R\right) I_0$ represents the absorbed fraction of the incident laser intensity [50]. $\hbar\nu$ is the photon energy, a_N is the material dependent constant associated with N -photon photoemission. $F\left(x_N\right)$ is the Fowler function with $x_N = \left(N\hbar\nu - \varphi\right)/k_B T_{es}$.

The photon energy is calculated using $\hbar\nu = \hbar c/\lambda$, with $\hbar$ being the Planck constant, 6.626×10^{-34}J.s and c= 3.0×10^8 m/s being the speed of light. The wavelength λ is selected as 800nm for the study. The photon energy needed to overcome the potential barrier to release an electron into the vacuum is calculated to be 1.55 eV.

5.4.2. Fowler Function

The Fowler function is a power series [48] and [49] as follows

$$F\left(x_N\right)=\int_0^{\infty} dy \ln\left(1+e^{-(y+x_N)}\right)$$
$$=\begin{cases}\sum_1^{\infty}(-1)^{n+1}\dfrac{e^{nx_N}}{n^2} & x_N<0\\ \dfrac{\pi^2}{12} & x_N=0\\ \dfrac{\pi^2}{6}+\dfrac{x_N^2}{2}-\sum_1^{\infty}(-1)^{n+1}\dfrac{e^{-nx_N}}{n^2} & x_N>0\end{cases} \tag{72}$$

where $x_N=\left(N\hbar\nu-\varphi\right)/k_BT_{es}$. Figure 22(a) plots the Fowler function $F\left(x_N\right)$. When $N=0$ the Fowler-DuBridge expression in for electric current density is reduced to the Richardson equation mentioned previsouly with the term j_N being equivalent to the electrical current density due to thermionic emission. Thus Eq. (71) can be simplified to Eq. (70) when $N=0$ [52].

Three-photon photoemission is the dominant process of nonlinear multiphoton emission that dominates the generation of electric current density in gold materias. While it is indisputable that the three-photon energy considered in the work, which is $3\hbar\nu$ =4.65 eV, is above the photoemission threshold for overcoming the work function (φ = 4.25 eV), however, some would still argue that the thermally assisted multiphoton photoemission is probable in the nonlinear process of photoemission where a certain amount of ejected electrons are attributed to the high-energy tail of the Fermi-Dirac distribution when $\left(N\hbar\nu-\varphi\right)<0$ [49]. This means that two-photon photoemission is enabled by thermalization and the high electron temperature resulted from rigorous electron-electron collisions. Considering the thermally assisted two-photon photoemission, the

electrical current density due to the two-photon emission is calculated with respect to the surface electron temperature, T_{es}. Figure 22(b) provides a comparison of the resulted Fowler functions associated with the two- and three-photon emissions. It is found that the two-photon emission and the resulted emission rate is negligible when the surface electron temperature is below 5000 K. However, as T_{es} increases, photoelectrical emission is suppressed and decreases sharply. Eventually the Fowler function that corresponds to the thermally assisted two-photon emission becomes comparable with the predominant three-photon emission after the electron temperature exceeds 5000 K. Incorporating both the two- and three-photon photoemissions for the determination of the total electrical current density whenever and wherever high electron temperatures are involved is necessary.

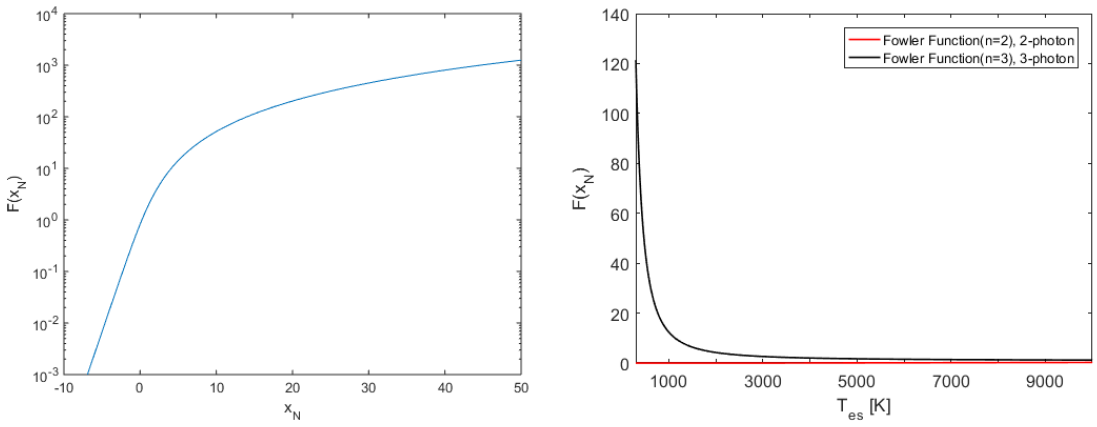

(a). Fowler Function as a function of x_N **(b). Fowler Function as a function of T_{es}**

Figure 22. Fowler function $F(x_N)$

The total electrical current density of the electrons emitted from the target surface is summarized in the followings that considers both the thermionic and photoelectric components,

$$\begin{aligned} j_t &= A_0 T_{es}^2 \exp\left(-\frac{\varphi}{k_B T_{es}}\right) \\ &+ a_2 \left(\frac{q}{\hbar\nu}\right)^2 A_0 {I_0}^2 (1-R)^2 T_{es}^2 \cdot F\left(\frac{2\hbar\nu-\varphi}{k_B T_{es}}\right) \\ &+ a_3 \left(\frac{q}{\hbar\nu}\right)^3 A_0 {I_0}^3 (1-R)^3 T_{es}^2 \cdot F\left(\frac{3\hbar\nu-\varphi}{k_B T_{es}}\right) \end{aligned} \tag{73}$$

where a_2 and a_3 are material-dependent constants associated with the two- and three-photon photoemissions, respectively. These parameters are determined by considering transition matrix elements and the escape probability of the electrons. For gold materials, these two parameters are empirically approximated from experimental data: $a_2 = 4\times10^{-23}$ cm^4/A^2 [53] and $a_3 = 10^{-33}$ cm^6/A^3 [54]. Eq. (73) calculates the surface emission rate describing the electron flow into the ambient due to the surface emission and is applied as the boundary condition for the generated electron dynamics at the surface in Eq. (75).

5.4.3. Electrical Current inside Target

The basic continuity equations for the evolution of the laser-generated charge carriers (electrons and ions) transport is [42]:

$$\frac{\partial n_x}{\partial t} + \frac{1}{e}\frac{\partial j_x}{\partial x} = G + R \tag{74}$$

where n_x represents the carrier density, j_x is the electrical current densityin the target, G and R denote the carrier generation and decay rates, respectively. For metals, the G and

R in Eq. (74) are assumed to be 0 [31] and [47], resulting in the following transport equations for electrons and ions generated in the target material,

$$\frac{\partial n_e}{\partial t} - \frac{1}{q}\frac{\partial j_e}{\partial x} = 0$$
$$\frac{\partial n_i}{\partial t} + \frac{1}{q}\frac{\partial j_i}{\partial x} = 0 \tag{75}$$

where n_e and n_i are the number density of the free electrons and ions, respectively, q is the magnitude of the electron charge, j_e and j_i are the electric current density of the electrons and ions, respectively.

Considering the carrier transport dynamics involving both drift and diffusion due to the generated electric field and carrier density gradient, the corresponding electrical current densities of the electron and ions are

$$j_e = qn_e\mu_e E + qD_e\frac{\partial n_e}{\partial x}$$
$$j_i = qn_i\mu_i E - qD_i\frac{\partial n_i}{\partial x} \tag{76}$$

where E is the electric field initiated by the surface emission, μ_e = 5.17×10^{-3} (m^{2}V^{-1}s^{-1}) and μ_i = 5.17×10^{-3} (m^{2}V^{-1}s^{-1}) are the mobility of the electrons and ions, respectively [47], D_e and D_i are the diffusion coefficients of electrons and ions given by

$$D_e = \mu_e k_B T_e / q$$
$$D_i = \mu_i k_B T_l / q \tag{77}$$

where k_B = 1.38064852×10^{-23} JK^{-1} is the Boltzmann constant with T_e and T_l denoting the electron and lattice temperature, respectively.

The electric field in the target is determined through the Poisson equations derived from incorporating the local breaking of quasi-neutrality,

$$\frac{\partial E}{\partial x} = \frac{q}{\varepsilon \varepsilon_0}\left(n_i - n_e\right) \tag{78}$$

with ε = 1.0 being the relative permittivity of the target material [31] and the vacuum permittivity of the target material being $\varepsilon_0 = 8.85\times10^{-12}$ C/(Vm).

5.5. Energy Balance Equations

5.5.1. Electron Energy Balance Equations

The total balance equation for the generated carrier energy is as follows [42], [45] and [46],

$$\frac{\partial U}{\partial t} + \nabla \cdot W = S_U - L_U \tag{79}$$

where U represents the carrier energy, W is the total energy current derived from the electrical current density of the carriers, S_U is the absorption of optical energy, and L_U represents the kinetic energy loss to electron-lattice interaction. Considering the description of energy transport equation in terms of electron temperature, the electron energy balance equation in Eq. (79) is revised in the followings to 1) incorporate the dissipation of energy current W caused by the electron emission and 2) admit the hyperbolic nature of the electron energy transport with a finite propagating speed,,

$$\begin{aligned} C_e\left(\frac{\partial T_e}{\partial t} + \frac{j_e}{q n_e}\frac{\partial T_e}{\partial z}\right) &= -\nabla \cdot q_e - G\left(T_e - T_l\right) + S\left(z,t\right) \\ \tau_e \frac{\partial q_e}{\partial t} + q_e &= -\kappa_e \nabla T_e \end{aligned} \tag{80}$$

where the electron transport equation is embodied by a hyperbolic heat flux equation with the relaxation time of free electrons, τ_e, and q_e is the electron heat flux. The electron energy current is function of the electrical current density j_e coupled with the electron density n_e and electron temperature T_e [8], [31] and [47]. The source term $S(z,t)$ is derived from the temporal and spatial profiles of the laser intensity absorption, and $L_U = G(T_e - T_l)$ is the energy loss term. Material property C_e is the electron heat capacity, κ_e is the electron thermal conductivity, and G is the electron-phonon coupling factor.

5.5.2. Lattice Energy Balance Equations

The hyperbolic nature of the lattice energy transport is imparted by the presence of the thermal relaxation time of the lattice, τ_l, [55], thus rendering finite thermal propagating speed. Thermal-mechanical coupling is non-negligibly essential to describing the entire energy transport in the quasi- and near-equilibrium states [45], [46], [56] and [56]. Ignoring the energy dissipated to initiating thermoelasticity would inevitably lead to higher lattice temperature. This is particularly so when the laser fluence is greater than the ablation threshold. Also the frequency response of the thermally induced stress rate would be falsely interpreted if the thermoelastic damping due to the onset of plasticity is not considered [57], thus obscuring the rate-dependent stress field and the energy transport dynamics of the lattice system. As thermo-mechanical coupling is crtitical to understanding ablation-induced surface morphology, the following energy balance equations of the lattice incorporate an energy exchange term, L_M,

$$C_l \frac{\partial T_l}{\partial t} = -\nabla \cdot q_l + G\left(T_e - T_l\right) - L_M$$

$$\tau_l \frac{\partial q_l}{\partial t} + q_l = -\kappa_l \nabla T_l \tag{81}$$

Many have addressed the energy dissipation term in thermoelasticity. However, none have considered plasticity and its impact on the irreversibly dissipated energy loss when the material behaves inelastically, primarily when the material is undergoing plastic deformation. It is reported that plastic work is converted into heat, either partially or entirely [58]. The additional energy induced by the plastic work done is non-negligible when plastic deformation occurs under cyclic loading [59] and [60]. Considering the above, a modified lattice energy balance equation is developed as follows which addresses both the thermoelastic and thermoplastic effects in the coupled thermomechanical energy term $L_M = \left(3\lambda + 2\mu\right)\alpha' \cdot T_l \cdot \dot{\varepsilon}_{kk}^{e} - \sigma_{ij} \cdot \dot{\varepsilon}_{ij}^{p}$ [57], [59] and [60]

$$C_l \frac{\partial T_l}{\partial t} = -\nabla \cdot q_l + G\left(T_e - T_l\right) - \left(3\lambda + 2\mu\right)\alpha' \cdot T_l \cdot \dot{\varepsilon}_{kk}^{e} + \sigma_{zz} \cdot \dot{\varepsilon}_{zz}^{p}$$

$$\tau_l \frac{\partial \overrightarrow{q_l}}{\partial t} + \overrightarrow{q_l} = -\kappa_l \nabla T_l \tag{82}$$

where T_l is the lattice temperature, q_l is the lattice heat flux vector, τ_l is the lattice thermal relaxation time, C_l is the electron heat capacity, and κ_l is the electron thermal conductivity. λ and μ are the Lamé constants and α' is the thermal expansion coefficient. σ_{zz} is the stress component in the *z*-direction. ε^e is the elastic part of the total strain while ε^p represents the plastic strain with $\varepsilon_{kk} = \varepsilon_{zz}$ for the uniaxial model employed for the study. The overdot "$\cdot$" denotes the time derivative of the certain variables.

5.5.3. Laser Intensity Source

The temporal and spatial distribution of the laser pulse is a Gaussian function given by [55],

$$S(z,t)=\sqrt{\frac{\beta}{\pi}}\frac{1-R}{t_p\delta_s}\cdot F\cdot\exp\left(-z/\delta_s-\beta\left(\left(t-2t_p\right)/t_p\right)^2\right) \tag{83}$$

where F is the applied laser fluence, t_p is the pulse duration. $R=0.93$ is the reflectivity for gold materials [55] and δ_s is the optical penetration depth. L is the film thickness and $\beta=4\ln(2)$. Eq. (83) is revised to consider an effective absorption depth that includes both optical penetration and ballistic depth. The revised laser intensity has an additional absorption, namely, the ballistic depth δ_b [50] and [51] , as a parameter of the ballistic energy transport,

$$S(z,t)=\sqrt{\frac{\beta}{\pi}}\frac{1-R}{t_p\left(\delta_s+\delta_b\right)\left[1-e^{-L/(\delta_s+\delta_b)}\right]}\cdot F\cdot\exp\left(-z/\left(\delta_s+\delta_b\right)-\beta\left(\left(t-2t_p\right)/t_p\right)^2\right) \tag{84}$$

5.6. Thermo-Elasto-Plasto-Dynamic Equations of Motion

5.6.1. Elasto-Plastic Model

Total strain rate is obtained to appropriate the standard additive decomposition for small deformations [61] and [62] as

$$\dot{\varepsilon}_{ij}=\dot{\varepsilon}^e_{ij}+\dot{\varepsilon}^p_{ij} \tag{85}$$

where $\dot{\varepsilon}^e_{ij}$ denotes the elastic part of the strain rate, and $\dot{\varepsilon}^p_{ij}$ is the plastic strain rate. Before reaching the yield surface, only thermo-elasto-dynamics prevails and the mechanical

response of the target material is predominantly elastic. When loading is uniaxial, the constitutive equation is derived using the non-zero total strain rate in the *z*-direction, $\dot{\varepsilon}_{zz}$,

$$\dot{\varepsilon}_{zz} = \dot{\varepsilon}^{e}_{zz} + \dot{\varepsilon}^{p}_{zz} \tag{86}$$

with all other strains $\varepsilon_{xx} = \varepsilon_{yy} = \varepsilon_{xz} = \varepsilon_{xy} = \varepsilon_{yz} = 0$. The rate of the Cauchy stress, $\dot{\sigma}_{ij}$, is related to the elastic strain rate $\dot{\varepsilon}^{e}_{ij}$ with the thermal-mechanical coupling [61]

$$\dot{\sigma}_{ij} = E\dot{\varepsilon}^{e}_{ij} - \beta\dot{\theta}_{l} \tag{87}$$

here $\dot{\theta}_{l}$ is the time derivative of the absolute temperature, $E = \hat{E}(\theta)$ and $\beta = \hat{\beta}(\theta)$ are the incremental Young's modulus and the stress-temperature modulus, respectively. Substituting Eq. (85) into Eq. (87) to obtain the constitutive stress rate-strain rate relation as [23] and [63],

$$\dot{\sigma}_{ij} = \left(\lambda\dot{\varepsilon}^{e}_{kk} - \alpha'(3\lambda + 2\mu)\dot{\theta}_{l}\right)\delta_{ij} + 2\mu\dot{\varepsilon}^{e}_{ij} \tag{88}$$

The stress rate-strain rate relation in the z-direction for the uniaxial loading can be revised as

$$\dot{\sigma}_{zz} = (\lambda + 2\mu)\cdot\left(\dot{\varepsilon}_{zz} - \dot{\varepsilon}^{p}_{zz}\right) - (3\lambda + 2\mu)\cdot\alpha'\cdot\dot{\theta}_{l} \tag{89}$$

$$\dot{\sigma}_{xx} = \dot{\sigma}_{yy} = \lambda\left(\dot{\varepsilon}_{zz} - \dot{\varepsilon}^{p}_{zz}\right) - (3\lambda + 2\mu)\alpha'\dot{\theta}_{l} \tag{90}$$

where σ_{xx} and σ_{yy} are the normal stresses in the *x*- and *y*- directions, respectively. λ, μ are the Lamé constant, and α' is the thermal expansion coefficient. $\theta_{l} = (T_{l} - T_{0})$ denotes

the lattice temperature variation w.r.t the reference temperature T_0 = 300K. Material elastic and plastic deformations obey the strain-displacement relation [64],

$$\varepsilon_{ij} = \varepsilon_{ij}^{e} + \varepsilon_{ij}^{p} = \frac{1}{2}\left(u_{i,j} + u_{j,i}\right) \tag{91}$$

And the strain-displacement relation for the uniaxial loading is

$$\varepsilon_{zz} = \varepsilon_{zz}^{e} + \varepsilon_{zz}^{p} = \frac{\partial u_z}{\partial z} \tag{92}$$

with u_z being the displacement in the *z*-direction. For metals, the von Mises condition is mostly adopted as the appropriate yield criterion with the dynamic yield surface f_c defined as [62] and [65],

$$f_c = \sqrt{\frac{3}{2}\left(\tau_{ij} - X_{ij}\right)\left(\tau_{ij} - X_{ij}\right)} - Y = 0 \tag{93}$$

where Y is derived from the initial yield stress and the isotropic internal function, τ_{ij} is the deviatoric component of the Cauchy stress tension, with $\tau_{ij} = \sigma_{ij} - \frac{1}{3}\sigma_{kk}\delta_{ij}$, and X_{ij} is the back-stress tensor or the kinematic hardening conjugate force as defined in the nonlinear kinematic hardening rule by Armstrong and Frederick [66]. As plastic flows are constrained by the yield surface, thus $f_c > 0$ is inadmissible, the following consistency conditions need be satisfied,

$$f_c = 0, \qquad \dot{f}_c = 0, \qquad \frac{\partial f_c}{\partial \boldsymbol{\sigma}} : d\sigma \geq 0 \tag{94}$$

Along with the plastic strain rate

$$\dot{\varepsilon}_{ij}^{p} = \dot{\lambda}\frac{\partial f_c}{\partial \tau_{ij}} \tag{95}$$

where $\dot{\lambda}$ is the plastic multiplier. Base on the plastic flow rule, $\dot{\lambda}$ is determined to be equal to the equivalent plastic strain increment as $\dot{\lambda} = \dot{p}$. And $\dot{p}$ is defined as the effective plastic strain given by [62],

$$\dot{p} = \sqrt{\frac{2}{3}\dot{\varepsilon}_{ij}^{p}\,\dot{\varepsilon}_{ij}^{p}} \tag{96}$$

Substitute Eqs. (93) and (96) into Eq. (95) to obtain the plastic strain rate

$$\dot{\varepsilon}_{ij}^{p} = \frac{3}{2}\sqrt{\frac{3}{2}\dot{\varepsilon}_{ij}^{p}\,\dot{\varepsilon}_{ij}^{p}}\cdot\left(\frac{\tau_{ij} - X_{ij}}{Y}\right) \tag{97}$$

For uniaxial loading, irreversible deformations would occur when the yield limit is violated. A revised von Mises yield criterion for the nonlinear kinematic hardening is formulated to define the limit as

$$f_c = \left|\sigma_{zz} - X_z\right| - \sigma_y = 0 \tag{98}$$

where σ_y is the updated yield stress and X_z is the backstress in the *z*-direction. Moreover, the effective plastic strain and the equivalent plastic multiplier are modified for the uniaxial loading as $\dot{\lambda} = \dot{p} = \left|\dot{\varepsilon}_{ij}^{p}\right|$. Eq. (97) thus becomes

$$\dot{\varepsilon}_{ij}^{p} = \psi\,\dot{\lambda} = \psi\left|\dot{\varepsilon}_{ij}^{p}\right| \tag{99}$$

$\psi = 1$ when the stress is tensile and $\psi = -1$ for compression [65].

The study employs the Armstrong and Frederick model and uses the von Mises based yield criterion. The following expression for the evolution of backstress $\dot{X}_z$ in the

z-direction is adopted to resolve the uniaxial Bauschinger effect and its kinematic hardening rule,

$$\dot{X}_z = C\,\dot{\varepsilon}^p_{zz} - \gamma\,\dot{X}_z \cdot \left|\dot{\varepsilon}^p_{zz}\right| \tag{100}$$

where C and γ are material constants determined from a uniaxial testing on gold. Time-integrating the above expression to obtain the backstress,

$$X_z = \psi\frac{C}{\gamma} + \left(X_z^y - \psi\frac{C}{\gamma}\right)\cdot\exp\left(-\gamma\left|\varepsilon^p_{zz} - \varepsilon^{py}_{zz}\right|\right) \tag{101}$$

where $\left(\varepsilon^p_{zz}\right)^y$ and X_z^y denote the updated plastic strain and backstress corresponding to the updated yield stress $\sigma_y = X_y^z + \psi\sigma_Y^0$, with σ_Y^0 being the initial yield stress. Substitute Eq. (101) into the yield surface function in Eq. (98) to get the modified normal stress in the z-direction,

$$\sigma_{zz} = \psi\sigma_Y^0 + \psi\frac{C}{\gamma} + \left(X_z^y - \psi\frac{C}{\gamma}\right)\cdot\exp\left(-\gamma\left|\varepsilon^p_{zz} - \left(\varepsilon^p_{zz}\right)^y\right|\right) \tag{102}$$

5.6.2. Time-Integration of the Elasto-Plastic Model

Applying the thermo-elasto-plastic dynamic theory to ultrafast optical heating requires that the nonlinear kinematic model be numerically time-integrated. The effort is extremely demanding given that the calculation of the hysteresis loop involves the consideration of initial loading, unloading, and reloading. Plastic deformation can only occur when yielding is reached at which time plastic strains start accumulating. As yield backstress and yield stress both increase in hardening, they need be updated for each computing step with the accumulated plastic strain. Moreover, the alternating

compression-tension response requires that the Bauschinger effect be considered. To aid in implementing the complex nonlinear hardening model, a procedure is developed as follows in Figure 23.

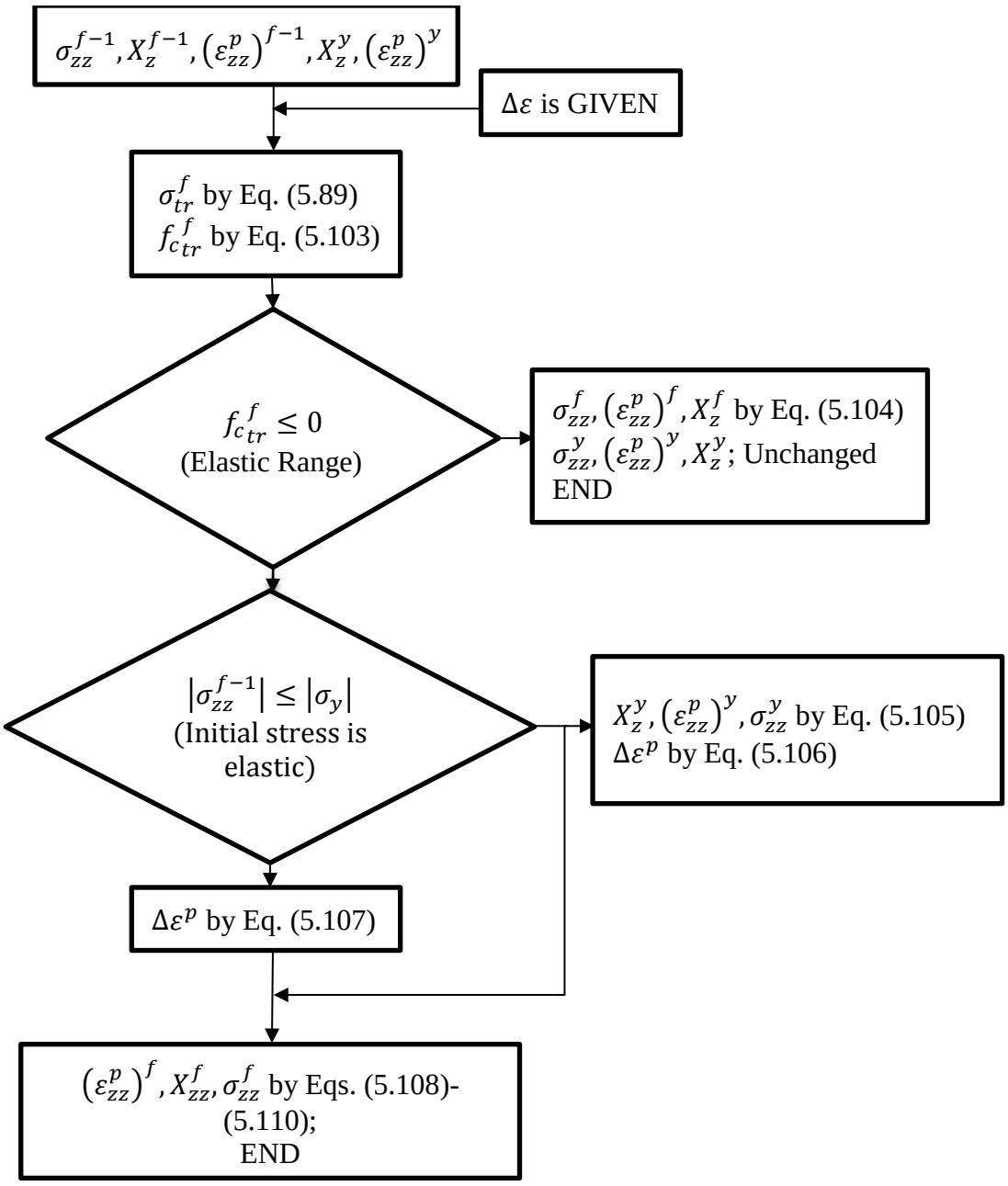

Figure 23. Flow chart of integration algorithm for elastic-plastic behavior

During time iteration, the following variables are calculated in the last time step $t = f - 1$: stress σ_{zz}^{f-1}, plastic strain $\left(\varepsilon_{zz}^{p}\right)^{f-1}$, back-stress X_z^{f-1}, yield back-stess X_z^{y}, the yield plastic strain $\left(\varepsilon_{zz}^{p}\right)^{y}$, yield stress σ^{y}, and the strain increment $\Delta\varepsilon$ to advance from the previous time moment $t = f - 1$ to the next instance at $t = f$. Since the material was not overloaded in the previous loading history, the initial loading at the present moment requires that $X_z^{f-1} = X_z^{y} = 0$, $\left(\varepsilon_{zz}^{p}\right)^{f-1} = \left(\varepsilon_{zz}^{p}\right)^{y} = 0$, and $\sigma^{y} = \sigma_Y^0$. When hardening occurs at $\left|\sigma^{y}\right| > \sigma_Y^0$ a non-zero accumulated plastic strain is generated. After each iteration, the variables σ_{zz}^{f}, X_z^{f}, $\left(\varepsilon_{zz}^{p}\right)^{f}$, X_z^{y}, $\left(\varepsilon_{zz}^{p}\right)^{y}$ and σ^{y} at $t = f$, are updated and returned as the given values for the next computing step. The followings elaborate on the specific procedure:

1) Estimate trial stress and trial yield function

Firstly, assume that the stress-field initiated by thermal expansion is elastic and calculate the trial stress σ_{tr}^{f} at $t = f$ using Eq. (89). And the corresponding trial yield function f_{ctr}^{f} is calculated by using Eq. (98), which may not strictly follow the consistency condition ($f_c \le 0$) as follows,

$$f_{ctr}^{f} = \left|\sigma_{tr}^{f} - X_z^{f-1}\right| - \sigma_y = 0 \tag{103}$$

Whether the current stress state is tension or compression is determined by the multiplier ψ.

2) Check for meeting consistency condition

Check whether the calculated yield function satisfies the consistency condition. That is to determine if the trial stress σ_{tr}^{f} is lower than the yield stress σ^{y}. If $f_{tr}^{f} \le 0$, the trial stress σ_{tr}^{f} is below the yield stress and elasticity prevails. Then sets,

$$\sigma_{zz}^{f} = \sigma_{tr}^{f}, \quad X_{zz}^{f} = X_{z}^{f-1}, \quad \left(\varepsilon_{zz}^{p}\right)^{f} = \left(\varepsilon_{zz}^{p}\right)^{f-1} \tag{104}$$

The yield backstress X_{z}^{y}, yield stress σ^{y} and the corresponding yield plastic strain $\left(\varepsilon_{zz}^{p}\right)^{y}$ stay unchanged. After is, move on to the next time step. In unloading, the initial stress state can be either elastic or plastic. This needs not be checked since the material behaves elastically as long as the trial stress σ_{tr}^{f} is lower than the yield stress.

3) Evaluate initial stress σ_{zz}^{f-1}

If $f_{ctr}^{f} > 0$, the calculated yield function fails to satisfy the consistency condition, thus indicating yielding. The trial stress σ_{tr}^{f} is no longer available for calculating σ_{zz}^{f} and σ_{zz}^{f} needs be considered for plastic response. Before calculating the current stress, the initial stress σ_{zz}^{f-1} needs established by comparing with the yield stress σ^{y}.

If $\left|\sigma_{zz}^{f-1}\right| \le \left|\sigma_{y}\right|$, it implies that the stress was initially in the elastic state and is reaching the plastic yield surface. This is possible in both initial loading and reloading. To begin, the yield stress is $\sigma_{y} = \sigma_{Y}^{0}$, the yield plastic strain is $\left(\varepsilon_{zz}^{p}\right)^{y} = 0$ and the yield backstress is $X_{z}^{y} = 0$ in the initial loading. However, due to hardening caused by the elastic-plastic transition in the reloading process, the yield stress increases along with the increase of the plastic strain and yield backstress. The yield stress σ_{y}, yield back-stress

X_z^y and the yield plastic strain $\left(\varepsilon_{zz}^p\right)^y$ therefore need be updated in order to calculate the accumulated plastic strain and actual stress to get

$$X_z^y = X_z^{f-1}, \quad \left(\varepsilon_{zz}^p\right)^y = \left(\varepsilon_{zz}^p\right)^{f-1}, \quad \sigma_y = X_z^y + \psi\sigma_Y^0 \tag{105}$$

Moreover, the plastic strain increment $\Delta\varepsilon^p$ which is part of the total strain increment is calculated as follows

$$\Delta\varepsilon^p = \Delta\varepsilon - \frac{1}{E}\left(X_z^y + \psi\sigma_Y^0 - \sigma_{zz}^{f-1}\right) \tag{106}$$

If $\left|\sigma_{zz}^{f-1}\right| > \left|\sigma_y\right|$, the stress initiates in the plastic state and continues to increase in the plastic yield surface. The yield stress σ_y, yield back-stress X_z^y and the yield plastic strain $\left(\varepsilon_{zz}^p\right)^y$ stay unchanged at $t = f$, since no elastic-plastic transition occurs. The plastic strain increment equals to the total strain increment

$$\Delta\varepsilon^p = \Delta\varepsilon \tag{107}$$

4) Plastic correction

For $f_{ctr}^f > 0$, the trial yield function does not satisfy the consistency condition, indicating that the calculated trial stress σ_{tr}^f cannot represent the actual stress. Thus, all the accumulated plastic strain $\left(\varepsilon_{zz}^p\right)^f$, back-stress X_z^f, and actual stress σ_{zz}^f need be determined using the AF nonlinear kinematic hardening model. The unknown plastic strain increment $\Delta\varepsilon^p$ has been determined by either Eq. (106) or Eq. (107) depending on the state of the initial stress σ_{zz}^{f-1}. Hence, the accumulated plastic strain $\left(\varepsilon_{zz}^p\right)^f$, current

back-stress X_z^f and current stress σ_{zz}^f are subsequently calculated using the following equations,

$$\left(\varepsilon_{zz}^p\right)^f = \left(\varepsilon_{zz}^p\right)^{f-1} + \Delta\varepsilon^p \tag{108}$$

$$X_{zz}^f = \psi\frac{C}{\gamma} + \left[X_{zz}^y - \psi\frac{C}{\gamma}\right]\cdot\exp\left(-\gamma\cdot\left|\left(\varepsilon_{zz}^p\right)^f - \left(\varepsilon_{zz}^p\right)^y\right|\right) \tag{109}$$

$$\sigma_{zz}^f = \psi\sigma_Y^0 + \psi\frac{C}{\gamma} + \left[X_z^y - \psi\frac{C}{\gamma}\right]\cdot\exp\left(-\gamma\cdot\left|\left(\varepsilon_{zz}^p\right)^f - \left(\varepsilon_{zz}^p\right)^y\right|\right) \tag{110}$$

5.7. Discretization on Finite Difference Scheme

5.7.1. Initial and Boundary Conditions

The initial conditions defined for the electron and ion number density and the electron and lattice temperatures are

$$\begin{aligned} &n_e(z,0) = n_i(z,0) = 0 \\ &T_e(z,0) = T_l(z,0) = T_0 \\ &\sigma_{zz}(z,0) = \sigma_{xx}(z,0) = \sigma_{yy}(z,0) = 0 \\ &u_z(z,0) = \dot{u}_z(z,0) = 0 \end{aligned} \tag{111}$$

where the ambient temperature T_0 is 300K and the initial conditions for n_e and n_i are that no electrons or ions emit from the target surface. For simplicity, the following thermal-insulation boundary conditions are specified by neglecting the heat dissipated from the front and back surfaces during ultrashort laser pulsing,

$$
\begin{aligned}
&j_e(0,t) = j_t \\
&j_e(L,t) = 0 \\
&j_i(0,t) = j_i(L,t) = 0 \\
&q_e(0,t) = q_l(0,t) = 0 \\
&q_e(L,t) = q_l(L,t) = 0 \\
&\sigma_{zz}(0,t) = \sigma_{zz}(L,t) = 0
\end{aligned}
\tag{112}
$$

where the front surface at $z = 0$ and the back surface $z = L$ are both stress-free. Heat fluxes q on all the open surfaces are negligible. And the electron emission rate j_e at the front surface is depicted by the electron emission rate j_t at all time.

5.7.2. Summary of Field Equations

Eqs. (75) – (78), (80), (82), (85) – (102) are the field equations dictating the thermo-elasto-plasto-dynamic behaviors of polycrystalline metallic materials in response to ultrafast laser irradiation. The governing equations consider the absorption from the laser, electron and lattice energy transports, energy exchange due to electron-lattice interaction, and coupled thermos-elastoplastic responses covering from the onset of laser irradiation to the reaching of the equilibrium state from non-equilibrium. Of these equations, Eq. (84) describes laser absorption as a function of optical penetration and ballistic motion. Eqs. (75) – (78) define electron dynamics as one that admits electron emission. They also describe the induced electronic current density and the generated electric field inside the target localized near the irradiated surface. Defining the constitutive equations that govern the coupled thermal-mechanical field response in the metallic target, Eqs. (80), (82), and (85) – (102) cover thermoelasticity and a modified

plasticity with a nonlinear kinematic hardening model. Eqs. (103) – (110) provide the procedure for implementing the nonlinear kinematic hardening rule.

Since the majority of the energy among the excited electrons are spent to emit the electrons and transfer to the lattice subsystem when the thermal equilibrium is reached at $T_e = T_l$, thus, Eqs. (82), (85) – (102), which describe the dynamics of thermal-mechanical coupling in lattice, are further time-integrated to explore the energy transport dynamics in the material.

5.7.3. Discretization Model

The temporal and spatial evolutions of the governining equations are solved using a finite difference model. All numerical time integrations are performed with an explicit scheme. To resolve electron emission, electron current transport, electron and lattice energy transports, and the induced elasto-plasto behaviors, the field equations are discretized equations as follows

$$\left(j_e\right)_{i-1}^{f-1} = q\mu_e \frac{\left(n_e\right)_{i-2}^{f-1} + \left(n_e\right)_i^{f-1}}{2} \left(E\right)_{i-1}^{f-1} + q \frac{\left(D_e\right)_{i-2}^{f-1} + \left(D_e\right)_i^{f-1}}{2} \cdot \frac{\left(n_e\right)_i^{f-1} - \left(n_e\right)_{i-2}^{f-1}}{\Delta z} \tag{113}$$

$$\left(j_i\right)_{i-1}^{f-1} = -q\mu_i \frac{\left(n_i\right)_{i-2}^{f-1} + \left(n_i\right)_i^{f-1}}{2} E_{i-1} - q \frac{\left(D_i\right)_{i-2}^{f-1} + \left(D_i\right)_i^{f-1}}{2} \cdot \frac{\left(n_i\right)_i^{f-1} - \left(n_i\right)_{i-2}^{f-1}}{\Delta z} \tag{114}$$

$$\left(n_e\right)_i^f = \left(n_e\right)_i^{f-1} + \frac{\Delta t}{q} \cdot \frac{\left(j_e\right)_{i+1}^{f-1} - \left(j_e\right)_{i-1}^{f-1}}{\Delta z} \tag{115}$$

$$\left(n_i\right)_i^f = \left(n_i\right)_i^{f-1} - \frac{\Delta t}{q} \cdot \frac{\left(j_i\right)_{i+1}^{f-1} - \left(j_i\right)_{i-1}^{f-1}}{\Delta z} \tag{116}$$

$$\left(\dot{u}_z\right)_{i+1}^f = \left(\dot{u}_z\right)_{i+1}^{f-1} + \frac{\Delta t}{\rho} \cdot \frac{\left(\sigma_{zz}\right)_{i+2}^{f-1} - \left(\sigma_{zz}\right)_i^{f-1}}{\Delta z} \tag{117}$$

$$\left(\dot{\varepsilon}_{zz}\right)_i^{f-1} = \frac{\left(\dot{u}_z\right)_{i+1}^{f-1} - \left(\dot{u}_z\right)_{i-1}^{f-1}}{\Delta z} \tag{118}$$

$$\begin{aligned}\left(T_e\right)_i^f = {} & \left(T_e\right)_i^{f-1} - \Delta t \cdot \frac{\left(j_e\right)_{i+1}^{f-1}}{q\left(n_e\right)_i^{f-1}} \cdot \frac{\left(T_e\right)_{i+2}^{f-1} - \left(T_e\right)_i^{f-1}}{\Delta z} \\ & - \frac{\Delta t}{\left(C_e\right)_i^{f-1}} \cdot \frac{\left(q_e\right)_{i+1}^{f-1} - \left(q_e\right)_{i-1}^{f-1}}{\Delta z} - \frac{\Delta t}{\left(C_e\right)_i^{f-1}} \cdot G_i^{f-1}\left(\left(T_e\right)_i^{f-1} - \left(T_l\right)_i^{f-1}\right) + \frac{\Delta t}{\left(C_e\right)_i^{f-1}} \cdot S_i^f\end{aligned} \tag{119}$$

$$\begin{aligned}\left(T_l\right)_i^f = {} & \left(T_l\right)_{li}^f - \frac{\Delta t}{C_l} \cdot \frac{\left(q_l\right)_{i+1}^{f-1} - \left(q_l\right)_{i-1}^{f-1}}{\Delta z} + \frac{\Delta t}{C_l} \cdot G_i^{f-1}\left(\left(T_e\right)_i^{f-1} - \left(T_l\right)_i^{f-1}\right) \\ & - \frac{\Delta t}{C_l}\left(3\lambda + 2\mu\right)\alpha' \cdot \left(T_l\right)_{i-1}^f \left(\left(\dot{\varepsilon}_{zz}\right)_i^{f-1} - \left(\dot{\varepsilon}_{zz}^p\right)_i^{f-1}\right) + \frac{\Delta t}{C_l} \cdot \left(\sigma_{zz}\right)_i^{f-1} \cdot \left(\dot{\varepsilon}_{zz}^p\right)_i^{f-1}\end{aligned} \tag{120}$$

$$\left(q_e\right)_{i-1}^f = \left(1 - \frac{\Delta t}{\tau_e}\right) \cdot \left(q_e\right)_{i-1}^{f-1} - \frac{\Delta t}{\tau_e} \cdot \frac{\left(\kappa_e\right)_i^f + \left(\kappa_e\right)_{i-2}^f}{2} \cdot \frac{\left(T_e\right)_i^{f-1} - \left(T_e\right)_{i-2}^{f-1}}{\Delta z} \tag{121}$$

$$\left(q_l\right)_{i-1}^{f}=\left(1-\frac{\Delta t}{\tau_l}\right)\cdot\left(q_l\right)_{i-1}^{f-1}-\frac{\Delta t}{\tau_l}\cdot\kappa_l\cdot\frac{\left(T_l\right)_i^{f-1}-\left(T_l\right)_{i-2}^{f-1}}{\Delta z} \tag{122}$$

$$\begin{aligned}\left(\sigma_{tr}\right)_i^{f}=\left(\sigma_{zz}\right)_i^{f-1}+\Delta t\cdot\left(\lambda+2\mu\right)\cdot\left(\left(\dot{\varepsilon}_{zz}\right)_i^{f-1}-\left(\dot{\varepsilon}_{zz}^{p}\right)_i^{f-1}\right)\\-\left(3\lambda+2\mu\right)\cdot\alpha'\left(\left(T_l\right)_i^{f}-\left(T_l\right)_i^{f-1}\right)\end{aligned} \tag{123}$$

$$\left(f_{tr}\right)_i^{f}=\left|\left(\sigma_{tr}\right)_i^{f}-\left(X_{tr}\right)_i^{f}\right|-\sigma_Y^0 \tag{124}$$

If $\left(f_{tr}\right)_i^{f}\le 0$ (Elastic), then

$$\left(\sigma_{zz}\right)_i^{f}=\left(\sigma_{tr}\right)_i^{f} \tag{125}$$

$$\left(\Delta\varepsilon_{zz}^{p}\right)_i^{f}=0 \tag{126}$$

$$\left(\varepsilon_{zz}^{p}\right)_i^{f}=\left(\varepsilon_{zz}^{p}\right)_i^{f-1} \tag{127}$$

$$\left(X\right)_i^{y}=\left(X_{tr}\right)_i^{f} \tag{128}$$

$$\left(\varepsilon_{zz}^{p}\right)_i^{y}=\left(\varepsilon_{zz}^{p}\right)_i^{f} \tag{129}$$

If $\left(f_{tr}\right)_i^f > 0$ (Plastic), and $\left|\left(\sigma_{zz}\right)_i^{f-1}\right| \le \left|\left(X\right)_i^y + \mathrm{sgn}\left(\left(\Delta\varepsilon_{zz}\right)_i^f\right)\cdot\sigma_Y^0\right|$, then

$$\left(\Delta\varepsilon_{zz}^p\right)_i^f = \left(\Delta\varepsilon_{zz}\right)_i^f - \frac{1}{E}\left[\left(X\right)_i^y + \mathrm{sgn}\left(\left(\Delta\varepsilon_{zz}\right)_i^f\right)\cdot\sigma_Y^0 - \left(\sigma_{zz}\right)_i^{f-1}\right] \tag{130}$$

If $\left(f_{tr}\right)_i^f > 0$ (Plastic), and $\left|\left(\sigma_{zz}\right)_i^{f-1}\right| > \left|\left(X\right)_i^y + \mathrm{sgn}\left(\left(\Delta\varepsilon_{zz}\right)_i^{f-1}\right)\cdot\sigma_Y^0\right|$, then

$$\left(\Delta\varepsilon_{zz}^p\right)_i^f = \left(\Delta\varepsilon_{zz}\right)_i^f \tag{131}$$

Continuously, obtains as

$$\left(\varepsilon_{zz}^p\right)_i^f = \left(\varepsilon_{zz}^p\right)_i^{f-1} + \left(\Delta\varepsilon_{zz}^p\right)_i^f \tag{132}$$

$$X_i^f = \mathrm{sgn}\left(\Delta\varepsilon_i\right)\cdot\frac{C}{\gamma} + \left[X_i^y - \mathrm{sgn}\left(\Delta\varepsilon_i\right)\cdot\frac{C}{\gamma}\right]\cdot\exp\left(-\gamma\cdot\left|\varepsilon_{pi}^{\ f} - \varepsilon_{pi}^{\ y}\right|\right) \tag{133}$$

$$\begin{aligned}&\left(\sigma_{zz}\right)_i^f \\ &= \mathrm{sgn}\left(\left(\Delta\varepsilon_{zz}\right)_i^f\right)\cdot\sigma_Y^0 + \mathrm{sgn}\left(\left(\Delta\varepsilon_{zz}\right)_i^f\right)\cdot\frac{C}{\gamma} \\ &\quad + \left[\left(X\right)_i^y - \mathrm{sgn}\left(\left(\Delta\varepsilon_{zz}\right)_i^f\right)\cdot\frac{C}{\gamma}\right]\cdot\exp\left(-\gamma\cdot\left|\left(\varepsilon_{zz}^p\right)_i^f - \left(\varepsilon_{zz}^p\right)_i^y\right|\right)\end{aligned} \tag{134}$$

$$\left(\dot{\varepsilon}_{zz}^p\right)_i^f = \frac{\left(\varepsilon_{zz}^p\right)_i^f - \left(\varepsilon_{zz}^p\right)_i^{f-1}}{\Delta t} = \frac{\left(\Delta\varepsilon_{zz}^p\right)_i^f}{\Delta t} \tag{135}$$

5.8. Summary

In the present chapter, the phenomena and observations associated with ultrafast laser ablation at different laser fluences were reviewed. It was concluded that a mass removal mechanism for light laser intensity ablation must be established to differentiate from the one that incorporates phase transition and phase explosion in explaining ultrafast laser ablation with extremely high fluence. The inadequacy of current theories in describing the mechanical damage and surface morphology induced by femtosecond laser ablation with light laser intensity was noted. A comprehensive formulation viable for describing both electronic and thermo-elasto-plasto-dynamics of non-thermal ablation in polycrystalline metal was presented. The formulation followed the time scales characteristic of each of the underlying dynamics and obeyed the principle of energy conservation when establishing the energy transport of the electron and lattice subsystem. Also presented were a procedure for time-integrating the proposed nonlinear kinematic hardening model and a discretized version of the field equations that was the computational model of the thermos-elasto-plastodynamics developed for the resrach.

5.9. References

[1] Nolte, S., Momma, C., Jacobs, H., Tünnermann, A., Chichkov, B. N., Wellegehausen, B., and Welling, H., "Ablation of metals by ultrashort laser pulses," *JOSA B*, Vol. 14, No. 10, 1997, pp. 2716-2722.

[2] Huang, J., Zhang, Y., Chen, J. K., and Yang, M., "Modeling of ultrafast phase change processes in a thin metal film irradiated by femtosecond laser pulse trains," *Journal of Heat Transfer*, Vol. 133, No. 3, 2011, pp. 031003.

[3] Zhao, X., and Shin, Y. C., "Coulomb explosion and early plasma generation during femtosecond laser ablation of silicon at high laser fluence," *Journal of Physics D*: *Applied Physics*, Vol. 46, No. 33, 2013, pp. 335501.

[4] Zhigilei, L. V., Lin, Z., and Ivanov, D. S., "Atomistic modeling of short pulse laser ablation of metals: connections between melting, spallation, and phase explosion," *The Journal of Physical Chemistry C*, Vol. 113, No. 27, 2009, pp. 11892-11906.

[5] Rethfeld, B., Ivanov, D. S., Garcia, M. E., and Anisimov, S. I., "Modelling ultrafast laser ablation," *Journal of Physics D*: *Applied Physics*, Vol. 50, No. 19, 2017, pp. 193001.

[6] Rethfeld, B., Sokolowski-Tinten, K., Von der Linde, D., and Anisimov, S. I., "Ultrafast thermal melting of laser-excited solids by homogeneous nucleation," *Physical review B*, Vol. 65, No. 9, 2002, pp. 092103.

[7] Labutin, T. A., Lednev, V. N., Ilyin, A. A., and Popov, A. M., "Femtosecond laser-induced breakdown spectroscopy," *Journal of Analytical Atomic Spectrometry*, Vol. 31, No. 1, 2016, pp. 90-118.

[8] Bulgakova, N. M., Stoian, R., Rosenfeld, A., Hertel, I. V., Marine, W., and Campbell, E. E. B., "A general continuum approach to describe fast electronic transport in pulsed laser irradiated materials: The problem of Coulomb explosion," *Applied physics A*, Vol. 81, No. 2, 2005, pp. 345-356.

[9] Cheng, C., and Xu, X., "Mechanisms of decomposition of metal during femtosecond laser ablation," *Physical review B*, Vol. 72, No. 16, 2005, pp. 165415.

[10] Izawa, Y., Setuhara, Y., Hashida, M., Fujita, M., and Izawa, Y., "Ablation and amorphization of crystalline Si by femtosecond and picosecond laser irradiation," *Japanese journal of applied physics*, Vol. 45, No. 7, 2006, pp. 5791.

[11] Bäuerle, D., "Laser processing and chemistry", 2011, pp. 279-313.

[12] Sokolowski-Tinten, K., Bialkowski, J., Cavalleri, A., von der Linde, D., Oparin, A., Meyer-ter-Vehn, J., and Anisimov, S. I., "Transient states of matter during short pulse laser ablation," *Physical Review Letters*, Vol. 81, No. 1, 1998, pp. 224.

[13] Cheng, J., Liu, C.-S., Shang, S., Liu, D., Perrie, W., Dearden, G., and Watkins, K., "A review of ultrafast laser materials micromachining," *Optics & Laser Technology*, Vol. 46, 2013, pp. 88-102.

[14] Perez, D., and Lewis, L. J., "Molecular-dynamics study of ablation of solids under femtosecond laser pulses," *Physical review B*, Vol. 67, No. 18, 2003, pp. 184102.

[15] Niso, D., Francesca, C. G., Sibillano, T., Mezzapesa, F. P., Ancona, A., and Lugarà, P. M., "Role of heat accumulation on the incubation effect in multi-shot laser ablation of stainless steel at high repetition rates," *Optics express*, Vol. 22, No. 10, 2014, pp. 12200-12210.

[16] Liu, J., Jia, X., Wu, W., Cheng, K., Feng, D., Zhang, S., Sun, Z., and Jia, T., "Ultrafast imaging on the formation of periodic ripples on a Si surface with a prefabricated nanogroove induced by a single femtosecond laser pulse," *Optics express*, Vol. 26, No. 5, 2018, pp. 6302-6315.

[17] Zuhlke, C. A., Tsibidis, G. D., Anderson, T., Stratakis, E., Gogos, G., and Alexander, D. R., "Investigation of femtosecond laser induced ripple formation on copper for varying incident angle," *AIP Advances*, Vol. 8, No. 1, 2018, pp. 015212.

[18] Das, S. K., Messaoudi, H., Debroy, A., McGlynn, E., and Grunwald, R., "Multiphoton excitation of surface plasmon-polaritons and scaling of nanoripple formation in large bandgap materials," *Optical Materials Express*, Vol. 3, No. 10, 2013, pp. 1705-1715.

[19] Tsibidis, G. D., Stratakis, E., and Aifantis, K. E., "Thermoplastic deformation of silicon surfaces induced by ultrashort pulsed lasers in submelting conditions," *Journal of Applied Physics*, Vol. 111, No. 5, 2012, pp. 053502.

[20] Sakakura, M., Fukuda, N., Shimotsuma, Y., and Miura, K., "Dynamics of interference of femtosecond laser-induced stress waves and crack formation inside a LiF single crystal," *Laser Applications in Microelectronic and Optoelectronic Manufacturing (LAMOM) XIX*, Vol. 8967, 2014, pp. 89670C.

[21] Zhao, X., and Shin, Y. C., "A two-dimensional comprehensive hydrodynamic model for femtosecond laser pulse interaction with metals," *Journal of Physics D: Applied Physics*, Vol. 45, No. 10, 2012, pp. 105201.

[22] Dirscherl, M., Esser, G., and Schmidt, M., "Ultrashort pulse laser bending," *Journal of Laser Micro/Nanoengineering*, Vol. 1, No. 1, 2006, pp. 54-60.

[23] Qi, X., and Suh, C. S., "Elasto-viscoplastic response of silicon to femtosecond laser heating at elevated temperature," *Journal of Thermal Stresses*, Vol. 34, No. 2, 2011, pp. 115-137.

[24] Beuton, R., Chimier, B., Breil, J., Hébert, D., Mishchik, K., Lopez, J., Maire, P. H., and Duchateau, G., "Thermo-elasto-plastic simulations of femtosecond laser-induced multiple-cavity in fused silica," *Applied Physics A*, Vol. 124, No. 4, 2018, pp. 324.

[25] Zeifman, M. I., Garrison, B. J., and Zhigilei, L. V., "Combined molecular dynamics–direct simulation Monte Carlo computational study of laser ablation plume evolution," *Journal of applied physics*, Vol. 92, No. 4, 2002, pp. 2181-2193.

[26] Yilbas, B. S., "Short-pulse laser heating of gold-chromium layers: thermo-elasto-plastic analysis," *Journal of Physics D: Applied Physics*, Vol. 35, No. 11, 2002, pp. 1210.

[27] Haustrup, N., and O'Connor, G. M., "Impact of laser wavelength on the emission of electrons and ions from thin gold films during femtosecond laser ablation," *Applied Surface Science*, Vol. 302, 2014, pp. 1-5.

[28] Geindre, J. P., Audebert, P., Rousse, A., Fallies, F., Gauthier, J. C., Mysyrowicz, A., Dos Santos, A., Hamoniaux, G., and Antonetti, A., "Frequency-domain interferometer for measuring the phase and amplitude of a femtosecond pulse probing a laser-produced plasma," *Optics letters*, Vol. 19, No. 23, 1994, pp. 1997-1999.

[29] Riffe, D. M., Wang, X. Y., Downer, M. C., Fisher, D. L., Tajima, T., Erskine, J. L., and More, R. M., "Femtosecond thermionic emission from metals in the space-charge-limited regime," *JOSA B*, Vol. 10, No. 8, 1993, pp. 1424-1435.

[30] Amoruso, S., Wang, X., Altucci, C., De Lisio, C., Armenante, M., Bruzzese, R., and Velotta, R., "Thermal and nonthermal ion emission during high-fluence femtosecond laser ablation of metallic targets," *Applied Physics Letters*, Vol. 77, No. 23, 2000, pp. 3728-3730.

[31] Tao, S., and Wu, B., "The effect of emitted electrons during femtosecond laser–metal interactions: A physical explanation for coulomb explosion in metals," *Applied Surface Science*, Vol. 298, 2014, pp. 90-94.

[32] Hashida, M., Namba, S., Okamuro, K., Tokita, S., and Sakabe, S., "Ion emission from a metal surface through a multiphoton process and optical field ionization," *Physical Review B*, Vol. 81, No. 11, 2010, pp. 115442.

[33] Dachraoui, H., Husinsky, W., and Betz, G., "Ultra-short laser ablation of metals and semiconductors: evidence of ultra-fast Coulomb explosion," *Applied Physics A*, Vol. 83, No. 2, 2006, pp. 333-336.

[34] Dunne, F., and Petrinic, N., "Introduction to computational plasticity," *Oxford University Press on Demand*, 2005.

[35] Rezaiee-Pajand, M., and Sinaie, S., "On the calibration of the Chaboche hardening model and a modified hardening rule for uniaxial ratcheting prediction," *International Journal of Solids and Structures*, Vol. 46, No. 16, 2009, pp. 3009-3017.

[36] Kobayashi, M., and Ohno, N., "Implementation of cyclic plasticity models based on a general form of kinematic hardening," *International Journal for Numerical Methods in Engineering*, Vol. 53, No. 9, 2002, pp. 2217-2238.

[37] McDowell, D. L., "A nonlinear kinematic hardening theory for cyclic thermoplasticity and thermoviscoplasticity," *International Journal of Plasticity*, Vol. 8, No. 6, 1992, pp. 695-728.

[38] Ho, K., "Effect of the rate dependence of nonlinear kinematic hardening rule on relaxation behavior," *International Journal of Solids and Structures*, Vol. 45, No. 3-4, 2008, pp. 821-839.

[39] Hennessey, C., Castelluccio, G. M., and McDowell, D. L., "Sensitivity of polycrystal plasticity to slip system kinematic hardening laws for Al 7075-T6," *Materials Science and Engineering: A*, Vol. 687, 2017, pp. 241-248.

[40] Chaboche, J.-L., and Rousselier, G., "On the plastic and viscoplastic constitutive equations—Part I: Rules developed with internal variable concept," *Journal of Pressure Vessel Technology*, Vol. 105, No. 2, 1983, pp. 153-158.

[41] Ohno, N., and Wang, J-D., "Kinematic hardening rules with critical state of dynamic recovery, part I: formulation and basic features for ratchetting behavior," *International journal of plasticity*, Vol. 9, No. 3, 1993, pp. 375-390.

[42] Van Driel, H. M., "Kinetics of high-density plasmas generated in Si by 1.06-and 0.53-μm picosecond laser pulses," *Physical Review B*, Vol. 35, No. 15, 1987, pp. 8166.

[43] Qi, X., "Ultrafast laser induced thermo-elasto-visco-plastodynamics in single crystalline silicon," Ph.D. Dissertation, Texas A&M University, 2009.

[44] Chen, J. K., Tzou, D. Y., and Beraun, J. E., "Numerical investigation of ultrashort laser damage in semiconductors," *International Journal of Heat and Mass Transfer*, Vol. 48, No. 3-4, 2005, pp. 501-509.

[45] Qi, X., and Suh, C. S., "Generalized thermo-elastodynamics for semiconductor material subject to ultrafast laser heating. Part I: Model description and validation," *International Journal of Heat and Mass Transfer*, Vol. 53, No. 1-3, 2010, pp. 41-47.

[46] Qi, X., and Suh, C. S., "Ultrafast laser-induced elastodynamics in single crystalline silicon part I: model formulation," *Journal of Thermal Stresses*, Vol. 32, No. 5, 2009, pp. 477-493.

[47] Bulgakova, N. M., Stoian, R., Rosenfeld, A., Hertel, I. V., and Campbell, E. E. B., "Electronic transport and consequences for material removal in ultrafast pulsed laser ablation of materials," *Physical Review B*, Vol. 69, No. 5, 2004, pp. 054102.

[48] Bechtel, J. H., Smith, W. L., and Bloembergen, N., "Two-photon photoemission from metals induced by picosecond laser pulses," *Physical Review B*, Vol. 15, No. 10, 1977, pp. 4557.

[49] Girardeau-Montaut, J. P., and Girardeau-Montaut, C., "Theory of ultrashort nonlinear multiphoton photoelectric emission from metals," *Physical Review B*, Vol. 51, No. 19, 1995, pp. 13560.

[50] Hohlfeld, J., Wellershoff, S-S., Güdde, J., Conrad, U., Jähnke, V., and Matthias, E., "Electron and lattice dynamics following optical excitation of metals," *Chemical Physics*, Vol. 251, No. 1-3, 2000, pp. 237-258.

[51] Wellershoff, S-S., Hohlfeld, J., Güdde, J., and Matthias, E., "The role of electron–phonon coupling in femtosecond laser damage of metals," *Applied Physics A*, Vol. 69, No. 1, 1999, pp. S99-S107.

[52] Ferrini, G., Banfi, F., Giannetti, C., and Parmigiani, F., "Non-linear electron photoemission from metals with ultrashort pulses," *Nuclear Instruments and Methods in Physics Research Section A: Accelerators, Spectrometers, Detectors and Associated Equipment*, Vol. 601, No. 1-2, 2009, pp. 123-131.

[53] Girardeau‐Montaut, J. P., Girardeau‐Montaut, C., Moustaizis, S. D., and Fotakis, C., "Nonlinearity and inversion of femtosecond single‐and two‐photon photoelectric emission sensitivities from gold," *Applied physics letters*, Vol. 64, No. 26, 1994, pp. 3664-3666.

[54] Chen, Z., and Mao, S. S., "Femtosecond laser-induced electronic plasma at metal surface," *Applied Physics Letters*, Vol. 93, No. 5, 2008, pp. 051506.

[55] Chen, J. K., and Beraun, J. E., "Numerical study of ultrashort laser pulse interactions with metal films," *Numerical Heat Transfer: Part A: Applications*, Vol. 40, No. 1, 2001, pp. 1-20.

[56] Mao, X., and Suh, C. S., "Generalized Thermo-Elastodynamics for Polycrystalline Metallic Thin Films in Response to Ultrafast Laser Heating," *Journal of Thermophysics and Heat Transfer*, 2018, pp. 1-11. doi:10.2514/1.t5429

[57] Ummenhofer, T., and Medgenberg, J., "Numerical modelling of thermoelasticity and plasticity in fatigue-loaded low carbon steels: Studies for a thermographic

approach," *Quantitative InfraRed Thermography Journal*, Vol. 3, No. 1, 2006, pp. 71-91.

[58] Bhalla, K. S., Zehnder, A. T., and Han, X., "Thermomechanics of slow stable crack growth: closing the loop between experiments and computational modeling," *Engineering Fracture Mechanics*, Vol. 70, No. 17, 2003, pp. 2439-2458.

[59] Dillon Jr, O. W., "Coupled thermoplasticity," *Journal of the Mechanics and Physics of Solids*, Vol. 11, No. 1, 1963, pp. 21-33.

[60] Rusinek, A., and Klepaczko, J. R., "Experiments on heat generated during plastic deformation and stored energy for TRIP steels," *Materials & Design*, Vol. 30, No. 1, 2009, pp. 35-48.

[61] Anand, L., "Constitutive equations for the rate-dependent deformation of metals at elevated temperatures," *Journal of engineering materials and technology*, Vol. 104, No. 1, 1982, pp. 12-17.

[62] Voyiadjis, G. Z., and Abu Al-Rub, R. K., "Thermodynamic based model for the evolution equation of the backstress in cyclic plasticity," *International Journal of Plasticity*, Vol. 19, No. 12, 2003, pp. 2121-2147.

[63] Qi, X., Liu, L., Suh, C. S., and Chona, R., "Elasto-viscoplastic wave thermometry for single crystalline silicon processing," *International Journal of Applied Mechanics*, Vol. 2, No. 4, 2010, pp. 827-849.

[64] Burenin, A. A., Dats, E. P., and Murashkin, E. V., "Formation of the residual stress field under local thermal actions," *mechanics of Solids*, Vol. 49, No. 2, 2014, pp. 218-224.

[65] Halama, R., Sedlák, J., and Šofer, M., "Phenomenological modelling of cyclic plasticity," *In Numerical Modelling*. InTech, 2012.

[66] Armstrong, P. J., and Frederick, C. O., "A mathematical representation of the multiaxial Bauschinger effect," Vol. 731. Berkeley: Central Electricity Generating Board [and] Berkeley Nuclear Laboratories, Research & Development Department, 1966.

[67] Dorgan, R. J., and Voyiadjis, G. Z., "Functional forms of hardening internal state variables in modeling elasto-plastic behavior," *Archives of Mechanics*, Vol. 59, No. 1, 2007, pp. 35-58.

6. THERMO-ELASTO-PLASTODYNAMIC RESPONSE AND DAMAGE EVALUATION

6.1. Introduction

It has been shown in the previous chapters that grain size effects are prominent in laser-material interaction. The thermo-elasto-plasto-dynamic model developed for the research considers the grain size effect in describing the ablation of polycrystalline metals by ultrafast laser pulse. In the following sections, electron and thermal-mechanical responses are investigated gain a better understanding for the mechanism behind the removal of material by optical heating.

Surface electron emission is consisted of two different mechanisms: photoelectric and thermionic emissions. The surface emission rates of the two mechanisms can be individually calculated using the presented model to determine as to which one is more dominant. And, the emission-induced electron number density and electrical field can be used to evluate the probability of ion emission by Coulomb explosion. Many employed the Fourier heat conduction or classic two-temperature model to study electron energy transport dynamics while ignoring the effect of energy current resulted from surface emission. The presented model considers the energy current generated by emission dynamics, thermo-mechanical coupling, and thermally induced elasto-plasticity. It is applicable to evaluating the effect of electron emission on the transport of the electron energy so as to be able to determine whether surface emission and thermo-mechanical coupling can be ignored.

The thermo-elasto-plastic model is applicable to describing the irreversible deformation induced by ultrafast laser heating and estimating the onset of fracture. Thermal-mechanical coupling allows lattice temperature, normal stress and plastic strain to be studied by virtue of laser fluence. The corresponding thermal field provides the basis for establishing if melting has occured during non-thermal ablation. The temporal and spatial evolution of the stress and plastic strain fields give a picture of the irreversible deformation while mechanical fracture and fragmentation ejection are evaluated with the calculated strain energy rate. The model also allows the ablation depth to be quantified a function of the applied laser fluence.

6.2. Dynamics of Electron Subsystem

6.2.1. Surface Emission Rate

Surface electron emission is crucial to the study of plasma dynamics in the early stage of intense ultrafast laser irradiation. The emitted electrons excite ion emissions from the surface and ionize the ambient air, thus the initial plasma plume. As surface electron emissions impact both the electrical and energy fields, incorporating the resulted electrical and energy currents is essential for quantifying the energy dissipation and energy transport to ensure that the electron subsystem is conservative and self-consistent. Photoelectric emission is directly determined by the laser input and absorption. High energy free electrons are emitted when the absorbed laser energy is sufficient to overcome the potential binding energy. On the other hand, thermionic emission is initiated through thermal relaxation. Electrons obtain sufficient thermal energy to overcome the work function of the target material, thus a process occurs after photoelectric emissions. To

study surface electron emissions and identify the dominant emission mechanism, the two competing emission mechanisms are explored for their properties.

To study the effect of laser fluence on the corresponding emission rate, an optical beam of 800nm in wavelength and 100fs in pulse duration is applied to a gold target which is 1μm in thikness. depicts the total emission rate and the thermionic emission rate at 4 different applied laser fluences at 0.3 J/cm^2, 0.5 J/cm^2, 0.8 J/cm^2 and 1.2 J/cm^2, respectively. An estimated ablation threshold for a gold target was 0.5 J/cm^2 [1], which agreed with the experimental value of 0.45±0.1 J/cm^2 reported in Ref. [2]. 0.5 J/cm^2 is being taken by the study as a reference point for establishing the correlation between ablation threshold and laser incident fluence. Given that grain size and thickness are primary parameters impacting the resulted electron temperature, the ablation threshold may vary depending on the geometry of the target material.

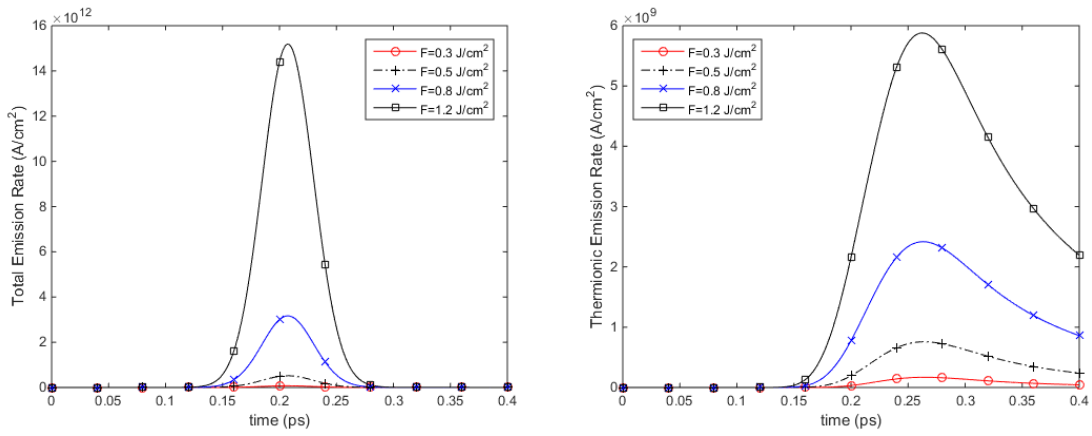

(a). Total emission rate **(b). Thermionic emission rate**

Figure 24. Total and thermionic emission rates at 4 different laser fluences

As indicated in Figure 24, both the photoelectric and thermionic emission rates increase with the laser fluence applied. The magnitude of the total emission rate is of the order of 10^{12} while the thermionic emission rate is 3 order-of-magntidue smaller at 10^{9}. That is, during the optical absorption stage, photoelectric emissions dominate as the primary process and thermionic emissions can be neglected. This is explained by the photoelectric effect in which photoelectrons are able to produce and emit as long as the absorbed energy exceeds the characteristic binding energy. Thermionic emissions take place after thermal relaxation. As seen in Figure 24(a), the total emission rate increases sharply before t=0.15ps when the thermionic emission rate is negligibly small, thus suggesting the dominant role of photoelectric emissions. The total emission rate reaches the climax at approximately t=0.2ps and then rapidly drops off, following the decrease of the absorbed laser intensity. Seen to lag behind the total emission rate in reaching the peak value at t=0.25ps in Figure 24(b), afterward, the thermal emission rate decreases at a much slower pace than the total rate does. However, the rate of drop-off of thermionic emissions is geater than photoelectric emissions', which is attributed to the comparably slow decreasing of the electron temperature. However, emissions by the photoelectric effect are not always the dominant process. Laser fluence J = 1.2 J/cm^2 is chosen for deriving the photoelectric and thermionic emission components. Photoelectric emissions are seen Figure 25 to disappear after the ending of the laser pulse, giving the dominancy to thermionic emissions. Photoelectric emissions in Figure 25(a) are dominant with a magnitude on the order of 10^{12} A/cm^2. Subsequently, after t=0.32ps, the photoelectric emission rate becomes negligibly small and eventually bows out. Although gradually

attenuating, thermionic emissions take over the surface emission and dominates the process starting at 0.32ps as seen in Figure 25(b).

It should be noted that observations made above with regard to the gold material were similarly made with the Al and Cu target materials reported in Ref. [4].

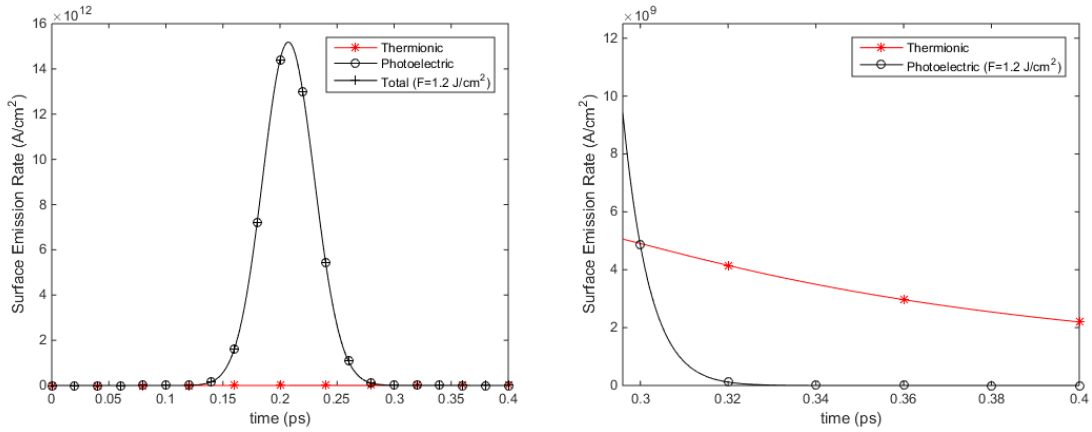

(a). Comparison of different emission rates

(b). Emission rates after ending of laser pulse

Figure 25. Evolution of emission rate at F=1.2 J/cm^2

6.2.2. Electric Field

It is generally believed that Coulomb explosion contributes to the ion emission and surface layers disintegration involved in non-thermal ablation in dielectrics [3] - [5]. Surface electron emissions either by the photoelectric effect or via thermionic emissions provides the stage for the accumulation of positive charges in the irradiated region, inducing an intense electrical field and an electrostatic stress. However, some argue that Coulomb explosion is inhibited in metals due to the screening effects [31] in which

residual electrons with good mobility effectively neutralize the positive charges and suppress ion emissions as a result. Consider the correlation between the external field in the ambient gas and the electric field beneath the surface, $E_{ex} = \varepsilon E_{in}$, with ε being permittivity [3]. In addition to driving the external electrical field and the electrostatic force, E_{in} is also a significant criterion for evaluating Coulomb explosion. A critical electrical field of 2.76×10^8 V/cm was determined for a gold target [5]. It has since been adopted as the criterion for Coulomb explosion. The maximum electrical field beneath the surface at 4 laser fluences (0.3 J/cm^2, 0.5 J/cm^2, 0.8 J/cm^2 and 1.2 J/cm^2) are evaluated against the critical value for Coulomb explosion in Figure 26.

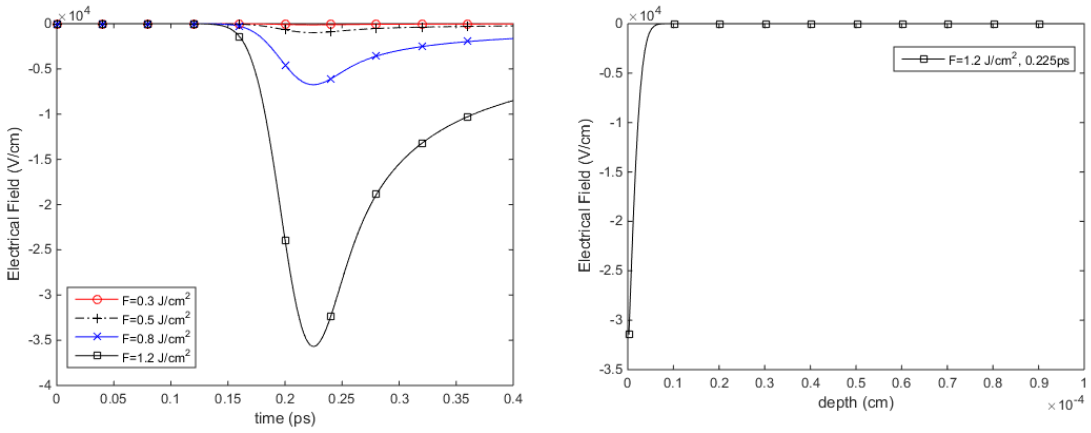

(a). Temporal evolution of electrical field at 4 different laser fluences

(b). Spatial Distribution of electric field at laser fluence F=1.2 J/cm^2

Figure 26. Electrical field generated beneath the surface

The electrical fields are negative and acting along the direction that is opposite to the direction of the laser irradiation. The magnitude of the electrical field is proportional

to the incident laser fluence input, thus agreeing with the observation made with the surface electron emission rate that larger amounts of emitted free electrons can excite a stronger electrical field. The spatial distribution of the electrical field corresponding to F=1.2 J/cm^2 is plotted in Figure 26(b) when the maximum electrical field is reached at t= 0.225ps. It is seen that the highest electrical field is located at the irradiated surface and the magnitude declines inside the target as explained by the screening effect. However, even at the highest laser fluence (F=1.2 J/cm^2), the calculated electrical field is still far below the critical value, indicating Coulomb explosion not being the primary mechanism for the associated ion emissions. It can be concluded that photoelectric effects are improbable for low intensity non-thermal ablation. Ion emission-induced photoelectric stress and Coulomb explosion are not the primary mechanisms of ablation because the force of the electrical field is nowhere being enough to electrostatically disintegrate the surface layers to realize material removal.

6.2.3. Emitted Electron Number Density

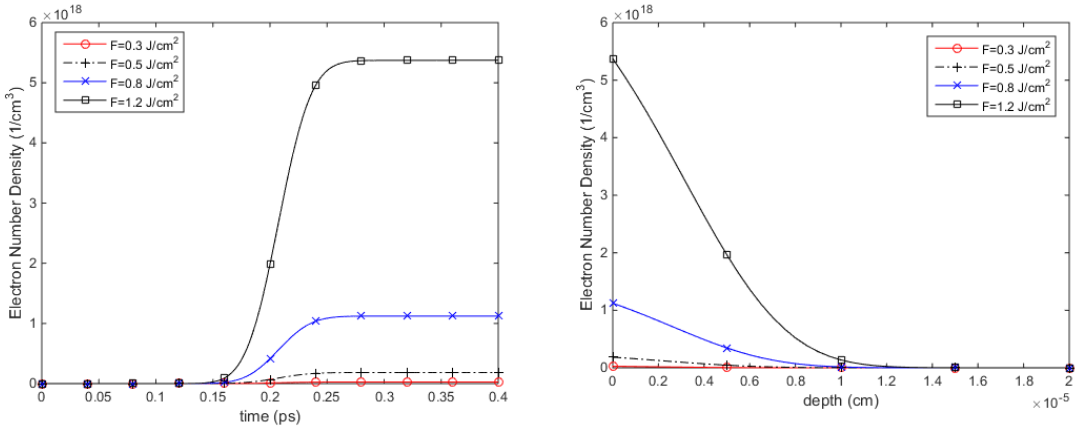

(a). Temporal evolution of electron number density

(b). Spatial distribution of electron number density

Figure 27. Evolution of emitted electron number density at 4 different laser fluences

Figure 27 gives the temporal and spatial profiles of the corresponding emitted electron number density at 4 different laser fluences at 0.3 J/cm^2, 0.5 J/cm^2, 0.8 J/cm^2 and 1.2 J/cm^2. The emitted electron number density of the irradiated surface layers is as much as 10^{18} cm^{-3}. Dissipation of optical energy via photoelectric and thermionic emissions is the early stage of laser-metal interaction. As thermalization (change in the thermal field) is temporarily suppressed by electron emissions, thus the lower electron and lattice temperatures. Figure 27(b) shows the spatial profiles of the electron number density corresponding to 4 different laser fluences. The electron number density decreases along the depth. The electronic transport becomes negligible at 100nm in depth, which is also

correlated with the optical penetration depth. The profile declines with a slower rate compared to the rate of increase of the emitted electron number density. This is attributed to the transport dynamics of the carriers engaging in drifting and diffusion. Drifting is mainly induced by the generated electric field and diffusion is dominated by the carrier (electrons and ions) density gradient. Not considering electron emissions would inevitably overestimate the electron temperature as a result.

6.2.4. Maximum Thermal Field with and without Electron Emissions

Electron temperatures are indicative of the energy transport of the electron subsystem after the equilibrium state is reached. The near-field electron temperature profiles in response to the 4 laser fluences at 0.3 J/cm^2, 0.5 J/cm^2, 0.8 J/cm^2 and 1.2 J/cm^2 are presented in Figure 28. The magnitude of each temperature profile corresponds to the intensity of the laser fluence applied. All the electron temperatures are seen to peak at appproximately the same time at t=0.26ps and then drop off to give rise to heat diffusion and electron-phonon interaction.

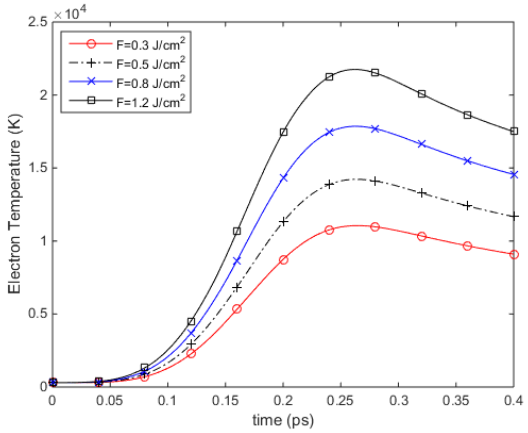

Figure 28. Time profiles of electron temperature at 4 different fluences

Because the emitted electron number density is of the order of 10^{18} cm^{-3}, whatever amount of the optical energy that is not carried off by the emitted electrons is further thermalized. To see the impact of electron emissions on energy transport and the ensuing laser-material interaction, electron temperatures without considering electron emissions are shown in Figure 29. Of the two laser fluences considered, F=1.2 J/cm^2 is the upper bound and F=0.3 J/cm^2 is the lower bound of the non-thermal ablation of the gold material.

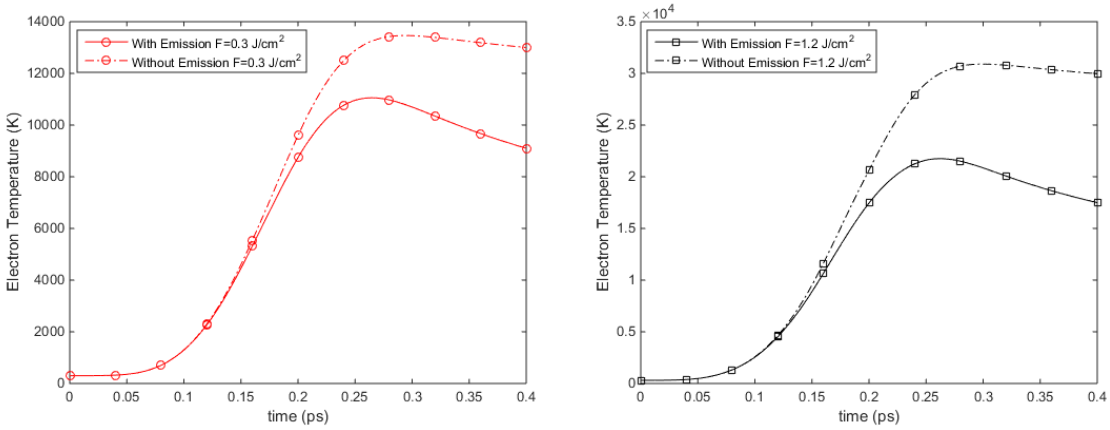

(a). F=0.3 J/cm^2 **(b). F=1.2 J/cm^2**

Figure 29. Comparison of electron profiles at 2 different laser fluences

Electron emissions are critical to the proper description of the electronic and energy transports of the electron subsystem. Electron temperatures are overestimated without considering the energy current caused by the emissions. The dotted line in Figure 29 represents the electron temperature obtained by neglecting electron emissions and the corresponding energy dissipation inside the target, while the solid line denotes the electron temperature generated using the presented energy transport formulation. The disagreement as seen in Figure 29(b) is as much as 71.2% for the case with F=1.2 J/cm^2. The overestimated high electron temperatures would inevitably risk misinterpreting the energy transfer through electron-lattice interaction and intense lattice dilation, leading to the erraneous conclusions of melting instead of non-melting ablation and falsely high stress magnitude or strain rate. The implications of these improper misinterpretations are many, including impeding the comprehensive understanding for the ablation and damage modes of ploycrystalline materials using low fluence, light intensity ultrafast lasers.

The governing equations derived earlier consider an additional energy current w contibuted by electron emissions during the electron energy transport process. Since this energy current decreases and eventually disappears along with the decay of the emission rate following the termination of the laser pulse, the energy dissipation term w can therefore be ignored when its effect on the electron temperature becomes negligibly small.

6.2.5. Effect of Laser Fluence and Pulse Duration

The objective of this section is to establish the correlation between material response and incident laser parameters. Because pulse duration and laser fluence are primary optical parameters, their impact on the electronic transport and the thermal field of the electron subsystem is of interest to the study. A wide range of pulse durations are selected to derive the responses of the maximum electrical field, emitted electron number density, and maximum electron temperature. The effect of pulse duration on non-thermal ablation under the submelting condition is evaluated in Figure 30 using an ultrafast laser of F=0.5 J/cm^2 in fluence and 800 nm in wavelength. It is noted that this particular fluence level below the ablation threshold of the gold material [1].

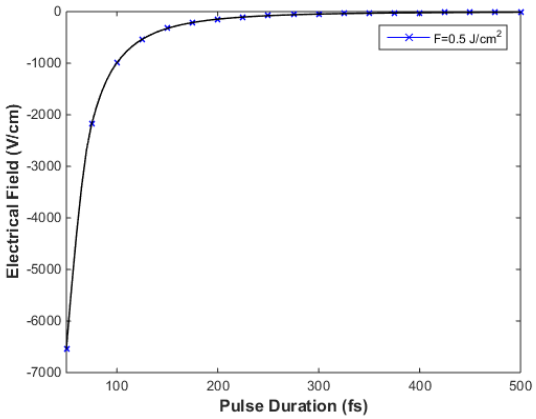

(a). Maximum electrical field vs. pulse duration

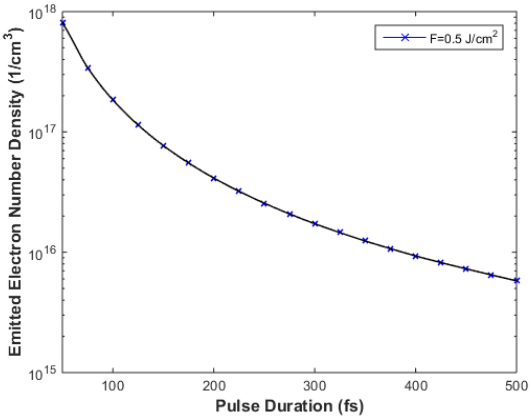

(b). Emitted electron number density vs. pulse duration

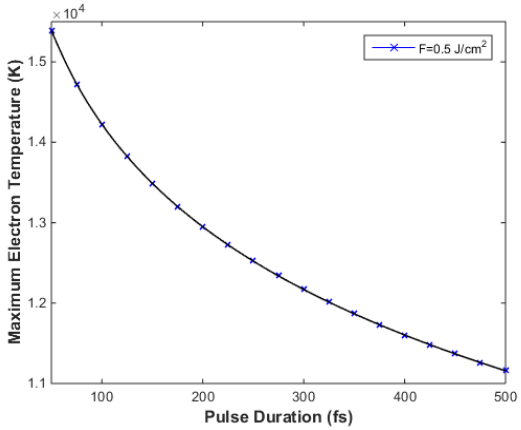

(c). Maximum electron temperature vs. pulse duration

Figure 30. Effect of pulse duration on electronic and thermal fields at F=0.5 J/cm^2

It is evident from Figure 30(b) and 30(c) that both the electron number density and the maximum electron temperature decrease exponentially with increasing pulse duration.

Because increase in pulse duration effectively reduces laser intensity, thus less optical energy is available for emitting free electrons and driving the transport of electron energy. In Figure 30(a) it is seen that the electrical field is high at short pulse durations and diminishes to zero at pulse durations longer than 200fs. As mentioned, the reduction in pulse duration leads to the increase of irradiated laser intensity. And this is greatly attributed to the electron emission in the early time while leaving a larger amount of accumulation of positive charged particles at the near-field. The larger deviation in number densities between electron and ion inside the target promotes the formation of electric field to be higher in magnitude. Besides, at larger pulse duration as above 200fs, the profile of electric field stays decreasing with especially slow rate, denoting the negligible deviation in electron and ion number densities. The electric field reaches a maximum value at approximately 6,500 V/cm^2 as pulse duration of 50fs, which is lower than the critical value for triggering electrostatic disintegration, indicating the inhibition of mass removal due to Coulomb explosion.

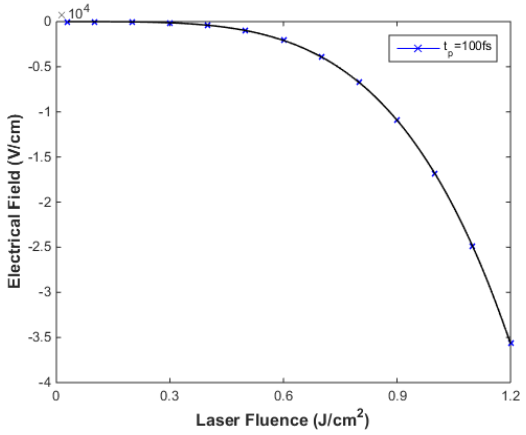

(a). Maximum electrical field vs. laser fluence

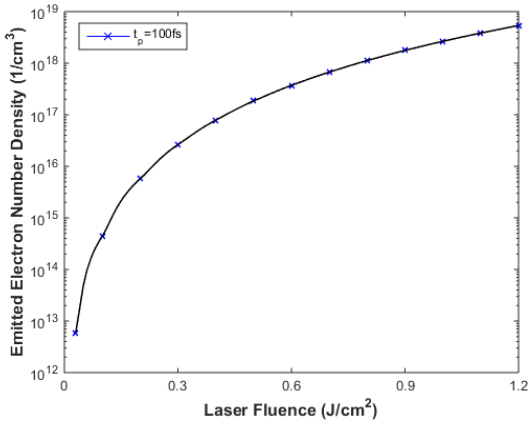

(b). Emitted electron number density vs. laser fluence

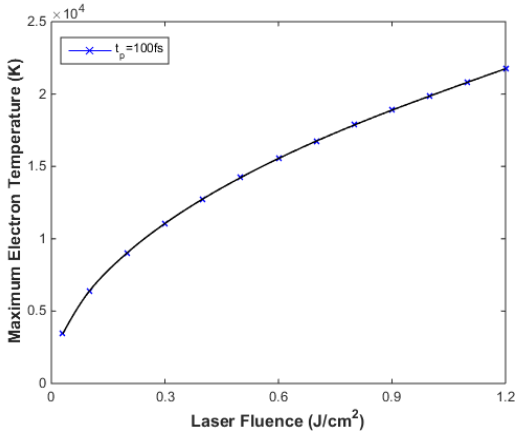

(c). Maximum electron temperature vs. laser fluence

Figure 31. Effect of laser fluence on the electronic and thermal fields at F=0.5 J/cm^2

As one of the primary parameters applied to control the ultrafast laser ablation, Figure 31 presents the effect of laser fluence on electrical field, emitted electron number

density and maximum electron temperature. All profiles as shown in figure reveal the fact that electronic dynamics and energy transport of electrons are also a strong function of laser fluence. The emitted electron number density steeply increase with the increase of laser fluence. The magnitude of emitted electron number density at the applied fluence of 1.2 J/cm^2 can reach the order as high of 10^{19} 1/cm^3. It reveals the fact that high laser fluence greatly excites the electron emission. And the significant high electron number density indicates that a non-negligible amount of energy is dissipated along with the electron emission. Besides, the precipitous increase in the profile of electrical field as shown in Figure 31 (a) denotes a great deviation in electron and ion number density. Thus, it can be expected that a great amount of energy current is produced when particles drift along the generated electric field and an energy current is produced by diffusion due to the deviation in particle concentration. These energy transport dynamics are necessary to be considered.

The maximum electron temperature as plotted in Figure 31 (c) implies a relatively linear relationship between the varied laser fluences and corresponding electron temperature. In the figure, the electron temperature is obtained from the electron energy balance equations while considering the energy loss due to electron emission and the energy current through both diffusion and drift. When applied laser fluence is as high as 1.2 J/cm^2, the maximum electron temperature can approximately reach 2.3×10^4 K. However, the electron temperature could be much higher if ignoring the energy dissipation terms and accordingly mislead to a relatively higher lattice temperature. The higher temperature would further denote the thermal melting rather than non-thermal melting

ablation, which conflicts to the physics observed in ultrafast laser ablation with low laser fluence. Therefore, the established model about surface emission dynamics and the modification of electron energy transport by incorporating the energy loss due to electron emission and energy current via drift and diffusion is crucial and assures the further study on thermo-mechanical coupled responses in non-thermal melting ablation process.

6.3. Dynamics of Lattice Subsystem

6.3.1. Stress-Strain Curve

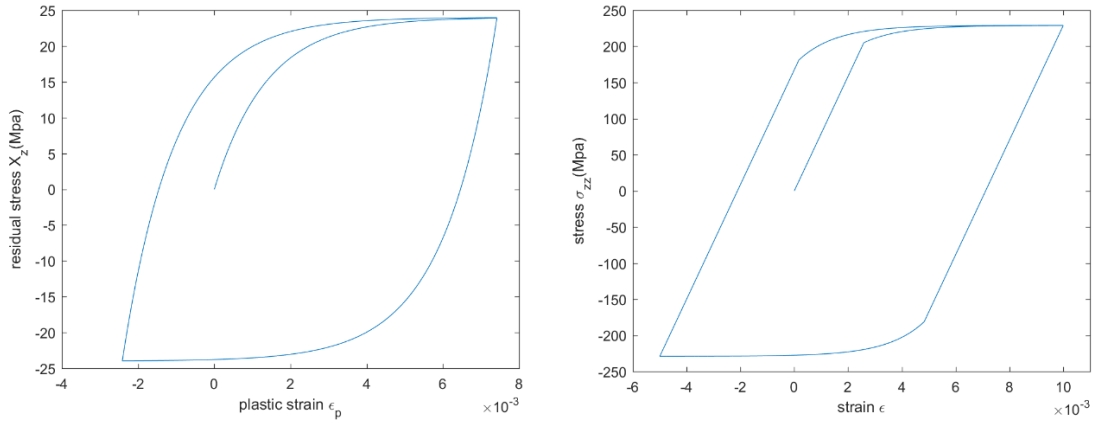

(a). Back-stress vs. accumulated plastic strain

(b). Stress-strain curve

Figure 32. Hysteresis loop under cyclic loadings using nonlinear kinematic hardening model

Figure 32 presents the hysteresis loop derived from the elastic-plastic model in Eqs. (5. 32) – (5.41). The flow chart in Figure 23 was followed to generate the stress (σ_{zz}

) – strain (ε_{zz}) relation in Figure 32(b) and the associated backstress (X_z) vs. accumulated plastic strain (ε_{zz}^{p}) hardening plot in Figure 32(a). Initially in tension, the stress state switches between tension and compression as the material undergoes cyclic loading and unloading. The back-stress is seen to vary in Figure 32(a) when the material is overloaded and plastic and stay unchanged when the material is elastic. Figure 32(b) shows that the yield stress in either tension or compression is not identical to what was registered in the previous loading-unloading cycle. The unloading stress in compression has a lower yield stress compared to the previous yielding stress in tension. This is known as the Bauschinger effect. Moreover, the stress-strain curve in the plastic region demonstrates nonlinearity. Such a nonlinear characteristic is also observed in the backstress – plastic strain relation in Figure 32(a).

6.3.2. Thermal Field

Figure 33 presents the electron and lattice temperature profiles of the polycrystalline gold target at 4 different depths at z=0, z=100nm, z=200nm, and z=400nm in response to a fluence of F=0.8 J/cm^2.

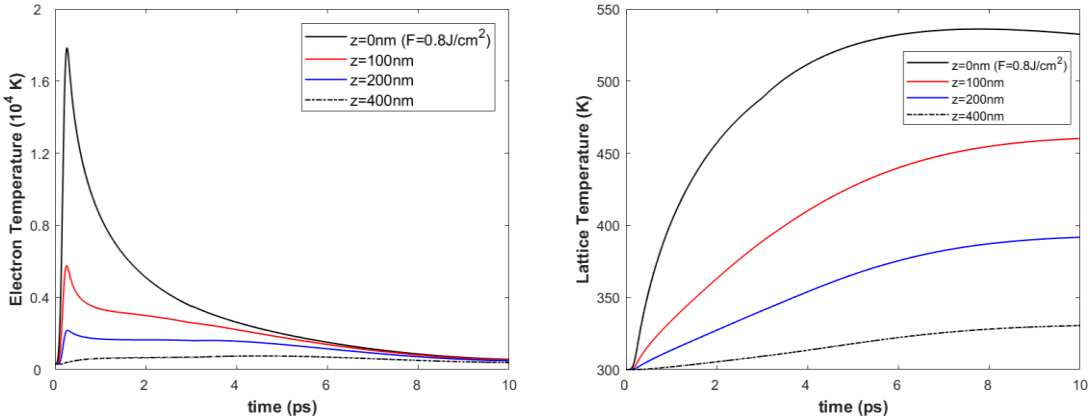

(a). Evolution of electron temperature at different locations with F=0.8J/cm^2

(b). Evolution of lattice temperature at different locations with F=0.8J/cm^2

Figure 33. Temperature profiles at laser fluence F=0.8 J/cm^2

The figure clearly indicats that the electron temperature at z=0nm climbs sharply at first and then declines at a significantly lower rate. The peak of the electron temperature is reached slightly behind the onset time of the peak laser intensity at t = 0.2ps. This delay in time is attributed to the electron relaxation time τ_e. The profile corresponding to z=100nm shows that the increase due to the absorption of laser energy is not as rigorous as the position located close to the irradiated surface. The rate of electron temperature increase and the decline that follows are progressively less rigorous at z=200nm and z=400nm. This can be explained by the optical penetration depth, which is 100nm, and the restrained movement of the electrons defined by the inherent ballistic range. Therefore, increase of electron temperature in the deeper region (greater than 100nm in depth) is suppressed. After reaching the peak, the decline of the electron temperature in near-field involves the diminishing laser intensity, photoelectric and thermionic

emissions, electron thermal diffusion, and electron-phonon interaction. Among these, the energy loss due to emissions plays a dominant role. Discharged electrons of high kinetic energy ionize the ambient air to generate plasma plume of high velocity. Electron temperature drop is not prominent in the deeper region at z=200nm and z=400nm, thus significantly less electron energy flow induced by the surface emissions. Electron thermal diffusion further impedes the drop of electron temperature in the deeper region and the transfer of energy. All the profiles demonstrate a gradual decrease for up to several picoseconds, signifying energies being transferred to the lattices through electron-phonon interaction. Eventually a thermal equilibrium between the electrons and lattice subsystem is reached.

Because all the profiles do not coincide with each other at and beyond t=10ps, as indicated in Figure 33(b), there is a temperature gradient across the material. Once all the lattice temperatures reach a state of thermal equilibrium ($T_e = T_l$) at approximately t=10ps, the sptial temperature gradient starts driving thermal diffusion which propagates at a much slower speed than the transfort speed of the electrons. The thermal gradient and the propagation of the thermal wave work together to induce rapid thermal expansion and contraction that give rise to coupled thermal-mechanical deformation.

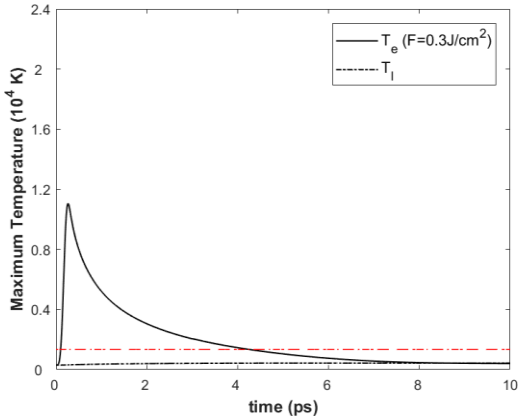

(a). F=0.3 J/cm^2

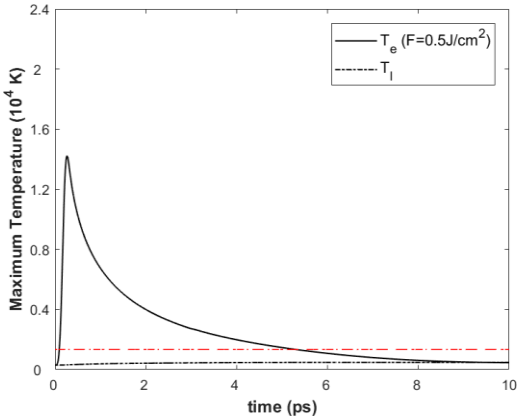

(b). F=0.5 J/cm^2

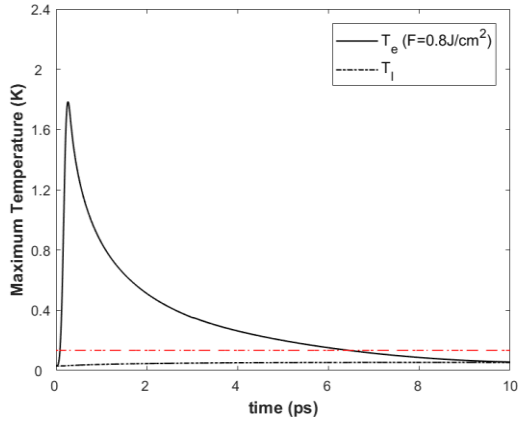

(c). F=0.8 J/cm^2

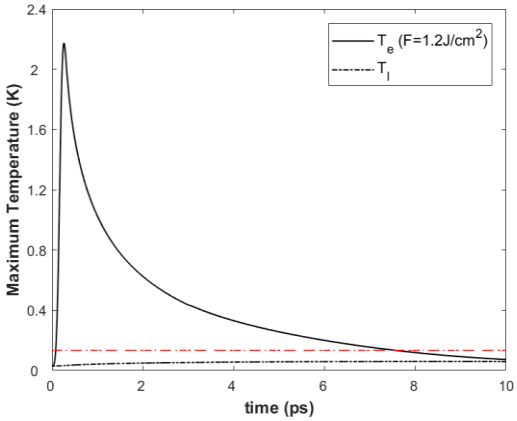

(d). F=1.2 J/cm^2

Figure 34. Evolution of electron and lattice temperatures at different laser fluences

Figure 34 displays the electron and lattice temperature time profiles in response to F=0.3 J/cm^2, 0.5 J/cm^2, 0.8 J/cm^2 and 1.2 J/cm^2. It is evident that all the lattice temperatures are far below the melting temperature of the gold target at 1337K as indicated by the red dash line. It is seen that all the lattice temperatures are far below the red dash-

line, meaning that it is improbable for ablation (material removal) to be accompanied by evaporation and heat-affected-zone. Therefore, material removal induced by light ultrafast laser is dictated by a non-melting mechanism involving no high temperature phase transition or phase explosion.

As time elapses, the electron and lattice temperatures reach a state of thermal equilibrium on the picosecond scale after irradiation. The time for reaching thermal equilibrium is delayed with increasing laser fluence. Since the thermal field is more intense with higher laser intensity, consequently the time window for the corresponding diffusion and electron-lattice interaction is also wider. In general, the state of thermal equilibrium takes several picoseconds to establish with low laser fluence. Longer time is required with high laser fluence. Because the ablation of polycrystalline materials irradiated by ultrafast laser is non-thermal involving surface emissions and low lattice temperature, a better understanding for the underlying mechanism is imperative.

6.3.3. Thermal Stress Field

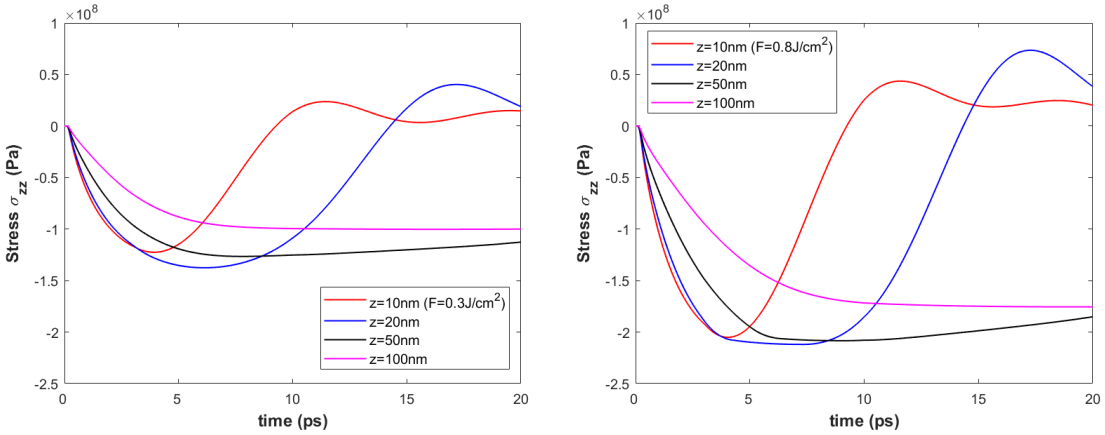

(a). F=0.3 J/cm^2 **(b). F=0.8 J/cm^2**

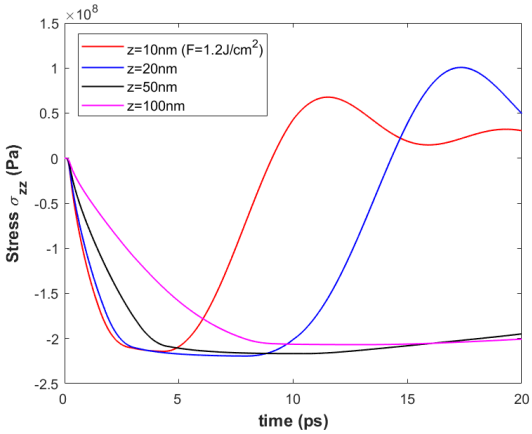

(c). F=1.2 J/cm^2

Figure 35. Evolution of normal stress profiles at different laser fluences

Figure 35 displays the evolutions of the thermal stress σ_{zz} indcued by laser of F=0.3 J/cm^2, 0.8 J/cm^2 and 1.2 J/cm^2 in fluences. The rapid thermally induced expansion and contraction initiate propagating stress waves. Figure 35(a) shows that only elastic

responses are observed at all the locations considered over the 20ps window. The stress states near the irradiated surface at z=10nm and z=20nm are initially compressive and then become tensile. Such oscillations from compression to tension are also observed at z=50nm and z=100nm albeit at a later time. The maximum compressive stress found around t=5ps at z=20nm is far less than the yield stress of the gold material. At F=0.3 J/cm^2, the generation is exclusively elastic involving no plasticity.

The time profiles in Figure 35(b) and 35(c) that correspond to higher laser fluences of 0.8 J/cm^2 and 1.2 J/cm^2, respectively, all indicate plastic stress. The material is initially in compression for all the locations beneath the surface, followed by a switch into tension. However, as indicated in Figure 35(b), the stress at z=20nm reaches the yielding point at t=4ps. The hardening that follows signifies plasticity. When the material undergoes plastic deformation, the stress increases nonlinearly with the strain rate during the loading process. As seen in the figure, the maximum compressive stress also peaks in near-field at z=20nm. Recall the maximum lattice temperature discussed previously that the elasto-plasto-dynamic response of the material is an irreversible deformation involving no thermal melting. Yielding at z=20nm is reached earlier and this stage of loading stays longer with the higher applied fluence F=1.2 J/cm^2 as seen in Figure 35(c). The thermal stress stress at z=50nm reaches the yielding point within 10ps while its counterpart in Figure 35(b) remains elastic. The material yields in near-field with plastic flow earlier with increasing laser fluence. In addition, higher laser fluences induce yielding and larger plastic strains plastic deformation in deeper region. These are precursors to mechanical

damage and layer disintegration of the polycrystalline material ablated by the ultrafast laser pulse of relatively low fluence.

Surface emissions and coupled thermo-mechanical responses are part of the physics that dictates non-thermal ablation involving no melting. Description of ablation dynamics that focuses exlusively on the thermal field without considering electron emissions and thermal stresses is incomplete. It is necessary to consider the cyclic behavior of the thermal stress governed by the hyperbolic heat conduction.

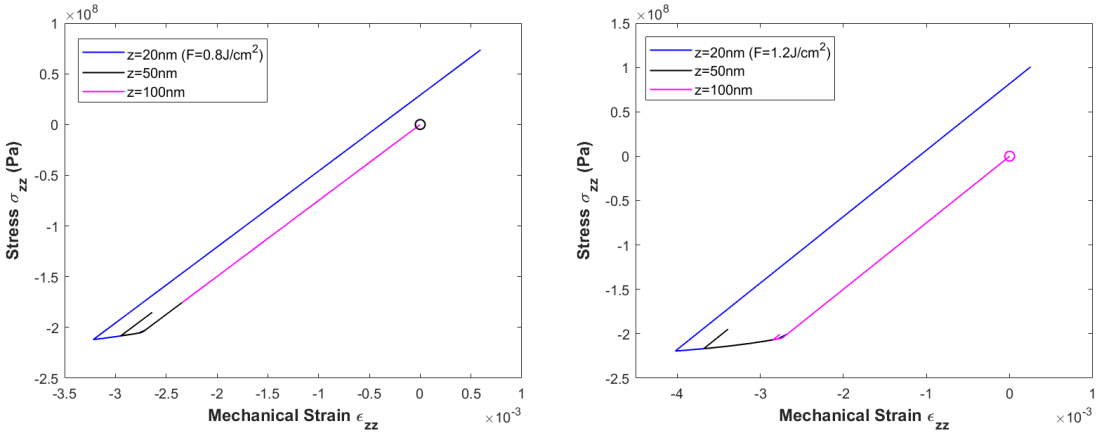

(a). F=0.8 J/cm^2 **(b). F=1.2 J/cm^2**

Figure 36. Stress-strain relation at different applied laser fluences

Figure 36 presents the normal stress-mechanical strain responses at different locations in the polycrystalline gold target subject to ultrafast laser irradiation with F=0.8 J/cm^2 and F=1.2 J/cm^2. All the stress-strain curves in Figure 36(a) originate from the origin, which is indicated by a circle. Initially, the compressive stress increases linearly with the rise of the strain, denoting elastic deformation. The stress-strain curve acquired

from z=100nm (magenta line) does not reach the yielding point and afterward returns to its initial state following the same path. As the material at z=100nm undergoes elastic deformation, the corresponding strain energy (the area under the stress-strain) accumulates. When yielding occurs and the material experiences irreversible deformation the corresponding strain energy is permanently dissipated to realize strain hardening. Hardening is evident in Figure 36(a) for the two locations at z=20nm and z=50nm where a large amount of strains is permanently accumulated.

Similar elastic-plastic behaviors are also observed in Figure 36(b). The figure indicates plastic deformation and hardening have occured at z=100nm and the largest strain is registered near the surface at z=20nm, implying that (1) irreversible deformations are prominent and the corresponding accumulated strain energy is high in near-field in response to ultrafast laser irradiation and (2) surface layers are highly vulnerable to facture and disintegration.

6.3.4. Accumulated Plastic Strain

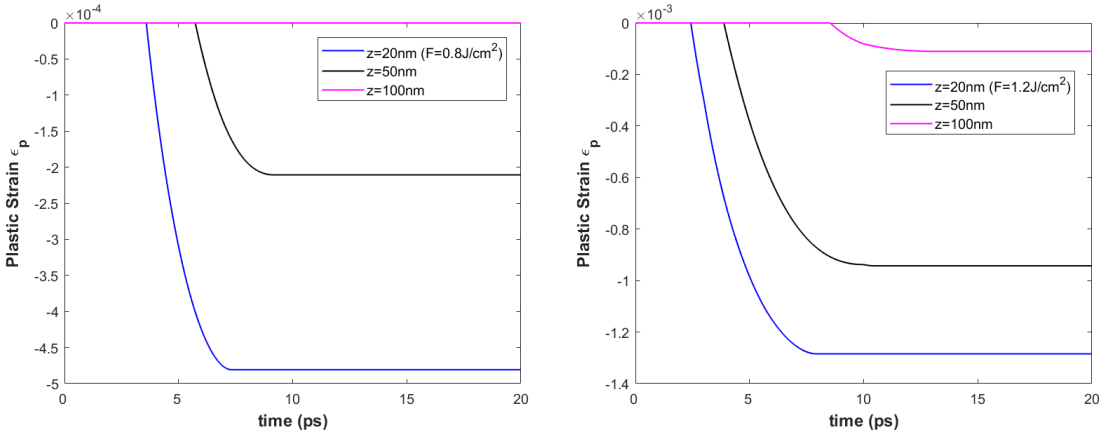

(a). F=0.8 J/cm^2 **(b). F=1.2 J/cm^2**

Figure 37. Evolution of plastic strains at different laser fluences

Irradiation induced rapid thermal expansions and contractions lead to the increment of total strain and the generation of thermal stress. The impact of the thermal field on the mechanical field is implemented in the numerical modelling (finite difference) scheme by excluding the thermal strain component from the total strain increment as $d\varepsilon_{zz}^{e} + d\varepsilon_{zz}^{p} = d\varepsilon_{zz}^{tol} - d\varepsilon^{T}$. The temporal evolutions of the plastic strain in response to two fluences at three locations are presented in Figure 37. In Figure 37(a) a zero plastic strain is found at z=100nm, indicating that the material at the location remains elastic. The plastic strains at z=20nm and z=50nm, however, are none-zero. While the accumulated plastic strain profile remains horizontal, only elastic responses are present with the increment of the plastic strain being zero. The specific onset and termination times of material yielding and hardening can be identified using Figure 37. It is seen that the

material initially yields near the irradiated surface while only elastic deformations are registered in the deeper region. As heating progresses, locations at z=50nm and z=100nm start to yield with low plastic strains. Furthermore, a time delay between the two profiles is observed. At the end of the 20ps time window, the deeper region remains in elastic without yielding or the generation of plastic strain as indicated by the profile of z=100nm.

When the laser fluence is increased to F=1.2J/cm^2, the corresponding plastic strain profiles show that the onset of yielding at the near-field locations is expedited with a higher stress magnitude. The overall plastic strains in Figure 37(b) are signigivantly greater than their counterparts in Figure 37(a). Consequently, although no melting or thermal damage is inflicted, the increasing plastic strain would eventually induce facture via nucleation, crack growth, and void coalesce. The material at z=100nm in depth is seen to start yielding within a few picoseconds from being irradiated.

6.4. Damage Evaluation and Ablation Depth Prediction

6.4.1. Power Density and Ablation Depth Prediction

Although the lattice temperature increases slowly and is well below the melting temperature, the stress field and strain energy that corresponds to the resulted high thermal strain rate are immense. As seen in the previous figures, stress oscillations in near-field are observed within a few picoseconds. As the oscillations propagate, the tensile stress inside the target repels the fragmented and disintegrated layers to eventually eject them from the surface, thus the non-thermal ablation. Since ion emissions do not contribute to ablation, layer disintegration and fragmentation along with stress alternation are the

primary mechanism that dominate the ablation process of the polycrystalline metallic target subject to low fluence ultrafast laser irradiation.

Yielding and plastic strain accumulation are prominent near the irradiated surface. When sufficiently large, the corresponding plastic strain energy accumulated over time is released while the material is in tension to eject fragmentations. It is seen that at $F=0.8J/cm^2$ and $F=1.2J/cm^2$, a large amount of plastic strains has been accumulated when the material is in the state of tension at t=5ps. Therefore, ejection can start as early as several picoseconds in near-field.

Describing the time variation of the energy dissipated to induce plastic flow, strain enery rate has been applied to evaluate damage modes of extremely short time scale, such as quantifying crack growth [8]. Fatigue can be induced by propagating dispersive thermal stress waves of extremely high frequency and low amplitude [56] and [10]. To address the need for describing the thermo-elasto-plastodynamic response to laser ablation, a strain energy based fracture criterion is applied to establish ablation depth as a function of the optical input parameters. Recall that the concept of power density was employed in the previous chapter to characterize thermal-elastic waves of short-time scale. The time variation of strain energy has the same equivalent SI units as power density's: $\left[Pa\cdot\frac{m}{m}\cdot\frac{1}{s}\right]\equiv\left[\frac{N\cdot m}{m^3\cdot s}\right]\equiv\left[\frac{W}{m^3}\right]$. All the strain energy variations in time to be considered in the section are interpreted using the equivalent unit of power density. A criterion exploring the concept of power density (critical strain energy rate) is explored to establish

ablation depth. When the power density at a certain depth violates a critical value, $\dot{W}_c$, fracture and disintegrated layer ejection are considered highly probable,

$$\dot{W} \geq \dot{W}_c \tag{136}$$

The accumulated power density is determined as follows

$$\dot{W} = \int \left| \sigma_{zz} d\dot{\varepsilon}_{zz} \right| \tag{137}$$

where $d\dot{\varepsilon}_{zz}$ is the strain rate increment obtained by excluding the thermal component from the total strain rate using $d\dot{\varepsilon}_{zz} = d\dot{\varepsilon}_{zz}^{tol} - d\dot{\varepsilon}^{T}$. In the finite difference scheme, the expression is discretized using the equation below at each time step,

$$\dot{W} = \sum_{f=0}^{t} \left| \sigma_{zz}^{f} \cdot \Delta\dot{\varepsilon}_{zz}^{f} \right| \tag{138}$$

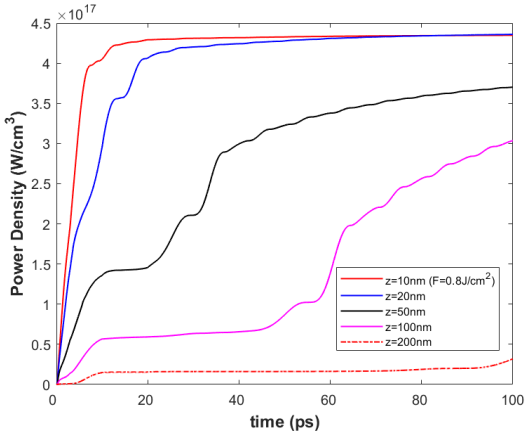

(a). Temporal evolution of strain energy rates at different locations

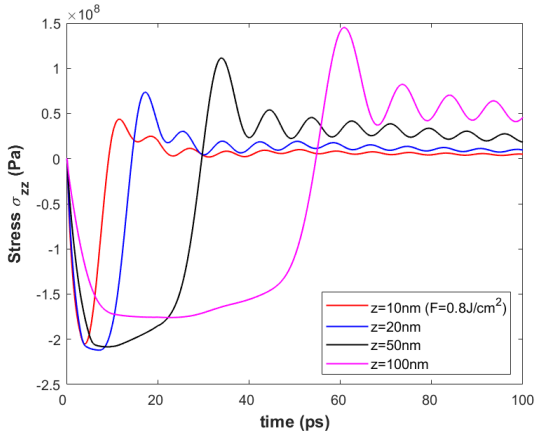

(b). Temporal evolution of normal stresses at different locations

Figure 38. Evolutions of strain energy rate and normal stress at F=0.8J/cm^2

Figure 38 presents the evolution of both the stress field and the corresponding power density of the polycrystalline gold target irradiated with F=0.8J/cm^2. It can be observed from Figure 38(a) that all the power densities increase before reaching a plateau. However, the increase of the power density profile is continuous. This is explained by the temporal evolution of the normal stress in Figure 38(b). In the figure, the normal stresses, in particular those in the deeper region (i.e. z=100nm and z=200nm), remain compressive for a long time at a slow growing rate, thus small growth in power density. After that, the stress rapidly switches to be tensile, leading to the next stage of significant increase. The thermal stress waves excited by the rapid thermal transient are dispersive and attenuative, thus the low and decreasing oscillation of $\dot{W}$. Another significant feature observed from the power density profiles is that the magnitude of the power density reduces with

increasing depth. Being able to establish the spatial profile of the corresponding power density is beneficial for describing non-melting ablation dynamics in terms of material yielding, fracture, and ejection. Qualitative correlations have been established by considering laser input parameters, thermophysical properties, and grain size effects of polycrystalline metallic target, and its coupled thermo-mechanical response. Some rough estimations of ablation depth were established based on either experimental results [11], or the expression of ablated depth individually derived by the laser incident fluence [12], which is criticized to be not consistent with the experimental data [13]. Hence, the present work aims to explore the ablation depth associated with the incident laser fluence by applying the power density generated from the thermo-elasto-plasto-dynamic model which involves in necessary multi-physics of the polycrystalline metallic target irradiated by the ultrafast laser with relatively light fluence. Based on the parameter studies with the use of current model, the laser fluence of F=0.65 J/cm^2 is the dividing crest that material does not yield with lower fluence. And the criterion of power density is selected where material located at z=20nm is found to yield with the applied laser fluence of 0.65J/cm^2, and the critical value of the power density is observed to be 3.46×10^{17} W/cm^3 as indicated by the green dot-line in Figure 39.

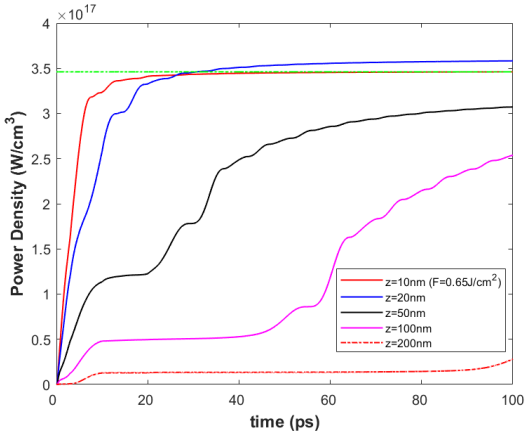

(a). Evolution of power densities at different locations with F=0.65J/cm^2

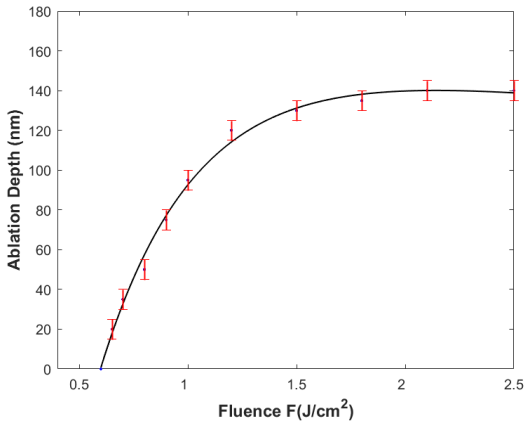

(b). Fitted ablation depth vs. laser fluence

Figure 39. Ablation depth as a function of laser fluences

By applying the criterion of power density, the ablation depth can be evaluated from the power density derived from different locations in depth. When the power density is higher than the critical value, the mechanical fracture and the induced disintegrated layer ejection are thereby assumed to occur after a while. The evaluation of power density, therefore, set the stage for predicting the potential fracture and ablation dynamics due to fragmentation ejection. Moreover, as observed, the deeper region with power density below the critical value is not possible for the fracture and ablation since the corresponding power density continuously decline associated with the increase in depth.

In Figure 39(b), ablation depth is plotted with varied laser fluences for laser beams with wavelength of 800nm and pulse duration of 100fs. In the figure, the error bar denotes the spatial deviation between two adjacent nodes in the mesh of the numerical scheme, which is dz=5nm as used in the computation. Laser fluences are adopted to be slightly

higher than the estimated ablation threshold of F=0.65J/cm^2 as analyzed above. As it can be noticed at the dividing crest, the ablation depth is equal to 20nm. When the lower laser fluence is applied, no mechanical layers are ablated. As is seen, ablation depth steeply increases with the increase of laser fluence no larger than F=1.5 J/cm^2. As applied laser fluence further increases, the growth of ablated depth slows down and eventually the ablation depth reaches the value around 140nm which is considered to be less than twice of optical penetration depth for the laser energy absorption. Meanwhile, the onset time can also be evaluated based from the power density profile and the critical value. For instance, as shown in Figure 39(a), the power density at z=20nm reaches the critical value after 20ps. Hence, the onset time of ablation would not occur after 20ps. Collecting temporal evolution of power density, a general conclusion can be made that the onset time of ultrafast laser ablation with relatively light laser fluence is around tens to one hundred picoseconds.

6.5. Summary

Based on the presented thermo-elasto-plasto-dynamics model for the fundamental mechanism underlying ultrafast laser ablation, both of electronic, thermal and mechanical responses were demonstrated and analyzed. The surface emission due to both of photoelectric and thermionic emission were presented and found that the electron emission rate caused by photoelectric emission dominates the process during the time of entire time of laser irradiation while thermionic emission can be negligible. But at the end of laser beam, the drop of photoemission rate is steep and thermionic emission takes charge as the primary mechanism. Therefore, all of these need to be incorporated as a complete surface

electron emission process. Moreover, the comparison of induced electron temperature showed that the emission dynamics and its energy current is essential to be taken into account and has a significant effect on the thermal field. If not, the corresponding lattice temperature can be improperly high and leads to an irresponsible result of melting. The investigation of emitted electron number density and electric field demonstrated the impossibility for the ion emission due to Coulomb explosion (CE), and hence, another mass removal mechanism is essential and required to explain the mass removal mechanism. The investigation of varied laser fluence and pulse duration on both electronic and thermal fields built a correlation to explore the effect of laser incident parameters on laser-material interaction. The resulted lattice temperature denoted that all the applied laser fluences cannot cause the melting and a different material removal mechanism other than phase transition or phase explosion is required. The study on the thermal-induced mechanical response showed the material response before and after yielding. And the temporal and spatial position where material yields and the evolution of the following plastic deformation and accumulation of plastic strain was also plotted and analyzed. Eventually, a criterion based on the power density was employed to investigate if modes of physical damage due to fracture would likely to occur and predict the ablation depth. Therefore, the correlation of ablation depth and laser incident parameters and necessary thermophysical material properties of polycrystalline metals were built by considering detailed involving multi-physics. The presented thermo-elasto-plast-dynamics model can be further developed into three-dimensionality for the

evaluation of the lateral response and the ablated diameter of the ablated cross-sectional area in certain depth.

6.6. References

[1] Gamaly, E. G., Rode, A. V., Luther-Davies, B., and Tikhonchuk, V. T., "Ablation of solids by femtosecond lasers: Ablation mechanism and ablation thresholds for metals and dielectrics," *Physics of plasmas*, Vol. 9, No. 3, 2002, pp. 949-957.

[2] Stuart, B. C., Feit, M. D., Herman, S., Rubenchik, A. M., Shore, B. W., and Perry, M. D., "Optical ablation by high-power short-pulse lasers," *JOSA B*, Vol. 13, No. 2, 1996, pp. 459-468.

[3] Bulgakova, N. M., Stoian, R., Rosenfeld, A., Hertel, I. V., and Campbell, E. E. B., "Electronic transport and consequences for material removal in ultrafast pulsed laser ablation of materials," *Physical Review B*, Vol. 69, No. 5, 2004, pp. 054102.

[4] Zhao, X., and Shin, Y. C., "A two-dimensional comprehensive hydrodynamic model for femtosecond laser pulse interaction with metals," *Journal of Physics D: Applied Physics*, Vol. 45, No. 10, 2012, pp. 105201.

[5] Bulgakova, N. M., Stoian, R., Rosenfeld, A., Hertel, I. V., Marine, W., and Campbell, E. E. B, "A general continuum approach to describe fast electronic transport in pulsed laser irradiated materials: The problem of Coulomb explosion," *Applied physics A*, Vol. 81, No. 2, 2005, pp. 345-356.

[6] Tao, S., and Wu, B., "The effect of emitted electrons during femtosecond laser–metal interactions: A physical explanation for coulomb explosion in metals," *Applied Surface Science*, Vol. 298, 2014, pp. 90-94.

[7] Cook, R. D., Malkus, D. S., and Plesha, M. E., "Concepts and applications of finite element analysis". Vol. 4. *New York: Wiley*, 1974.

[8] Bower, Allan F., "Applied mechanics of solids," *CRC press*, 2009.

[9] Mao, X., and Suh, C. S., "Generalized Thermo-Elastodynamics for Polycrystalline Metallic Thin Films in Response to Ultrafast Laser Heating," *Journal of Thermophysics and Heat Transfer*, 2018, pp.1-11. doi:10.2514/1.t5429

[10] Oh, Y., Suh, C. S., and Sue, H.-J., "On Failure Mechanisms in Flip Chip Assembly—Part 1: Short-Time Scale Wave Motion," *Journal of Electronic Packaging*, Vol. 130, No. 2, 2008, pp. 021008.

[11] Hwang, D. J., Grigoropoulos, C. P., and Choi, T. Y., "Efficiency of silicon micromachining by femtosecond laser pulses in ambient air," *Journal of applied physics*, Vol. 99, No. 8, 2006, pp. 083101.

[12] Krüger, J., and Kautek, W., "The femtosecond pulse laser: a new tool for micromachining," *LASER PHYSICS-LAWRENCE*, Vol. 9, 1999, pp. 30-40.

[13] Jiang, L., and Tsai, H.-L., "Prediction of crater shape in femtosecond laser ablation of dielectrics," *Journal of Physics D: Applied Physics*, Vol. 37, No. 10, 2004, pp. 1492.

7. CONCLUSIONS

The objective of the present research was to establish the fundamental understandings and establish a comprehensive model for the relevant multi-physics dictating the laser-material interactions in polycrystalline metals subject to the ultrafast laser. The lack of comprehensive descriptions of the non-ablation and non-melting ablation processes and the misunderstandings of the underlying mechanisms that govern coupled thermal-mechanical generation always impedes the border application of ultrashort lasers, which motivated the work. The dissertation addressed the need for interpreting the optical-thermal-mechanical responses of the laser-material interaction in polycrystalline metallic targets for both non-ablation and non-melting ablation cases irradiated by laser pulses of sub-picosecond pulse duration and light fluence, and establishing the connection between the incident laser parameters and the eventually caused mechanical damage. Specifically, the dissertation addressed the objective for describing of laser-induced thermomechanical responses by dividing into two models, where the thermo-elastodynamic model resolved for the mechanism of non-ablation, and the thermo-elasto-plastodynamic model developed for the ablation process. The governing equations throughout the research were featured by hyperbolic type of energy transports for both electron and lattice that admits the finite propagating speed and incorporating energy loss by thermo-mechanical disturbances of thermoelasticity and thermoplasticity when yielding occurs. A staggered-grid finite difference scheme coupled

with a time-integration scheme was developed to simultaneously resolve all filed equations for both uniaxial and three-dimensional model.

A generalized formulation viable for describing the complex dynamic process in non-ablation, including laser energy absorption, thermal diffusion, electron-phonon interaction, and thermo-elastodynamical responses in both single- and poly-crystalline metallic films was presented. The correlated thermo-physical properties were primarily considered that govern both electron and lattice energy transport in polycrystalline metallic films and the grain size effects, including film thickness and averaged grain diameter, on the corresponding thermal-mechanical fields. The one-dimensional thermo-elasto-dynamic model was developed with the incorporation of hyperbolic feature of energy transport in both electron and lattice and the coupled thermo-mechanical field resolved numerically to meet the computational requirement. Normalized electron temperature calculated using the formulation for a single-crystalline gold film was favorably examined against published physical data, verifying the validation of model. Based on the simulated results, grain size effects were found and presented to be of significance on thermal conductivity, electron-phonon coupling factor, and the following thermal-mechanical field response, especially when grain diameter is comparable to the electronic mean-free-path.

It would be insufficient to characterize ultrafast thermo-elastodynamics using models of low dimensionality where lateral distribution of the absorption of the laser energy and heat diffusion along with the resulted stress wave cannot be properly described. In order to be sufficient in the analysis for characterizing the thermal stress wave

propagation and the potential to initiate the fatigue cracking, an axisymmetric thermo-elasto-dynamic model was developed. And a staggered-grid finite difference scheme was created to time-integrate the coupled thermal-mechanical fields along the thickness and radial directions in space. Grain size effects were studied to quantify the inconsistencies in both thermal and stress waves generated in the gold film considering different averaged grain diameters. When smaller averaged grain diameters were considered, the electron and lattice temperature in near-field were higher with a lower electron thermal conductivity and a larger electron-phonon coupling factor, indicating that electron energy was localized and the corresponding scattering attributed to the rapid ascending of temperature in near-field. Such dynamics has a profound impact on the mechanical field responses manifested as stress waves that were intensive and potentially damaging. Both time and frequency analysis with the use of Gabor Wavelet Transform denoted the definitively dispersive and characteristically broad in bandwidth, low amplitude, and extremely high in frequency of the thermal stress wave propagation. And it was also shown that, despite of the non-ablated heating, these waves of high power density were highly detrimental as they were potent enough to initiate fatigue cracking in near-field.

Built upon the proposed formulation, a comprehensive thermo-elasto-plastodynamic model was further developed to understand the underlying mechanism of the light laser intensity ablation on polycrystalline metals. The fundamental knowledge of the underlying multi-physics based on experimental observation was analyzed, denoting a different mechanism required for describing the mechanical damage and surface morphology rather than phase transition or phase explosion induced by ultrafast

laser non-melting ablation with light laser fluence. The complete formulation was viable for describing in both electronic and thermo-mechanical fields of the involved physical dynamics, including laser energy absorption, early plasma formation, thermal diffusion, and the thermal-induced elastic-plastic response, aiming to explain the material fracture and the mechanical disintegration ejection as resulted by the ultrafast laser non-melting ablation. A self-consistent model was proposed for modeling the surface electron emission and the following electronic transport inside the target induced by the ultrafast lasers. Both of two-photon and three-photon photoelectric mechanism and thermionic mechanism were incorporated for electron emission and the drift-diffusion approach was also applied for exploring carriers transport from the bulk to the target surface in the form of electronic flux. The elastic-plastic constitutive equations were built upon Armstrong-Frederick nonlinear kinematic model to describe the complex elasto-plastodynamics responsible for cyclic behavior featured by the rapid thermal processing and nonlinear metallic characteristic of the Bauschinger'effect.

Based on the proposed comprehensive model for the material interaction induced by ultrafast laser non-melting ablation, both electronic, thermal and mechanical responses were demonstrated and analyzed. Both photoelectric and thermionic mechanism were indicated to be significant for the electron emission over hundreds of femtoseconds. And the effect on energy transport due to surface emission was proved to be important on corresponding thermal and mechanical fields. If not consider it, an irresponsible conclusion of melting might possible to make based on the overestimated lattice temperature. The investigation of emitted electron number density and electric field

demonstrated the inhibition for the ion emission due to Coulomb explosion, and hence, another mass removal mechanism was primary and required to be developed rather than phase transition or electrostatic disintegration. The investigation on the thermal-induced mechanical response showed that material initially behaved as elastic and then changed to be plastic associated with the accumulation of plastic strain after yielding. A criterion based on the power density was proposed tin investigate if modes of physical damage due to fracture would likely to occur and was employed to evaluate the ablation depth. Eventually, the correlation of ablation depth and laser incident parameters and necessary thermophysical material properties of polycrystalline metals were built by considering and modeling the complex series of multi-physics.